THE UNIVERSITY *of* EDINBURGH

Studies on the Excited Electronic States of Fullerenes

Minas Stefanou

Degree of Doctor of Philosophy
The University of Edinburgh
School of Chemistry
2020

Lay Summary

Fullerenes are molecules which are made up of only carbon atoms and have three-dimensional hollow structures. C_{60} is the most well studied fullerene. Its structure resembles the shape of a football, where a carbon atom is located on each corner of the joined up hexagons and pentagons. Due to the beautiful simplicity of these otherwise complex molecules, having elementary pure structures with high symmetry behaviours, theoretical calculations and modellings are possible.

The interaction between ultrashort laser pulses (fs-ps $\approx 10^{-15}$-10^{-12} s) and fullerene molecules was investigated. In the first part of the investigation, the focus was aimed at the so called Super-Atom Molecular Orbitals (SAMOs). These are excited electronic states which are characteristic for hollow molecules. In our experiments, electrons were excited from the ground electronic state (equilibrium state) with a laser pulse which initially populated and subsequently probed the SAMOs by ionising the electrons and recording them on a detector. This resulted in spectra being recorded where the intensity of the electrons is probed as a function of their speed (kinetic energy). In combination with theoretical calculations that can replicate the experimental results, the assignment of the features from the recorded spectra was achieved.

Endohedral fullerenes are a special class of fullerene molecules where atoms (as is the case of $Li@C_{60}$) or even molecules, can be encapsulated inside the hollow fullerene cage. In this study, the effects of adding an atom inside the empty C_{60} cage was investigated by comparing similarly acquired data sets for C_{60} with those for $Li@C_{60}$. It was reported that the SAMOs peaks in $Li@C_{60}$ had shifted in kinetic energy and some of them were split into multiple peaks. Gas-phase results were compared with theoretical calculations (performed by Dr Benoit Mignolet and Prof Francoise Remaçle from the University of Liège) and with experiments where C_{60} and $Li@C_{60}$ molecules were placed on a metal surface. The latter experiments were performed by Henry J. Chandler and Dr Renald Schaub from the University of St Andrews. The ability to alter the position of the Li atom inside $Li@C_{60}$ was demonstrated in their experiments where 14 different Li-to-cage-to-metal surface orientations were identified.

In the second part of the investigation, the laser excitation conditions were varied and the effect of the supplied energy to the C_{60} molecules was studied. The results yielded two different timescales for the energy decay and dissipation within the excited molecules. In addition, a feature was identified for the first time which is hypothesised to originate from a decaying long-lived excited state.

Abstract

This work focused on investigating the excited electronic states of fullerenes. Due to their highly symmetric nature and elemental purity, fullerenes are ideal model systems for studying and understanding the excitation and ionisation mechanisms of large complex systems. An intriguing characteristic that they possess is the atom-like nature of the diffuse excited electronic states known as Super-Atom Molecular Orbitals (SAMOs). SAMOs are described as low-lying Rydberg-like states where the charge distribution is centred on the centre of the hollow carbon cage. These states have been observed in gas-phase photoelectron spectroscopic studies of fullerenes, such as C_{60} and C_{70}, and endohedral fullerenes, such as $Sc_3N@C_{80}$. The photoelectron spectra after excitation using fs or ps laser pulses, are characterized by a thermal electron background and a peak structure superimposed on it, having kinetic energies lower than the photon energy. Based on the photoelectron angular distributions and TD-DFT calculations, the peak structure can be assigned to a one-photon ionisation from the SAMO states.

The electronic properties of the endohedral metallofullerene $Li@C_{60}$, C_{60} cage with a Li atom inside, were investigated experimentally for isolated molecules in the gas-phase using laser ionisation, for surface bound molecules using an STM/STS apparatus and theoretically through a combination of DFT and

TD-DFT calculations. Comparisons with the empty C_{60} provide information about the influence that the encapsulated atom has on the electronic system. The off-centre position of the Li inside the cage distorts the symmetry of the SAMOs which affects their binding energies and structure when probed in the gas-phase. Similar behaviours were observed from the calculations and from molecules adsorbed on a metal surface. Due to the asymmetric position of the Li atom inside the cage, Li@C_{60} has been speculated to be suitable to act as a molecular switch. Switching behaviour was observed for surface bound molecules were 14 reversible and stable molecular states that can be statistically accessed were identified. This represents the largest number of multiple states that have been identified in a single-molecular switch.

The influences that the pulse duration, laser fluence and bandwidth of excitation have on the ionisation dynamics of C_{60} and the energy resolution of the SAMOs was studied. The excited electronic energy was found to couple to the vibrational degrees of freedom with a coupling constant of 240 fs, which agrees with previously published results. A 650-750 fs timescale was observed to correlate with the point that thermionic electron emission becomes the dominant decay process over the hot electron emission. In addition, the chirp of the laser pulse affected the central position of the SAMOs and resulted in the photoelectron spectra to be characterised by inhomogeneous broadening. With narrowband excitation, the energy redistribution within the C_{60} molecules is less efficient and evidence of high-lying Rydberg states was present in the photoelectron spectra. Lastly, a peak superimposed on the delayed ionisation tail of C_{60}, found roughly at 6.9 µs after the prompt peak, was identified for the first time. A hypothesis for the origin of this feature is proposed which is based

on energy being released from a decaying long-lived superexcited state or a group of high-lying Rydberg states.

List of Publications

Stefanou, M., Chandler, H. J., Mignolet, B., Williams, E., Nanoh, S. A., Thompson, J. O. F., Remacle, F., Schaub, R. and Campbell, E. E. B. Angle-resolved photoelectron spectroscopy and scanning tunnelling spectroscopy studies of the endohedral fullerene Li@C_{60}. *Nanoscale* **11**, 2668-2678, 2019.

Chandler, H. J., Stefanou, M., Campbell, E. E. B. and Schaub, R. Li@C_{60} as a multi-state molecular switch. *Nature Communications* **10**, 2283, 2019.

Acknowledgements

So, this is it... What an unforgettable, beautifully calm and bumpy road has this been. There are many faces that I am grateful to, because without them, I wouldn't be in the position I am just now.

First of all I would like to thank my supervisor Professor Eleanor Campbell for giving me this unique experience of working in an ultrafast laser laboratory. Her support, wealth of knowledge and guidance has been the building block for my understanding of the subject and the progression of my work. I am extremely grateful as despite her busy schedule, she always made time to discuss any issues I had in the lab or in the data analysis.

I now want to thank Dr Adam Kirrander for all his support all these years. Whenever I'd unexpectedly knock on his door he would always greet and invite me in with a big smile. Thank you for guiding me through some difficult times.

I want to extend my gratitude to our group's collaborators, Dr Renald Schaub and Dr Henry Chandler from the University of St Andrews, who performed the remarkable and exciting work on the surface bound fullerenes molecules. Their help and explanations were crucial in my understanding of the STM and STS results. In addition I want to thank our group's long time collaborators,

Dr Benoit Mignolet and Professor Francoise Remaçle from the University of Liège, who performed the TD-DFT and Dyson orbital calculations for C_{60} and Li@C_{60}. Thank you for hosting me in your beautiful city, explaining me the works behind the calculations and showing me a good time in Liège.

I want to thank the Innovation Initiative Grants committee for supporting my application. That grand made it possible for me to buy vital equipment that I required in order to build the pump-probe setup.

It goes without saying that Dr Olof Johansson's guidance in the lab and his knowledge of the laser setup and vacuum apparatus was unimaginatively helpful throughout all these years.

At this point I want to thank all the members of the laser lab groups; Nathan, Florian, Luke, Andrei, Oleg, Elvira, Hal. It wouldn't have been the same without you. And to the guys from Adam's group, Nikola, Andrés, Darren, Mats, thank you for all the help regarding the computational stuff, all the laughs and delicious dinners.

To Dr Andy Alexander and Professor Philip Camp, thank you for your support when times were tough and for the laughs and interesting conversations that were had under the consumption, or not, of delicious bottles of aged Port and Vodka. I will always keep in mind; a shot of vodka is always hidden on the walls of an empty bottle.

This one is for all the subnormal, incredibly talented and beautifully weird humans/fae/pixxies/drummers that I have crossed paths with within the Beltane Fire Society. It is without a doubt that because of you I managed to keep my sanity to continue and finish this work. Fire Point 2018. Order of the Sun. Voice

of the Hill. BeastiesBeastiesBeasties Samhuinn 2019 and Beltane 2020. With the honourable mentions of Doogie, Craggles, Sam, Toni, Nathan. We've danced and screamed together when I was at my best, and you calmed me down and gave me space at my worst. Hugs and love to you all.

Hannah, I was really lucky to have you by my side all those years. Thank you for everything. I will always cherish the memories we made together.

To my oldest friends; Stonness, Sian, Alan, May, Sere. Thank you for being there for me all these years, I'm thinking of you constantly.

River, we've been through so much already, yet there is so much more to do, see and create. It has been such an unexpected gift being able to share my time with you. Thank you for your continued love and support.

Last but not least I would like to thank my family for their constant support, believing in me and letting me follow all these paths that I have chosen. Dad, Ma, Dimitri, Pappou, Nane, Pappou Dimitri, Giagia Vasiliki - I love you all. I couldn't have done this without you.

This thesis is dedicated to my grandparents Νανέ and Παππού.

Mabel

Always in my heart.

Crossed the rainbow bridge on the 3rd of June 2020.

Contents

List of Abbreviations

AI-PES	Angle-Integrated Photoelectron Spectrum
AR-PES	Angle-Resolved Photoelectron Spectrum
ATI	Above Threshold ionisation
BBO	β-Barium Borate
CPA	Chirp Pulse Amplification
DFT	Density Functional Theory
FWHM	Full Width Half Maximum
HOMO	Highest Occupied Molecular Orbital
IC	Internal Converion
LDOS	Local Density of States
LT-STM	Low-Temperature Scanning Tunnelling Microscopy
LUMO	Lowest Unoccupied Molecular Orbital
MCP	Microchannel Plate
MO	Molecular Orbital
MPI	Multi-Photon Ionisation
NFE	Nearly-Free Electron Band
NOPA	Non-colliniear Optical Parametric Amplifier
OPA	Optical Parametric Amplifier
PAD	Photoelectron Angular Distribution
PES	Photoelectron Spectrum
SAMO	Super-Atom Molecular Orbital
SHBC	Second Harmonic Bandwidth Compressor
SHG	Second Harmonic Generation
SOMO	Singly Occupied Molecular Orbital
STS	Scanning Tunnelling Spectroscopy
TD-DFT	Time-Dependent Density Functional Theory
THG	Third Harmonic Generation
Ti:Sapph	Titanium-dopped Sapphire
TKER	Total Kinetic Energy Release
TOF-MS	Time-of-Flight Mass Spectrometer
VMI	Velocity Map Imaging
WLC	White Light Continuum

1 Introduction

In a somewhat remarkable and unexpected fashion, experiments designed to investigate the molecular composition of interstellar clouds led to the groundwork of developing a revolutionary area of physics, chemistry and materials science. It all started in 1985 when Harry Kroto, Rick Smalley, Robert Curl and their co-workers within the universities of Rice and Sussex, discovered C_{60}.[1] In their experiment, laser irradiation was used to vaporise a solid piece of graphite, in the hope of reproducing the conditions found near giant stars and thus be able to study the formation of long-chain carbon molecules that had been identified in interstellar space. Their results showed the existence of a highly stable cluster consisting of 60 carbon atoms. The proposed structure for this cluster was a highly symmetric truncated icosahedral cage consisting of 20 hexagonal and 12 non-adjacent pentagonal faces. This molecule was classed as a new allotrope of carbon and was referred to as buckminsterfullerene, buckyball or fullerene due to the similarity between its molecular shape and the well known geodesic structures designed by Richard Buckminster Fuller. As a result of their discovery of fullerenes, Kroto, Smalley and Curl were awarded the 1996 Nobel Prize in Chemistry.

A major milestone came after the production and isolation of C_{60} in macroscopic quantities by Krätschmer *et al* in 1990.[2] They proposed a simple method

of using arc-discharge between two graphite rods to produce C_{60} and trace amounts of C_{70}. This allowed research groups to investigate and produce a vast amount of different fullerene and fullerene-like molecules, for example: a variety of C_x cage fullerenes; endohedral fullerenes, which are cage fullerenes that have an encapsulated atom or molecule within the hollow cage; exohedral fullerenes, which are cage fullerenes with a functionalised group attached to the cage; graphene sheets, which are 2-D sheets consisting of only carbon atoms in a hexagonal lattice; and carbon nanotubes, which are graphene sheets that are bend to form a hollow tube structure.

Fullerenes have been used as model systems to examine the excitation and ionisation mechanisms of large complex molecules and clusters. Because of their elemental purity and high symmetry, high level calculations have been feasible. Fullerenes are a particularly interesting species as depending on the method they are studied in the gas-phase, they have been shown to possess properties that are either characteristic to bulk matter or to a really large atom. How could these properties be further explored and what additional information could be extracted from such a well studied system?

Two different projects will be presented in this thesis. In the first, the aim was focused on investigating the fundamental properties of the endohedral metallofullerene (fullerene cage with an encapsulated metal atom) Li@C_{60} and compare it to the empty C_{60}. Through a combination of gas-phase experiments, theoretical computations and surface science experiments, the properties of the Super-Atom Molecular Orbital (SAMO) excited electronic states was investigated, Chapter 3. In the second project, the aim was to study how the laser ionisation conditions - pulse duration, laser fluence and bandwidth - affect the

ionisation dynamics and the appearance of the SAMOs in C_{60}, Chapter 4. This was achieved through a range of gas-phase experiments.

1.1 Photoionisation mechanisms in strong laser fields

The interaction between a laser pulse and a molecular or atomic system which results in ionisation is a well studied physical phenomenon. The photon energy and intensity of the laser pulse have a decisive role in terms of what type of photoionisation mechanism will take place. When using photon energies that are greater than the ionisation potential of the system, photoionisation can occur readily even with low laser intensities. If however the photon energy is smaller than the ionisation potential, as is the case when using visible to near-infrared radiation, stronger intensity laser pulses are required for the photoionisation to take place. In this energy and intensity regime, three main ionisation mechanisms are in play - multi-photon ionisation (MPI), tunnelling ionisation and over-the-barrier ionisation (Figure 1.1 shows the corresponding schematic diagrams).[3,4]

In order to distinguish which ionisation mechanism is dominant in a particular scenario, the Keldysh parameter, γ, is used,

$$\gamma = \sqrt{\frac{IP}{2U_p}}, \tag{1.1}$$

where IP is the ionisation potential and U_p is the ponderomotive energy.[3,5] U_p is defined as the energy that a free electron gains when it couples to the oscillating laser electric field and is given by,

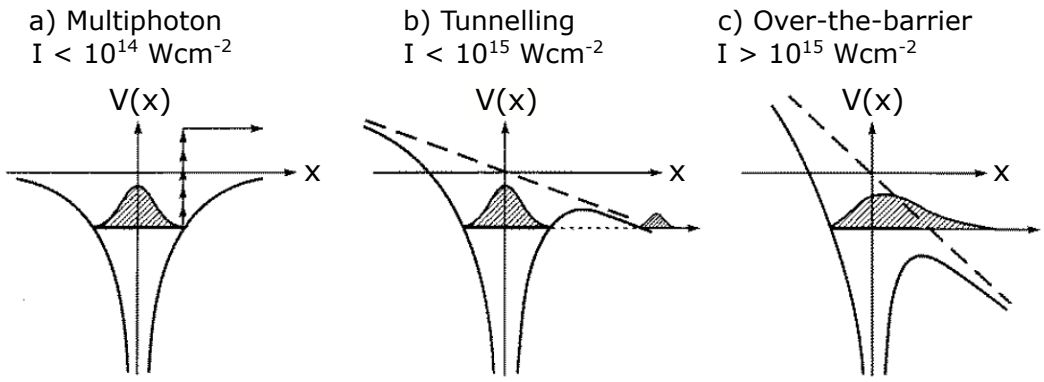

FIGURE 1.1: Diagram showing the strong laser field ionisation mechanisms. (a) multiphoton ionisation, (b) tunnelling ionisation and (c) over-the-barrier ionisation. The solid lines correspond to the binding potential while the dashed lines to the laser electric field. Figure adapted from Protopapas *et al.*[4]

$$U_p(\text{in eV}) = (\frac{F_0}{2\omega})^2 = 9.34 \times 10^{-20}\lambda^2 I, \tag{1.2}$$

where F_0 and ω are respectively the laser electric field amplitude and angular frequency, λ is the laser wavelength (in nm) and I is the laser intensity (in Wcm^{-2}).[6]

For relatively low intensities where $\gamma >> 1$, direct multiphoton ionisation is the dominant mechanism, Figure 1.1 (a). In this ionisation regime, a number of photons are coherently absorbed by the system which results in the total energy to overcome the ionisation potential. It is also possible for even more photons to be absorbed than what are required to just overcome the ionisation potential, known as above threshold ionisation (ATI). In the photoelectron spectra, the ATI peaks appear as a set of subsequent peaks after the direct MPI peak, that are separated by one photon energy.[7] When no intermediate states are resonant with a multiple of the photon energy, the ionisation probability is

given by I^n where n is the number of photons needed to exactly overcome the ionisation potenital.[8] If however an intermediate state is resonant with a multiple of the photon energy, the ionisation probability is increased significantly, a phenomenon called resonance-enhanced multiphoton ionisation (REMPI).[9]

For intermediate intensities where $\gamma \approx 1$, the magnitude of the laser electric field becomes comparable with the system's binding potential. This results in suppressing the ionisation barrier. Given that the electric field is oscillating, electrons can be ionised by tunneling through the barrier only if the tunneling period is shorter than the field's oscillations. This mechanism is known as tunnelling ionisation, Figure 1.1 (b).[3] For even higher intensities where $\gamma << 1$, the electric field suppresses the ionisation barrier so much so that the electron escapes from the barrier without tunneling. This mechanism is known as over-the-barrier ionisation, Figure 1.1 (c).[3] For the last two mechanisms, given that the magnitude of the electric field effectively 'pulls' the electron into the continuum, they are classified as the field ionisation regime.

In the following discussion, the excitation and ionisation events that take place assume to involve only one active electron. In addition, the laser intensities used in this thesis are within the multiphoton regime and thus the focus of the discussion will be limited to that.

1.2 Photoexcitation mechanisms in fullerenes

The ionisation behaviour of C_{60} is particularly interesting as it can be described as having properties that are characteristic of bulk matter or of isolated molecules. When irradiated with intense, ultrashort laser pulses, C_{60} can absorb multiple

photons whose total energy is larger than the ionisation potential, creating a molecule in highly excited, non-equilibrium states (denoted with an asterisk in Equation 1.3). The energy is initially absorbed within the electronic subsystem and over time it is assumed to be equilibrated over all the electronic degrees of freedom. Eventually, through coupling between the electronic and vibrational degrees of freedom, followed by intramolecular vibrational redistribution, the energy is fully equilibrated over all of the degrees of freedom. This excess energy can be released through three competing decay processes, Equation 1.3 : (i) dissociative decay (evaporation of neutral C_2 fragments), (ii) radiative decay (emission of photons), and (iii) delayed ionisation/ thermionic emission (emission of electrons).[10] Figure 1.2 demonstrates the relationship between the microcanonical rate constants of these decay processes and Table 1.1 displays the parameters of the microcanonical rate constants. The mechanism by which these processes occur depends on the rate of energy absorption and thus on the laser pulse duration. For the timescales which are studied in this thesis, radiative cooling can usually be neglected.[11] The focus of the remainder of this section will lie on the competition between dissociation and delayed ionisation in C_{60}.

$$\begin{aligned} &\text{(i)}\ C_{60}^{*} \rightarrow C_{58} + C_2 && \text{Dissociation} \\ &\text{(ii)}\ C_{60}^{*} \rightarrow C_{60} + h\nu && \text{Radiative decay} \\ &\text{(iii)}\ C_{60}^{*} \rightarrow C_{60}^{+} + e^{-} && \text{Delayed ionisation/} \\ & && \text{Thermionic emission} \end{aligned} \tag{1.3}$$

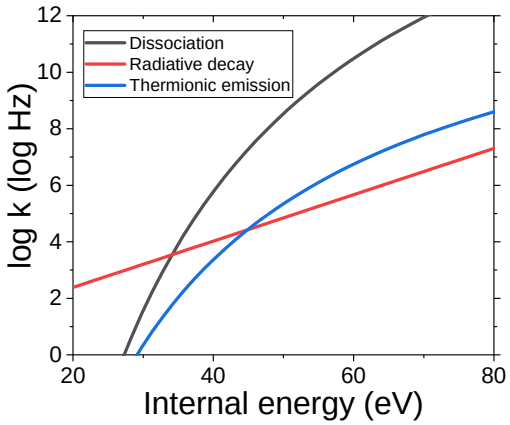

FIGURE 1.2: Microcanonical rate constant, k, plotted as a function of internal energy of the excited neutral C_{60} molecules for the cases of dissociation,[12] radiative decay[13] and thermionic emission.[14]

	Decay process rate constant	Parameters		Reference
		A (Hz)	E (eV)	
C_2 Dissociation (for neutrals)	$k = A\exp(-\frac{E}{k_B T_e})$	1×10^{22}	10.6	[12]
C_2 Dissociation (for ions)		1.2×10^{21}	10.1	[14]
Thermionic emission		1×10^{15}	7.6	[14]
Radiative cooling	$\log k = 0.082E + 0.744$	-	-	[13]

TABLE 1.1: Microcanonical rate constants for the decay channels of C_{60} molecules.

Pulse duration > ps

For excitation with ps or longer laser pulses the gained electronic energy has enough time during the laser pulse to couple to the vibrational degrees of freedom, thus creating a vibrationally hot molecule that readily fragments and ejects electrons on the µs timescale (delayed ionisation). Both fragmentation

and electron emission are described by statistical models of the Arrhenius form that assume the energy to be equilibrated over all the degrees of freedom.[15] Delayed ionisation can be seen on the molecular ion peak (C_{60}^+) as a tail on the high mass side, Figure 1.3 (a). Mass spectra at these pulse durations are typically characterised by having only singly charged species. For high excitation energies a bimodal fragmentation distribution is observed as is the case in Figure 1.3 (a). On the high mass side, the ions are formed by a subsequent C_2 evaporation from the molecular ion peak corresponding to smaller fullerene cages, while on the low mass side the peaks are separated by one C atom which result from the breaking up of the fullerene cages into smaller carbon chains and rings.[13,16] The photoelectron spectra, Figure 1.3 (b), at these pulse durations are structureless and can be fitted by a Boltzmann distribution,

$$I \propto A\, exp(\frac{-E_K}{k_B T_a}), \tag{1.4}$$

where I is the electron intensity, A is a pre-exponential factor, E_K is the electron kinetic energy, k_B is Boltzmann's constant and T_a is the electron apparent temperature, which is a measure of the average energy of the delocalised electrons.[17–19] Typical observed values for the apparent temperature are 3000-4000 K or 0.26-0.34 eV (using the conversion: 1 eV = 1.160×10^4 K). The isotropic distribution of the VMI (Velocity Map Imaging) image (inset in (b)) combined with the Boltzmann energy distributions is a strong indication that the emission mechanism is purely statistical in nature. The delayed ionisation phenomenon was attributed to thermionic emission due to the coupling between the rovibronic and electronic states.[20] The reason why it competes with the

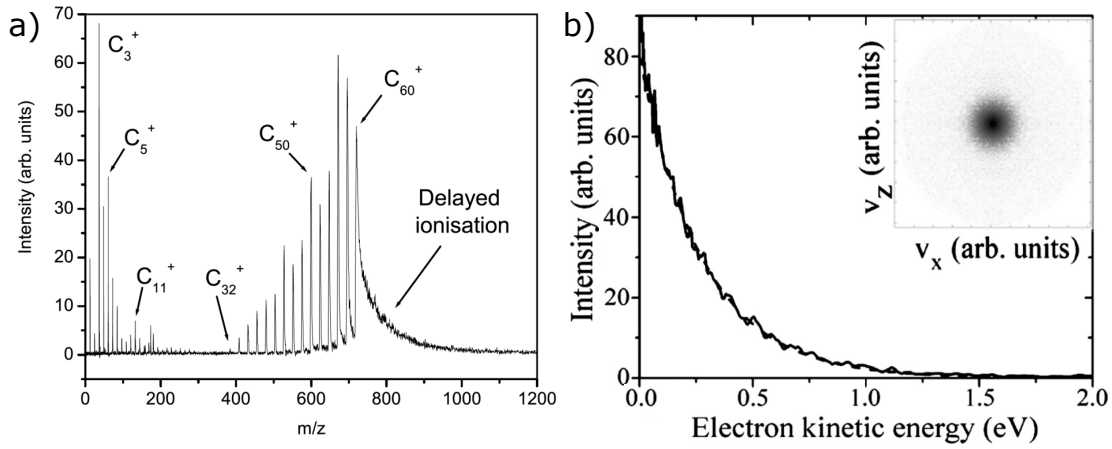

FIGURE 1.3: Typical C_{60} spectra taken using ns excitation. (a) TOF-mass spectrum using 337 nm ns pulses. (b) Angle-resolved PES using 532 nm 4 ns pulses. The VMI image shown in the inset depicts the isotropic distribution. Figure (a) adapted from Heden[21] and (b) from Johansson *et al.*[22]

dissociative decay lies on the fact that the ionisation potential of C_{60} (7.6 eV) is lower than the dissociation energy of C_2 emission (10.6 eV).[14] In later chapters, this statistical electron emission will be referred to as the thermal background.

Pulse duration ≈ ps-fs

As the pulse duration decreases to between 1 ps and 100 fs, previously suppressed ionisation channels come into play. On these timescales the excess energy does not have enough time during the laser pulse to couple to the vibrational subsystem and is accumulated in the electronic subsystem, inducing thermal ionisation from excited electrons in addition to direct multiphoton ionisation. Experimental data indicate that the coupling timescale within the electronic subsystem is on the order of 50 fs while the coupling between the electronic and vibrational subsystems is on the order of 240 fs.[23,24] Hence, electrons

are promptly ionised from the hot electronic subsystem followed by coupling of the remaining internal energy to the vibrational subsystem which leads to later fragmentation. This mechanism is known as transient thermal electron emission.[24–26] Multiple charged species, less fragmentation and no delayed ionisation on the µs timescale are observed in the mass spectra while larger apparent temperatures (10000-40000 K = 0.86-3.45 eV) are recorded on the PES (Figure 1.4 left and right hand side show respectively the mass spectra and the PES taken over a range of pulse durations). Similarly to thermionic emission, a Boltzmann distribution can fit the PES, however often a peak structure is superimposed on the thermal background. This peak structure has been assigned to originate from the Super-Atom Molecular Orbitals (SAMOs).[27] Further information will be provided in Chapter 1.4.

Anisotropic electron distributions, having a higher apparent temperature along the direction of the laser polarisation compared to the perpendicular one, have been reported for certain excitation energies within the ps-fs pulse duration range.[17,26] Calculations have shown that most of the electron emission takes place within the laser pulse duration.[26] Based on classical electrodynamics, electrons 'born' inside an oscillating electric field will gain a momentum kick along the direction of the field. Since thermal electrons are statistically emitted, they are not correlated with the laser field, meaning they can be emitted at any time during the oscillating field. Therefore the added kinetic energy is proportional to the value of the instantaneous vector potential which can take a maximum value of up to $2U_p$.[28] According to Equation 1.2 the degree of asymmetry will thus be wavelength dependent. Figure 1.5 compares the results of ionising C_{60} with 400 nm and 800 nm 120 fs pulses. Considering

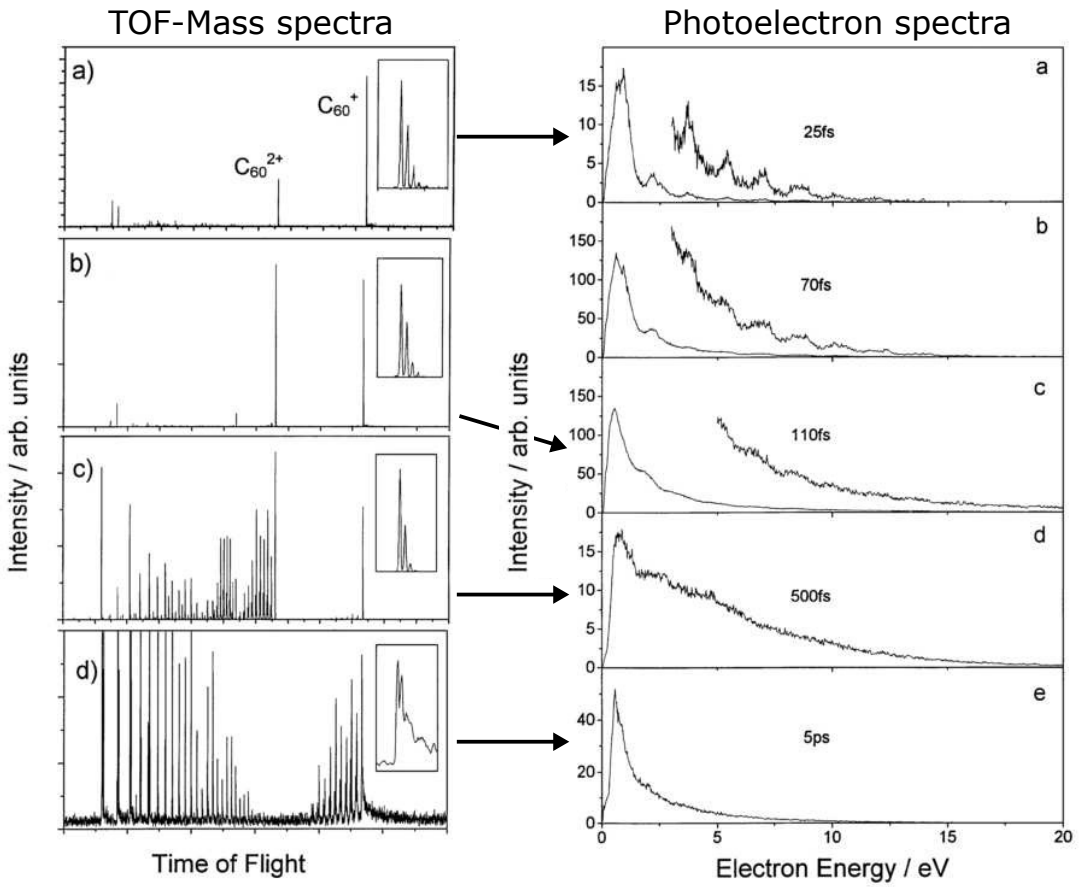

FIGURE 1.4: C_{60} mass spectra and PES taken using a range of ps to fs pulses. Left hand side: TOF-mass spectra taken with pulse durations of (a) 25 fs, (b) 110 fs, (c) 500 fs and (d) 5 ps and laser intensities of (a)-(c) $(8\pm2)\times10^{13}$ Wcm^{-2} and (d) 5×10^{12} Wcm^{-2}. Right hand side: PES taken with identical pulse durations and laser intensities for (a), (c), (d) and (e) with respect to the mass spectra (a)-(d) respectively. (b) 70 fs and $(8\pm2)\times10^{13}$ Wcm^{-2}. Figure adapted from Campbell *et al.*[25]

the similarities in the fragmentation patterns of the mass spectra, the overall energy absorbed by the molecules is assumed to be similar. The asymmetry in the VMI images can clearly be seen from the angular-resolved PES for 800 nm, showing a higher apparent temperature along the direction of the laser polarisation.[28]

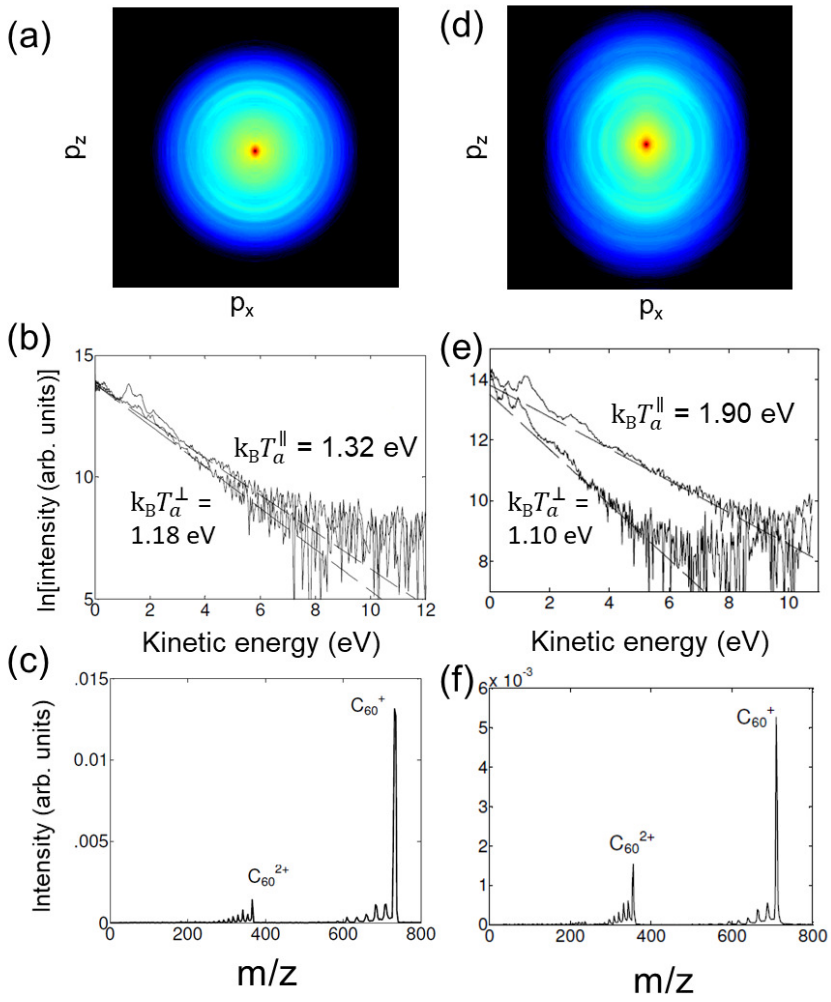

FIGURE 1.5: C_{60} mass spectra and PES taken using 400 nm (a)-(c) and 800 nm (d)-(f) 120 fs pulses. Top row: inverted VMI images plotted in logarithmic scale. Middle row: angular-resolved PES corresponding to the parallel and perpendicular directions with respect to the polarisation of the laser pulse (along p_z), plotted in a semi-logarithmic scale. Bottom row: Mass spectra. Figure adapted from Johanson *et al.*[28]

Pulse duration < 100 fs

For even shorter pulses (less than 100 fs), two different ionisation mechanisms are present depending on the laser intensity, and hence depending on the Keldysh parameter. For low intensities, direct multiphoton ionisation followed by above threshold ionisation is observed.[25] Whereas for higher intensities ($\approx 10^{14}$ Wcm^{-2}) the mechanism switches to tunneling ionisation.[8] The change of mechanism alters the PES from having a clear ATI peak structure to being structureless, Figure 1.6. Evidence of electron recollision has been reported for intensities that favor tunneling ionisation which result in high charged species and low fragmentation in the mass spectra.[29,30]

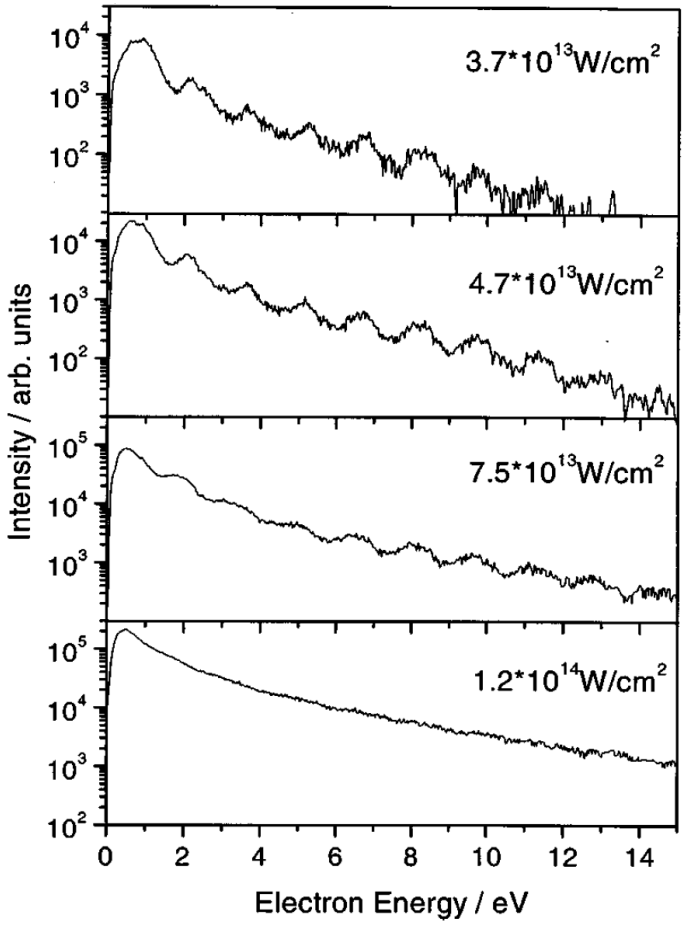

FIGURE 1.6: Laser intensity dependence of the C_{60} PES using 790 nm 25 fs pulses, plotted on a semi-logarithmic scale. The ATI structure is seen at lower intensities (a)-(c) while no structure is seen for higher intensities (d). Figure adapted from Campbell *et al.*[8]

1.3 Rydberg Fingerprint Spectroscopy

Rydberg states are highly excited, diffuse electronic states that have been observed in atoms and molecules which have symmetries that are comparable to the hydrogen atom's atomic orbitals. For the case of a hydrogen atom, the excited electron moves along a Coulomb potential of a point charge (V(H-atom)

in Figure 1.7). However, due to the electrostatic interactions of all the components in a molecule, the Coulomb potential at short distances differs greatly from that of the hydrogen atom (V(molecule) in Figure 1.7). Hence at short distances, this difference leads to a phase shift between the wavefunction in the hydrogen atom (top trace) compared to the molecule (bottom trace), resulting in a shift of the energy levels from E down to E′.[31] The Rydberg level's binding energy can be approximately described by the quantum defect formula,

$$E_B = \frac{R_y}{(n-\delta)^2}, \tag{1.5}$$

where R_y = 13.606 eV is the Rydberg constant, n is the principal quantum number of the electron and δ is the quantum defect. The exact phase shift, and thus quantum defect, is sensitive to the spatial arrangement, type and number of atoms in a molecule and also on the Rydberg orbital's angular momentum state.[31,32] Therefore, by measuring the binding energy of a Rydberg state and comparing these results with theoretical calculations, a 'fingerprint' of the molecule's structure can be obtained. This is the principle of the Rydberg fingerprint spectroscopy which was first described by Kuthirummal and Weber in 2003 using small organic molecules.[33] This technique has since then proven to provide structural sensitivity to large scale molecular systems such as polycyclic aromatic hydrocarbons and fullerenes.[32,34–36]

In Rydberg fingerprint spectroscopy, the Rydberg levels are accessed indirectly from the ground electronic state. An example schematic ionisation scheme is displayed in Figure 1.8 for the case of C_{60}. Through a multiphoton excitation, a band of high energy states (S_N) are populated directly from the ground state

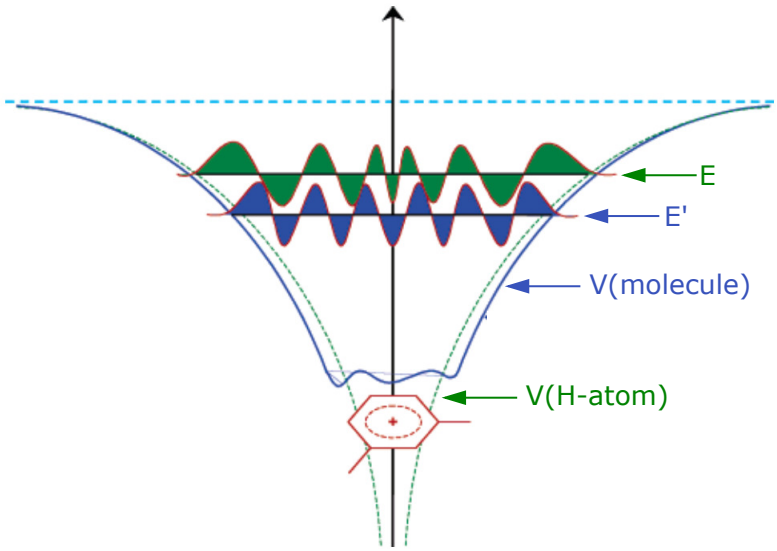

FIGURE 1.7: Comparison of the Coulomb potential energy diagram of a hydrogen atom (V(H-atom) with that of a molecule V(molecule). With respect to the molecular structure, phase shifts are experienced between the wavefunction of the hydrogen atom (top trace) and the Rydberg state (bottom trace), resulting in a lowering of the energy from the hydrogen atom E to the Rydberg state E'. Figure adapted from Gosselin *et al.*[32]

(S_0). These high energy states have very short lifetimes and decay through nonradiative internal conversion (IC) to lower singlet state series, populating a range of vibrational levels. An additional photon then ionises the molecule and gives rise to the ground electronic state of a vibrationally excited ion. Due to the fast timescales of all the processes, the above mechanism occurs within the same sub-ps laser pulse. Since these state series are populated indirectly, the final ionisation process can be approximated to be a single-photon ionisation.[17] Since the electron in the Rydberg state is only loosely bound to the cationic centre, the Rydberg and ionic states have almost identical potential energy surfaces. Hence, from the Franck-Condon arguments the vibrational

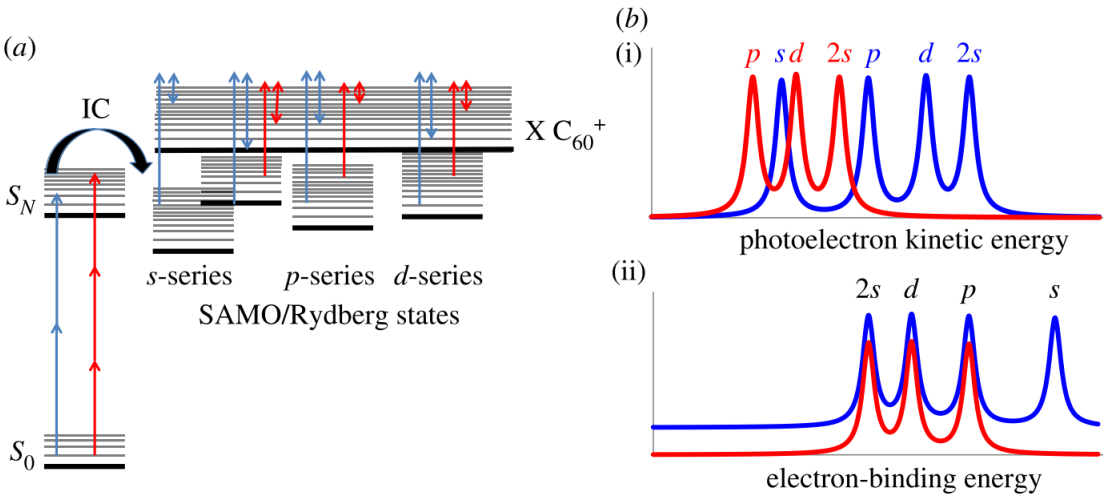

FIGURE 1.8: (a) Energy level diagram explaining the principles of Rydberg fingerprint spectroscopy in C_{60}. Two examples are shown: blue, two photon excitation and red three photon excitation. (b) (i) PES with respect to the photoelectron kinetic energies and (ii) PES with respect to the electron binding energies. Figure adapted from Johansson *et al*.[35]

energy is conserved in the ionisation step, $\Delta\nu = 0$.[37] This is demonstrated by the double headed arrows in Figure 1.8 (a), which indicate the kinetic energy of the photoelectron. Because of this indirect population of the Rydberg states, Rydberg fingerprint spectroscopy is insensitive to the excitation energy that is used in an experiment. For instance, in Figure 1.8 two different excitation energies are used to access the Rydberg states, pictorially seen as the red and blue arrows. Even though that the kinetic energies of the photoelectrons will be different (b)(i), the binding energies will be the same (b)(ii).

In this thesis, Rydberg fingerprint spectroscopy has been used to investigate in more detail the Rydberg series in fullerenes that Boyle *et al* had identified in C_{60} when using ps excitation, Figure 1.9, and Johansson *et al* had further studied using fs excitation.[27,38] Later on, the lowest energy Rydberg states were named

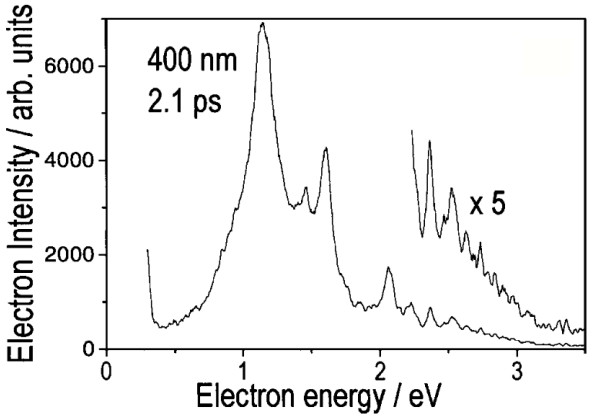

FIGURE 1.9: First observation of a Rydberg series in the PES of C_{60} using 2.1 ps 400 nm pulses. Figure adapted from Boyle *et al.*[38]

the Super-Atom Molecular Orbitals (SAMOs).[27]

1.4 Super-Atom Molecular Orbitals of fullerenes

1.4.1 Discovery

The SAMOs are low-lying, atomic-like, diffuse excited electronic states that have been observed on hollow molecules. SAMOs were first identified by Feng *et al* in a low-temperature scanning tunnelling microscopy (LT-STM) study of C_{60} molecules adsorbed on a copper surface, where they recorded images of atomistic orbitals that extended beyond the individual fullerene molecules, Figure 1.10.[39] They are classified as low-lying members of the Rydberg series found in hollow molecules.[40] The main difference between conventional Rydberg states and the SAMOs is that the SAMOs have a significant part of their electron density localised at the centre of the cage, in contrast to Rydberg

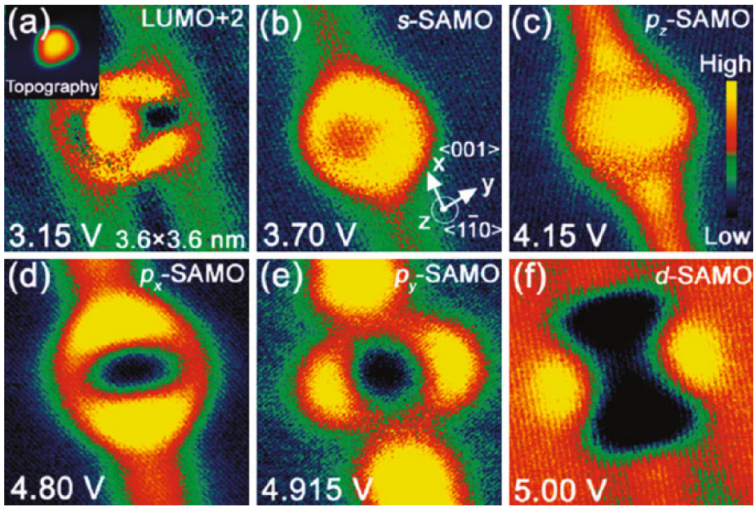

FIGURE 1.10: LT-STM images of the SAMOs in C_{60}. The C_{60} molecules were adsorbed on a partially oxidised Cu(110)-(2x1)-O surface. Figure adapted from Feng *et al.*[39]

states where their electron density is localised far away from the molecular core.[39,40] The above is demonstrated in Figure 1.11 where the charge density of the molecular orbitals has been plotted against the distance from the centre of the cage. To aid with the visualisation, the molecular orbitals are provided as well on the right hand side.[40] This difference arises due to a spherically symmetric potential which is created by the highly symmetric and hollow structure of the C_{60} molecule. This shallow attractive potential is the result from the summation of the long range interactions between electrons on opposite sides of the cage and the Coulomb potentials that are localised on each carbon atom.[40–42]

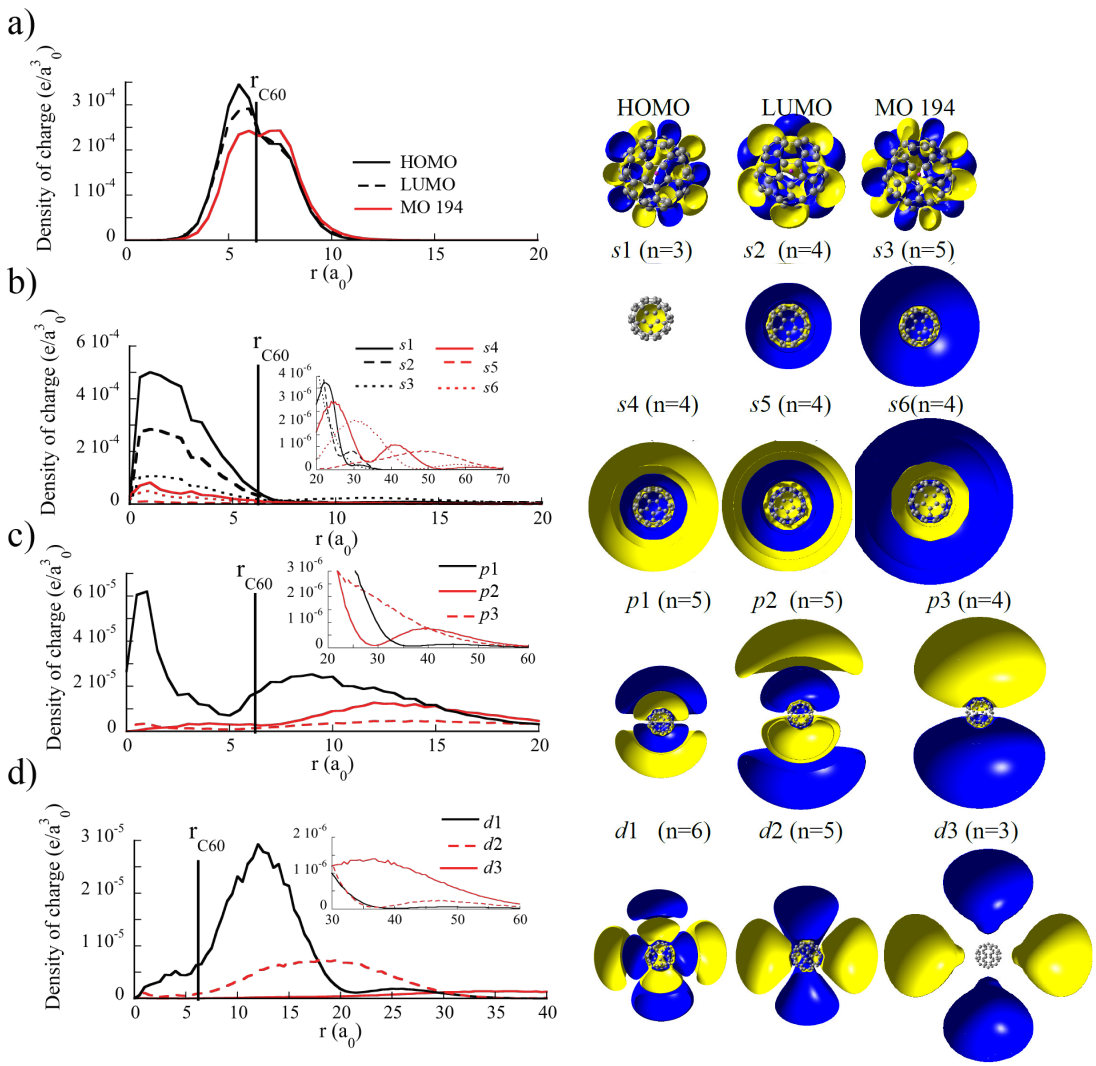

FIGURE 1.11: Charge density of the molecular orbitals of C_{60} plotted against the distance from the centre of the cage, where 0 is the centre. The vertical line indicates the radius of the cage. (a) Non-SAMO orbitals, (b) s-band states, (c) p-band states and (d) d-band states. In (b)-(d) the black traces represent the SAMOs while the red traces the Rydberg states. The corresponding molecular orbitals are plotted on the right hand side of the figure. Figure adapted from Mignolet *et al.*[40]

1.4.2 Gas-phase excitation mechanism

When C_{60} molecules are subjected to sub-ps excitation, the resulting photoelectron spectra are characterised as a peak structure that is superimposed on an exponentially decreasing thermal background. This peak structure originates from ionisation from the SAMOs. Studies of vibrationally cold fullerenes, however, show no peak structure on the photoelectron spectra.[43,44] This implies that a high vibrational energy and efficient coupling between the different states within the Rydberg fingerprint spectroscopy scheme may be required for the SAMO states to be populated.

From a computational investigation it was found that SAMO states have roughly three orders of magnitude larger photionisation widths compared to non-SAMO states, Figure 1.12. In addition, their photoionisation lifetimes are comparable to the fs pulse duration. This explains their dominance in the PES as well as why photoionisation from excited non-SAMO states does not occur within the ultrashort laser pulse duration used in these experiments.[40] However, the low photoionisation rate from these excited valence states could play an important role in the thermal electron emission scheme. Excitation energy could be accumulated statistically over time within these valence states and once the energy is larger than the binding energy of the state, an electron is emitted.

1.4.3 SAMOs of fullerene derivatives and their applications

SAMOs are not unique to C_{60} molecules. They have been observed in gas-phase, solid-state and theoretical investigations of larger fullerenes and fullerene derivatives.[27,40,45–53] A few different examples are displayed in Figure 1.13.

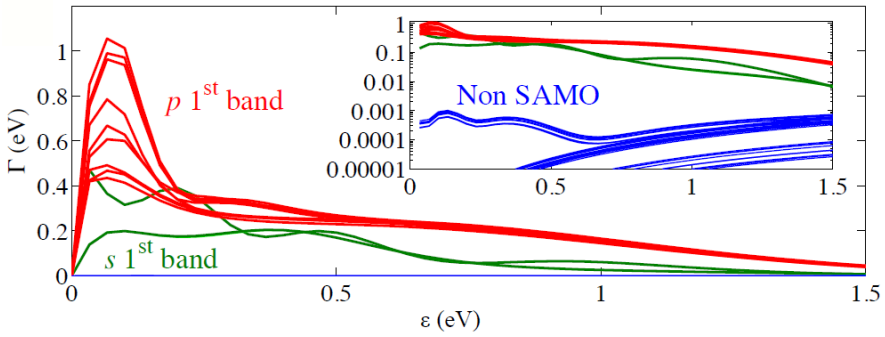

FIGURE 1.12: Photoionisation width of the SAMO and non-SAMO states in C_{60} as a function of the kinetic energy of the photoelectrons. A semi-logarithmic plot is displayed in the inset. Figure adapted from Mignolet *et al.*[40]

From gas-phase experiments, left hand side, evidence for SAMOs was found in the fs PES of C_{70}, C_{82} and $Sc_3N@C_{80}$.[51] While in STM and STS measurements of molecules adsorbed on a metal substrate, SAMOs were found in $La@C_{82}$ (top right) and $Sc_3N@C_{80}$ (bottom right).[47,53]

Particular interest has been shown in the potential applications that SAMOs could have in the fabrication of molecular electronics and molecular switching devices. It has been found that when fullerenes are adsorbed on surfaces, C_{60} SAMOs hybridise to form nearly free electron bands in 1-D quantum wires and 2-D quantum wells, Figure 1.14 left hand side.[45,46] Due to the fact that SAMOs are more diffuse compared to the valence σ or π orbitals, they possess an enhanced charge delocalisation and hence devices utilising the nearly free electron bands in fullerenes could be used for charge transport applications. Furthermore, the endohedral fullerene $Sc_3N@C_{80}$ has been shown to act as a single-molecule switching device which would make a strong candidate for advanced high density memory applications. Conformational changes occur

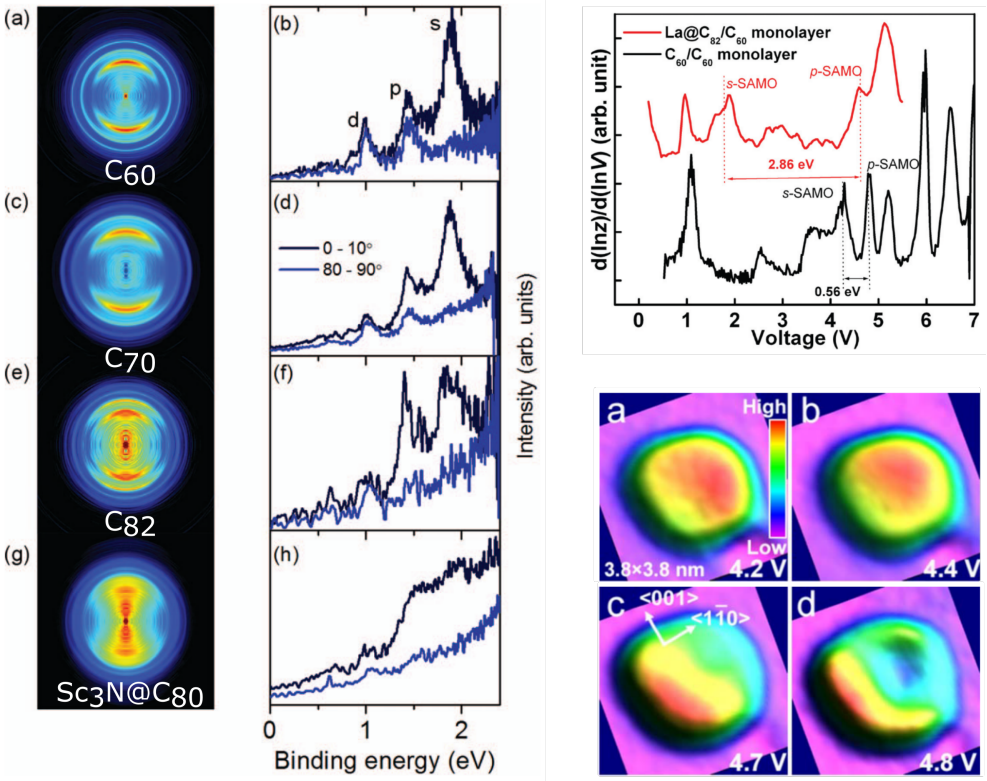

FIGURE 1.13: Observation of SAMOs on other fullerenes and endohedral fullerenes. Left hand side: VMI images and angle-resolved PES of C_{60}, C_{70}, C_{82} and $Sc_3N@C_{80}$. The marked peaks correspond to the s-, p- and d-SAMOs. Right hand side, top: STS spectra of isolated C_{60} (black curve) and $La@C_{82}$ (red curve) molecules that are adsorbed on a C_{60} monolayer which in turn is adsorbed on a Cu(111) surface. Right hand side, bottom: STM imaging showing the local density of states of the SAMOs of an isolated $Sc_3N@C_{80}$ molecule adsorbed on a partially oxidised Cu(110)-(2x1)-O surface. (a) and (b) correspond to an s- or p_z-SAMO, (c) and (d) correspond to a p_x- or p_y-SAMO. Figures adapted from Johansson *et al* (left hand side),[51] Feng *et al* (right hand side, top)[47] and Huang *et al* (right hand side, bottom).[53]

only within the hollow cage by affecting the geometrical position and orientation of the endohedral molecule.[54,55] This results in having minimal environmental perturbations during a switching event, an attractive attribute given that most other single-molecular switches function by having huge structural

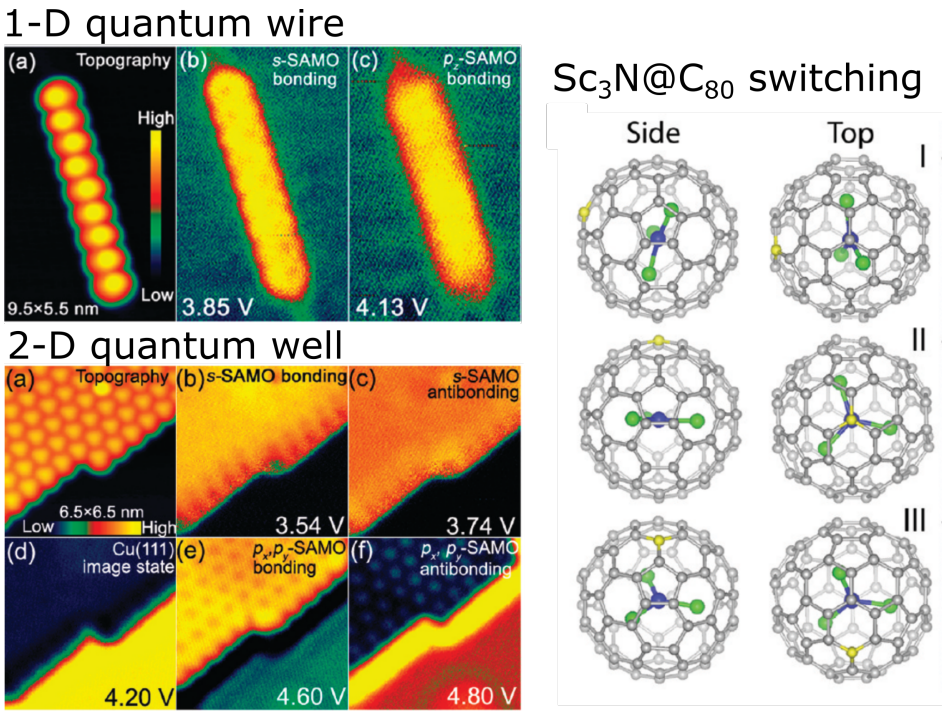

FIGURE 1.14: Molecular electronics and switching applications for SAMOs. Left hand side: STM images of the C_{60} SAMO 1-D quantum wires (top) and 2-D quantum wells (bottom). Right hand side: structures of the 6 different switching positions in $Sc_3N@C_{80}$. Figures adapted from Feng *et al* (left hand side)[46] and Huang *et al* (right hand side).[54]

changes. For instance, on the right hand side of Figure 1.14 the six different orientations of the endohedral molecule in the switching of $Sc_3N@C_{80}$ is shown. The switching mechanism is based on the rotation of the encapsulated molecule along two different axis.

2 Methods

2.1 Laser Setups

In this section, the basic theory behind how ultrashort laser pulses can be generated using the chirp pulse amplification (CPA) technique will be explained. Additional laser systems which manipulate the frequency, the pulse duration and the bandwidth of the fundamental output are described. These involve a harmonic generation stage, a non-collinear optical parametric amplifier (NOPA) and a second harmonic bandwidth compressor (SHBC). Further equipment and methods used to characterise the nature of the pulses will be presented.

2.1.1 Femtosecond oscillator and regenerative amplifier laser

At it's core, a laser system makes use of a gain medium with specific properties to support a population inversion mechanism. In order to achieve this phenomenon, a pumping mechanism is in place which supplies enough energy for the population inversion to be maintained and results in a lasing output.

Originating from the uncertainty principle, the relationship between the temporal and spectral attributes of a pulse of light are defined by the time-frequency

Fourier relationship,

$$\Delta\nu\Delta t \geq K, \tag{2.1}$$

where $\Delta\nu$ is the full width half maximum (FWHM) of the bandwidth in frequency space, Δt is the FWHM of the pulse duration and K is a constant number defined by the spectral profile of the pulse (K = 0.441 for Gaussian profile pulses and K = 0.315 for sech^2 profile pulses).[56] In the present experimental setup, Gaussian profile pulses provide a better fit to the data.

For the generation of ultrashort laser pulses, titanium-dopped sapphire (Ti:Sapph, Ti:Al_2O_3) is the most commonly used gain medium due to its large emission bandwidth and its high damage threshold. The crystal is pumped in the region of 500-550 nm where it has an absorption maximum. Usually the second harmonic (532 nm) of a Nd:YAG pump laser is used.[56]

The technique of first stretching, then amplifying and in the end recompressing a laser pulse is termed chirped pulse amplification (CPA).[57] Ultrashort, high intensity laser pulses can be generated with this method. Donna Strickland and Gérard Mourou were awarded the Nobel Prize in Physics in 2018 for developing this technique. A simplified schematic diagram of CPA is presented in Figure 2.1 (a).

The femtosecond laser system used in the present study is commercially produced by Coherent, Inc. It is comprised of a Ti:Sapph oscillator (Mantis) which is pumped by the second harmonic of a Nd:YAG continuous wave laser (532 nm, OPS laser). The Mantis produces high peak intensity, sub-35 fs pulses with

a central wavelength at 800 nm, a bandwidth of 80 nm and a repetition rate of 80 MHz. The optical spectrum of the Mantis is shown in Figure 2.1 (b). This output is directed into the regenerative amplifier (Regen, Legend) where it acts as a seed beam for the amplifying process. Before the seed pulses can interact with the amplifying medium, a Ti:Sapph crystal, their intensities need to be reduced below the damage threshold of the crystal. This is achieved by first directing the seed beam into the pulse stretcher, consisting of a single diffraction grating. By double passing the beam onto the grating, a positive chirp is added to the pulses, stretching them in time and thus decreasing the peak intensity. The seed pulses are subsequently directed into the amplifying cavity where they interact with a Ti:Sapph crystal which is pumped by the second harmonic of a Nd:YLF 1 kHz pulsed laser (532 nm, Evolution laser). A single pulse is confined within the cavity (bounces between the two end mirrors) due to it's polarisation. As such, the pulse passes through the crystal for a number of round trips, typically 10-15, where its intensity is amplified with each pass. Once the pulse reaches its maximum intensity, a gain in the range of 10^6, its polarisation is changed with the use of Pockels cells. The pulse is allowed to exit the cavity by reflecting off a polariser and is directed towards the pulse compressor. In that final stage, the dispersion introduced by the stretcher is compensated using a single diffraction grating that induces an opposite chirp to the initial one.[56] This generates a recompressed 120 fs pulse with a central wavelength at 800 nm, a bandwidth of 11 nm, a repetition rate of 1 kHz and a polarisation that is parallel to the plane of the laser table (horizontal, p-polarised). Figure 2.1 (c) displays the optical spectrum of the Legend. In addition, the compressor settings can be manually detuned to induce a chirp in

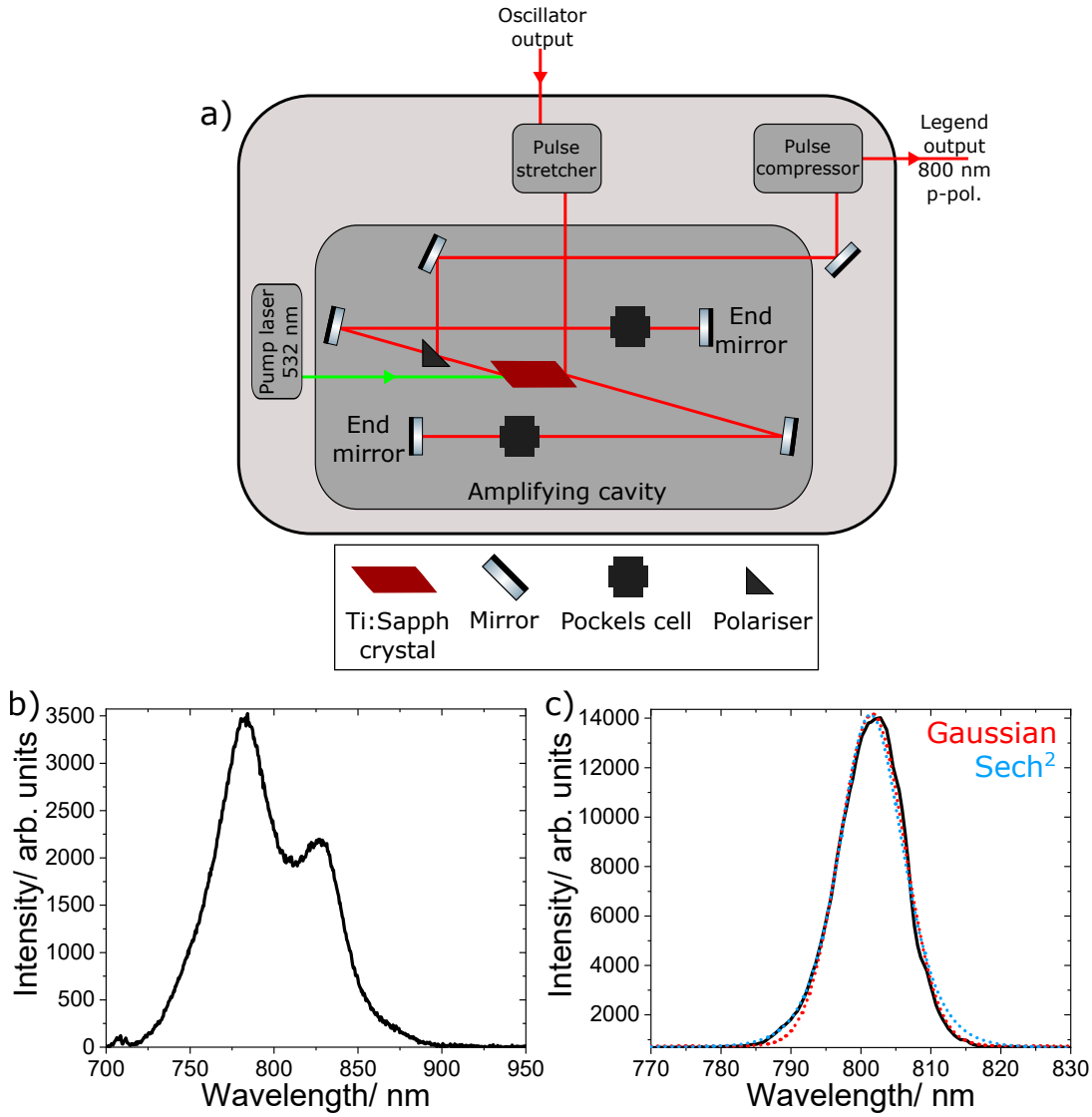

FIGURE 2.1: (a) Schematic diagram of the CPA technique. (b) Optical spectrum of the oscillator laser (Mantis). (c) Optical spectrum of the regenerative amplifier (Legend). Gaussian (red dotted line) and $Sech^2$ (blue dotted line) distributions have been fitted yielding a central wavelength of 802 nm FWHM 11 nm.

the pulses and thus obtain a longer pulse duration. The maximum pulse duration that was able to be achieved and measured with the available equipment in the lab was 5 ps.

2.1.2 Frequency conversion

A medium's dielectric polarisation, $\overrightarrow{\mathbf{P}}$, response to the laser's radiation electric field, $\overrightarrow{\mathbf{E}}$, which is passing through the medium is expressed as,

$$\overrightarrow{\mathbf{P}} = \varepsilon_0[\chi_1 \overrightarrow{\mathbf{E}} + \chi_2 \overrightarrow{\mathbf{E}}^2 + \chi_3 \overrightarrow{\mathbf{E}}^3 + ...], \tag{2.2}$$

where ε_0 is the permittivity of free space, χ_i are the i^{th}-order electric susceptibilities and the electric field is expressed as,

$$\overrightarrow{\mathbf{E}} \propto E_0 \exp(i\omega t) + E_0^* \exp(-i\omega t), \tag{2.3}$$

where E_0 is the amplitude and ω is the angular frequency of the electric field (photon energy is equal to $\hbar\omega$). In the polynomial expansion, the first-order linear term describes linear optical effects such as reflection or absorption, while the higher-order non-linear terms describe non-linear optical effects such as harmonic generation.[56] For low intensity electric fields, only the first term of the polynomial expansion dominates while the rest are negligible due to the small values of the higher-order susceptibilities. When the high intensity electric fields present in ultrashort pulses are incident on birefringent crystals, for example a BBO (β-barium borate) crystal, the higher-order terms become non-negligible and non-linear effects become more significant. In order for these non-linear effects to be dominant, the energy ($\propto w$) and momentum, $\overrightarrow{k}$, of the photons must be simultaneously conserved. A phenomenon known as phase-matching.[56]

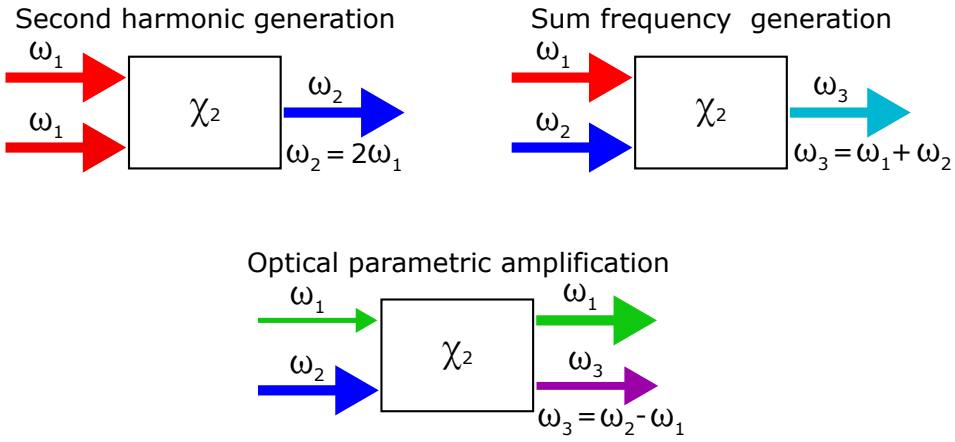

FIGURE 2.2: Examples of non-linear optical processes that are governed by the second-order susceptibility of a non-linear optic.

In the following sections, the focus will be kept on the second order term as the second-order susceptibility plays an important role in explaining the physics behind various different non-linear optical effects that were used in this thesis (see Figure 2.2).

Harmonic Generation

Assuming that two beams of different energies are present in a medium, the electric field will be equal to,

$$\vec{\mathbf{E}} = E_1 \exp(i\omega_1 t) + E_1^* \exp(-i\omega_1 t) + E_2 \exp(i\omega_2 t) + E_2^* \exp(-i\omega_2 t), \qquad (2.4)$$

where ω_1 and ω_2 correspond to the angular frequencies of the two beams. By substituting Equation 2.4 into the second term of Equation 2.2, the following output processes are resulted,

$$\begin{aligned}\frac{\overrightarrow{\mathbf{P}}_2}{\varepsilon_0} &= \chi_2 \left[E_1^2 \exp(2i\omega_1 t) + E_1^{*2} \exp(-2i\omega_1 t)\right] \\ &+ \chi_2 \left[E_2^2 \exp(2i\omega_2 t) + E_2^{*2} \exp(-2i\omega_2 t)\right] \\ &+ \chi_2 \left[2E_1 E_2 \exp(i(\omega_1 + \omega_2)t) + 2E_1^* E_2^* \exp(-i(\omega_1 + \omega_2)t)\right] \\ &+ \chi_2 \left[2E_1 E_2 \exp(i(\omega_1 - \omega_2)t) + 2E_1^* E_2^* \exp(-i(\omega_1 - \omega_2)t)\right] \\ &+ \chi_2 \left[2|E_1|^2 + 2|E_2|^2\right].\end{aligned} \tag{2.5}$$

The terms in the first and second lines describe the second harmonic generation (SHG) of the two individual beams respectively. The terms in the third and fourth lines describe the sum frequency generation and difference frequency generation of the two beams respectively. The terms in the last line describe optical rectification which results in no optical output. Each of the above different processes becomes dominant only when a specific phase-matching condition is met. Their efficiency also depends on the physical properties of the medium that they take place in. They cannot all occur simultaneously.[56]

In the SHG process, two photons of frequency ω_1 are destroyed while one photon of frequency $\omega_2 = 2\omega_1$ is produced. The third harmonic generation (THG) process is an example of a sum frequency generation where one photon of frequency ω_1 and one photon of frequency $\omega_2 = 2\omega_1$ are destroyed to produce one photon of frequency $\omega_3 = 3\omega_1$.

In the harmonic generation stage of the laser setup, the second (400 nm) and third (267 nm) harmonics of the fundamental (800 nm) can be generated. With the SHG crystal, two 800 nm photons are destroyed to produce one 400 nm photon whose polarisation is rotated by 90°. In the present setup, roughly 20% of the incident radiation is converted to 400 nm photons. In order to separate

the remaining 800 nm photons, a series of mirrors that reflect well at 400 nm and transmit well at 800 nm are used to direct the beam into the interaction chamber. Figure 2.3 (a) shows the schematic diagram for the SHG stage while (c) shows the optical spectrum obtained from 400 nm, 120 fs pulses.

To obtain the third harmonic, the fundamental and second harmonic have to frequency mix inside a second BBO crystal. In order for this to happen, the two different frequencies need to be together in time and have the same polarisation. Due to the fact that the refractive index of the BBO crystal varies with wavelength, the 400 nm photons have been temporally retarded compared to the 800 nm photons. This phenomenon is called group velocity delay. A calcite plate is used to compensate for this. As the polarisation of the 800 nm and 400 nm photons are perpendicular, a specially coated $\lambda/2$ waveplate is used which only rotates the polarisation of the fundamental. As a result the two beams can now interact in the THG crystal to produce 267 nm photons.[56] In order to separate the harmonics, specially coated mirrors that reflect well 267 nm and transmit well 400 and 800 nm are used to direct the beam into the interaction chamber. Figure 2.3 (b) shows the schematic diagram for the THG stage while (d) shows the optical spectrum obtained from 267 nm, 120 fs pulses.

The harmonic generation stage is placed right after the telescope in the overall laser table optical configurations in Figures 2.9 and 2.10.

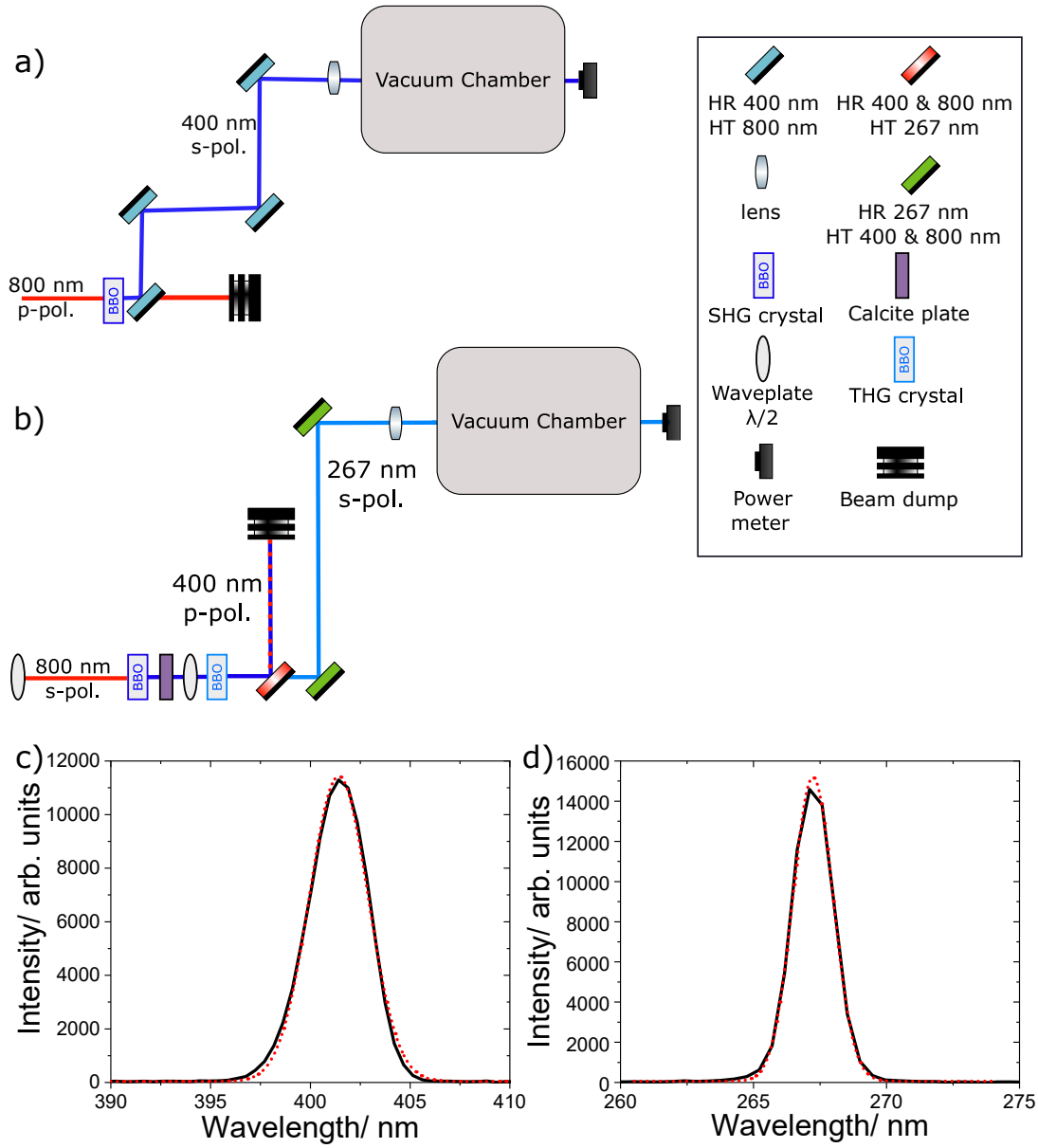

FIGURE 2.3: Schematic diagram of the (a) second and (b) third harmonic generation stage together with their respected optical spectra, (c) and (d) respectively. Gaussian curves have been fitted on the two spectra (red dotted line) yielding a central wavelength of 401 nm FWHM 3 nm for (c) and 267 nm FWHM 2 nm for (d).

TOPAS fs

Optical parametric amplification (OPA) is an additional process which is governed by the second-order susceptibility of the birefringent material (see Figure 2.2 for a schematic diagram). When a weak seed pulse, ω_1, and an intense

pump pulse, ω_2, interact together while having the frequency of the pump pulse larger than that of the seed pulse, OPA is achieved. This results in one pump photon being destroyed while two photons, one of frequency ω_1 and one of $\omega_3 = \omega_2 - \omega_1$, are created. As a result the intensity of the weak seed pulse is amplified. By adjusting the angle of incidence between the two light beams and the axes of the birefringent material, output wavelength tunability is possible.

A commercial non-collinear optical parametric amplifier (NOPA) (Light Conversion, Topas-White) is used to create fs pulses of tunable wavelength ranging between 500-1000 nm. The pulse duration depends on the specific wavelength and has a range of 35-70 fs. The Topas-White optical layout is shown in Figure 2.4. The incoming 800 nm light (red beam) is split using a beamsplitter, a small part of which is focused on a sapphire plate to produce the white light continuum (WLC, grey beam) and the remaining is converted to 400 nm using a SHG crystal (blue beam). The WLC beam passes through a pulse-phase shaper which adds a nonlinear negative chirp. The WLC acts as a seed beam to the two stage parametric amplifier which makes use of a single BBO crystal. The 400 nm beam is split into two, path A and B in the figure, which pump the first and second parametric amplification stages respectively. In path A, the pump beam is overlapped non-collinearly with the WLC to produce a signal pulse. In path B, that signal pulse is overlapped non-collinearly with the second pump beam to amplify its intensity. Finally, the output signal passes through a compressor which compensates for the induced negative chirp, producing transform limited pulses. The output wavelength can be tuned by adjusting the time delay between the two beams in the first parametric amplification stage

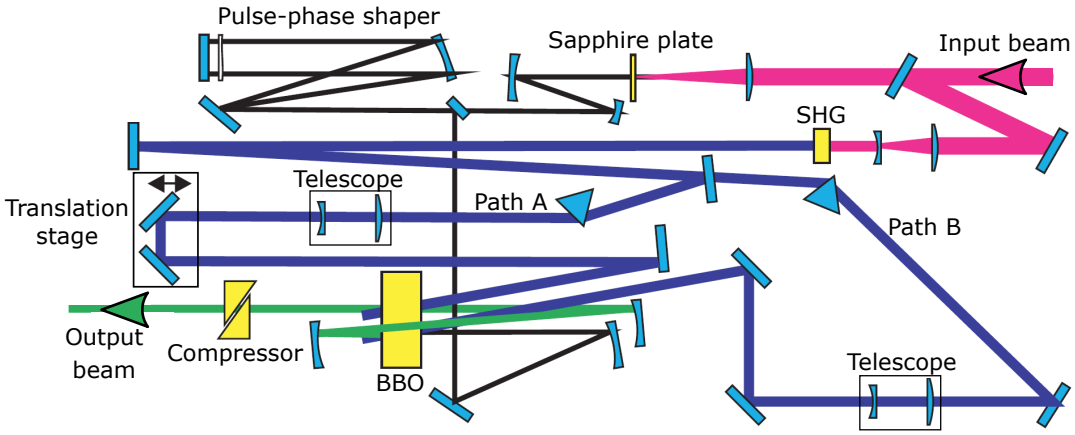

FIGURE 2.4: Schematic diagram of the OPA optical layout. Red beam = 800 nm, grey beam = WLC, blue beam = 400 nm and green beam = OPA output. Figure adapted from the Topas-White manual.[58]

together with fine tuning the crystal angle. The output beam is directed into the interaction chamber according to the laser table optical configuration in Figure 2.11 (a).

SHBC

The second harmonic bandwidth compressor (SHBC) unit manufactured by Light Conversion, produces 400 nm narrowband ps pulses. The working principle of the SHBC is the mixing of two phase conjugated pulses into a SHG crystal; pulses that have an equal but opposite temporal chirp. The incoming 800 nm, 120 fs beam is split in half using a 50/50 beamsplitter and each beam is directed onto a set of diffraction gratings that induce respectively an equal in magnitude positive and negative chirp to each pulse. Once the pulses have been matched in time, they are directed with a non-collinear geometry to the SHG crystal. This results in 3 beams being produced; the two side ones

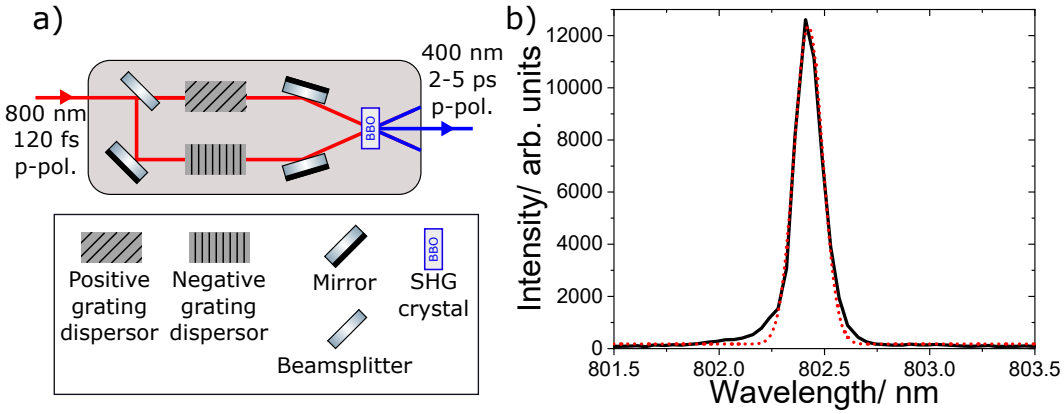

FIGURE 2.5: (a) Schematic diagram of the SHBC mechanism. (b) Second order diffraction spectrum. A Gaussian curve has been fitted (red dotted line) on the spectrum yielding a central wavelength of 401.22 nm FWHM 0.09 nm.

correspond to the SHG of each individual beam, while the middle one is the chirp-free second harmonic resulted from the mixing of the two initial beams. As such, 2-5 ps pulses can be produced with a bandwidth of 5 cm^{-1}. Figure 2.5 shows the schematic diagram of the SHBC together with its spectrum. It should be noted that because of the higher resolution requirements, a spectrometer that measures the second order diffraction is used. The output beam from the SHBC is directed into the interaction chamber according to the laser table optical configuration in Figure 2.11 (b).

2.1.3 Laser beam characterisation

Determining the pulse duration

For measuring the duration of an ultrashort pulse in the fs-ps regime, one cannot use electronic devices as their measurable limit is far longer than the pulse itself (around 1 ns). Rather, one needs to utilise optical methods such as the

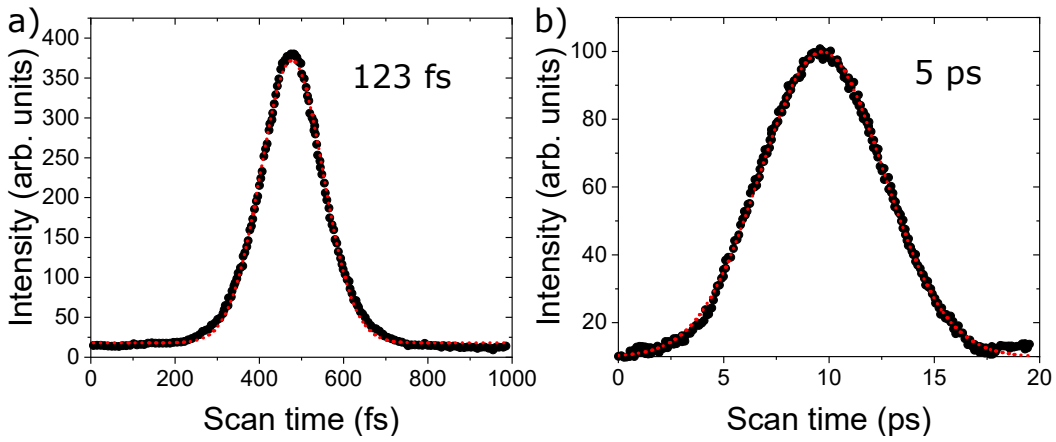

FIGURE 2.6: Measured second order autocorrelation of the 800 nm beam recorded for two different pulse durations: (a) 123 fs and (b) 5 ps. These values are the deconvoluted FWHM.

one described in this thesis, the autocorrelation of the input beam. The principle of operation is as follows. The incoming beam is divided into two equal intensity beams that follow different paths before being overlapped collinearly in a SHG crytal. Given that the intensity of the second harmonic is dependent on the temporal overlap of the two pulses, a temporal delay is introduced between the pulses and the resulting intensity is measured as a function of said delay time. Hence the convoluted second order autocorrelation of the input beam can be measured. To obtain the true deconvoluted FWHM of a Gaussian profile pulse, one has to divide the measured FWHM by $\sqrt{2}$.[56] Figure 2.6 displays typical autocorrelated spectra taken within this study using a commercial autocorrelator (APE Pulsecheck).

Determining the beam waist and laser intensity

When performing an experiment, it is vital to be able to present the results in a way that they can be compared with similar experiments undertaken in

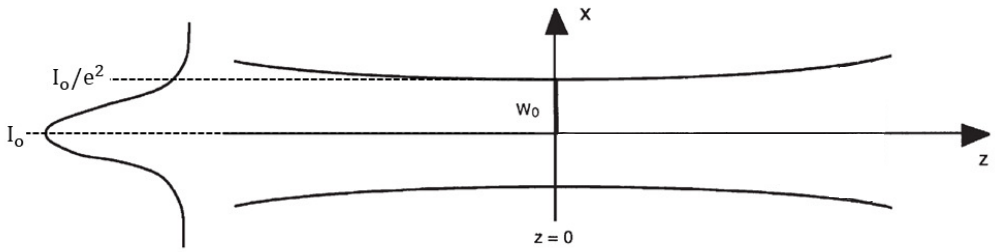

FIGURE 2.7: Beam waist diagram for a Gaussian profile beam in the focal region. The beam is propagating along the z-axis and at z = 0 the intensity of the beam is $1/e^2$ of the maximum intensity. The radius of the beam at z = 0 is termed the beam waist, w_0. A Gaussian curve is shown on the left hand side for completeness. Figure adapted from Rullière .[56]

different laboratories and with different experimental setups. In the case of a photophysical or photochemical experiment (or an experiment that uses laser light), one needs to present their results in terms of the laser intensity in the interaction region rather than the total laser power. There are several different techniques that can be used to determine the laser intensity. In this study it was determined by recording the beam profile in the focus of the beam using a camera and calculating the beam waist.

For a Gaussian profile beam propagating along the z-axis, the beam waist is defined as the radius at which the laser power is equal to $1/e^2$ of the maximum peak power, Figure 2.7.[56]

To make the derivations easier, several qualities of a Gaussian profile beam will now be described. The intensity of the beam at a given position away from the centre is described by,

$$I(x,y) = I_0\, exp\left[-2\frac{(x-x_0)^2+(y-y_0)^2}{w_0^2}\right], \tag{2.6}$$

where I_0 (in Wcm^{-2}) is the peak intensity at the centre of symmetry of the beam (the coordinates being x_0, y_0) and w_0 is the beam waist. The peak intensity is equal to,

$$I_0 = \sqrt{\frac{16ln(2)}{\pi}} \times \frac{E_P}{\Delta t\, \pi\, w_0^2} \approx 1.8789 \times \frac{E_P}{\Delta t\, \pi\, w_0^2}, \tag{2.7}$$

where E_P is the total energy of the pulse (in J) and Δt is the pulse duration (in s). After having determined the laser intensity in the focus, the laser fluence, F (in Jcm^{-2}), which is defined as the energy per area can be calculated from,

$$F = \sqrt{\frac{\pi}{4ln(2)}} \times \Delta t \times I_0 \approx 1.0645 \times \Delta t \times I_0. \tag{2.8}$$

A CMOS camera was placed at various positions along the beam propagation direction (z-axis) near the focus of the beam and the actual beam profile was recorded. Using a Matlab code written by Florian Liedy, a Guassian function was fitted along the *x*- and *y*-axes of the image to obtain the beam waist for those two directions. This was repeated for all the positions of the camera along the z-axis and the smallest value was used as the true beam waist. Figure 2.8 shows an image of the beam profile together with the fitted Gaussian curves for the two directions.

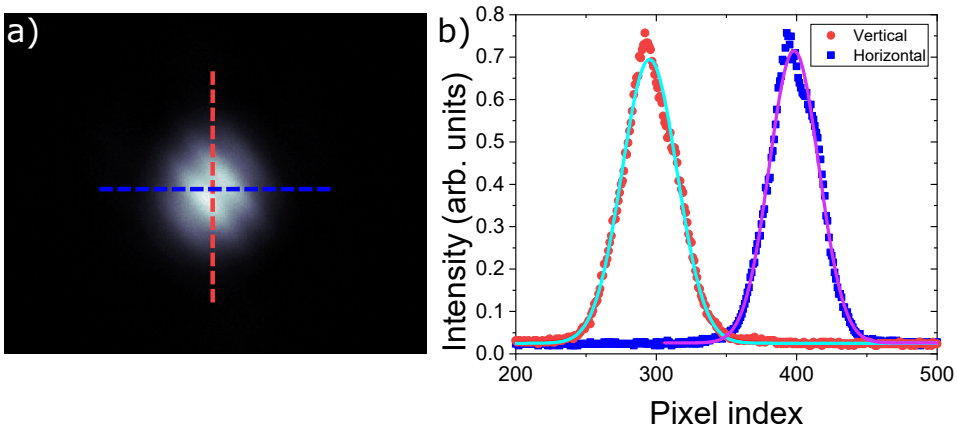

FIGURE 2.8: (a) Beam profile of the 400 nm SHBC laser beam that was focused using a 1 m focal length concave mirror onto a CMOS camera. (b) A cut through the vertical (red) and horizontal (blue) directions of the beam profile in (a). Gaussian functions have been fitted (solid lines). Given that 1 pixel = 2.2 µm, the vertical beam waist = 77 $\pm$ 4 µm and the horizontal beam waist = 86 $\pm$ 4 µm.

2.1.4 Optical setup

All the above laser setups or instruments made use of a single output from the regenerative amplifier. In order to be able to interchange between them or use them simultaneously, the output from the Regen was split using several beam-splitter optics. An overview of the laser table with various different optical arrangements are shown in Figures 2.9, 2.10 and 2.11 below.

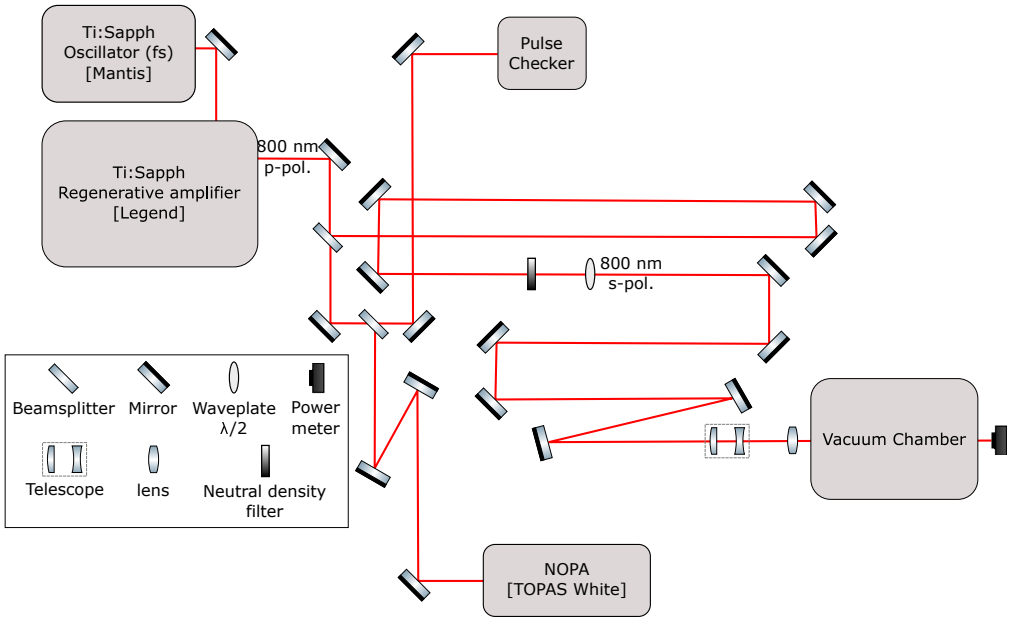

FIGURE 2.9: Schematic diagram of the layout of the laser table, version 1.

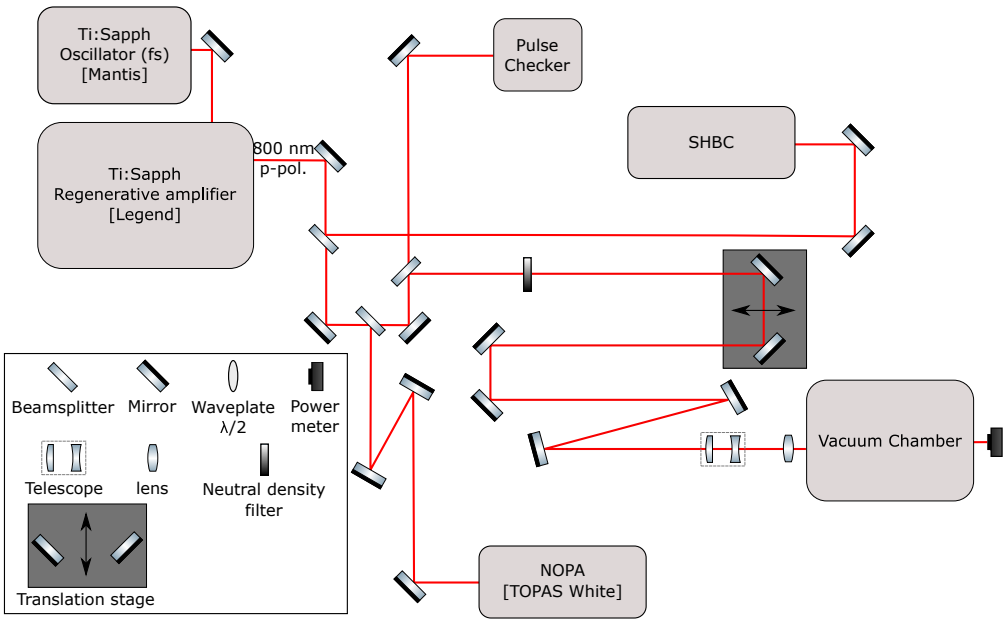

FIGURE 2.10: Schematic diagram of the layout of the laser table, version 2.

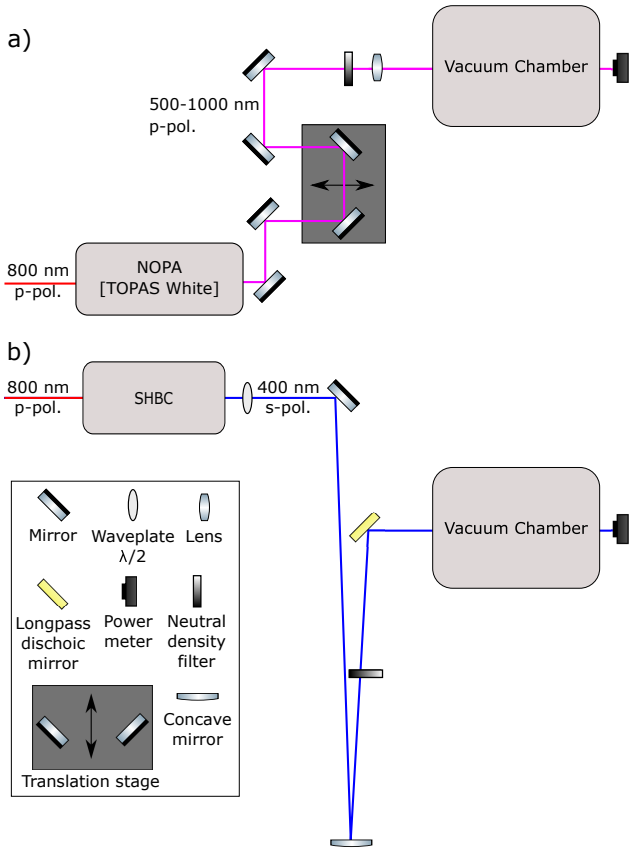

FIGURE 2.11: Schematic diagram of the layout of the laser table when (a) the TOPAS and (b) the SHBC beams are directed towards the interaction chamber.

A two-colour pump-probe setup, using an 800 nm fs pump beam from the Regen and a 400 nm ps probe beam from the SHBC, was built to investigate the dynamics of populating the SAMO states in C_{60}. A schematic diagram of the layout is displayed in Figure 2.12. In order to adjust and fine tune the temporal overlap between the two pulses, the 800 nm beam is aligned through a translation stage. The two focused beams are spatially overlapped inside the interaction chamber. The fs beam is focused using a 30 cm focal length lens and the ps beam using a 1 m focal length concave mirror. Although there was not enough time to perform the pump-probe experiment itself, results from testing the framework of this experiment are presented in Chapter 4.

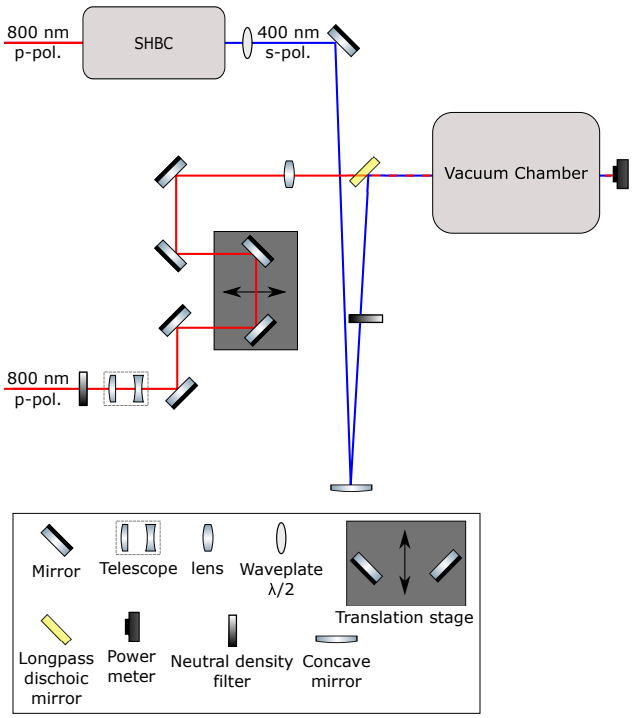

FIGURE 2.12: Schematic diagram of the pump-probe setup, using an 800 nm fs pump beam (from the Regen) and a 400 nm ps probe beam (from the SHBC).

2.2 Vacuum chamber

The main vacuum system used to acquire the mass spectroscopic and velocity map imaging data will be briefly described. The system was built and tested by Dr Olof J. Johansson as part of his PhD thesis. For the fully detailed description, the interested reader is referred to read his original work.[59]

The vacuum chamber can be divided into two parts: one being the hot source where the molecular beam is created by subliming the samples; and the other being the interaction chamber where the photoionisation events occur. In the latter is where the ion optics and two sets of detectors are situated. A schematic diagram is given in Figure 2.13. When no measurements are taking place, the pressure in both parts is no higher than 1.0×10^{-8} mbar. During a typical measurement, the pressure in the interaction chamber stays the same, while the pressure in the hot source is increased to 10^{-8}-10^{-7} mbar. When Xe gas is added for the kinetic energy calibration measurements, the pressure in the interaction chamber is adjusted to 10^{-7}-10^{-6} mbar. Within the hot source, the samples are placed inside a quartz ampule, which is then put inside a molybdenum rod. A heating wire is wrapped around the rod, which, when heated, can sublime the samples, creating a vertically moving molecular beam (shown by the brown arrow in Figure 2.13).

The C_{60} sample is purchased from SES Research and is 99.95% pure. The Li@C_{60} sample was purchased from Idea International as a $[Li@C_{60}]^+[PF_6]^+$ salt and is >80% pure. In order to create a desirably strong molecular beam density and avoid thermal decomposition, the samples are treated as follows. To remove any highly volatile residual solvents, the C_{60} sample is first heated to

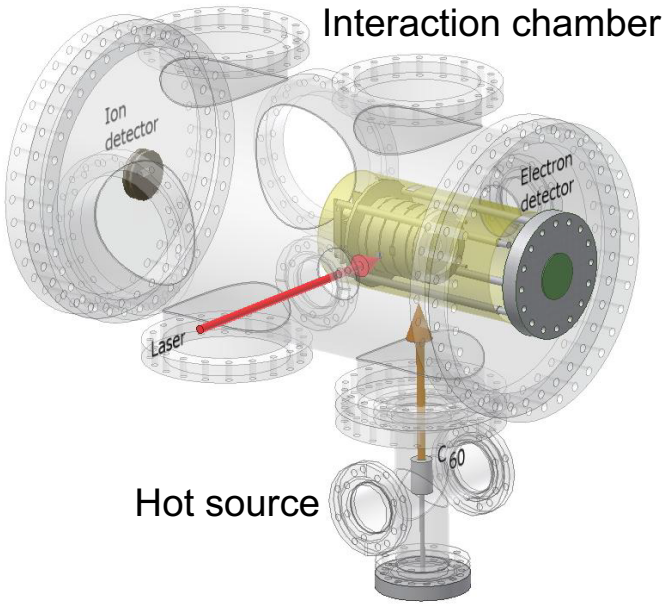

FIGURE 2.13: Schematic diagram of the vacuum chamber. Brown arrow corresponds to the vertically propagating molecular beam. Red arrow corresponds to the horizontally propagating laser beam. The yellow shaded area corresponds to the μ-metal that encapsulates the ion optics. Figure adapted from[59]

373-393 K for 12 hours. After that period, it is heated slowly up to a temperature of 823 K (corresponding vapour pressure $\approx 7\times10^{-4}$ Torr).[60] Measurements were performed from a temperature of 623 K (corresponding vapour pressure $\approx 2\times10^{-6}$ Torr), where a dense enough molecular beam was generated to allow detection of mass and photoelectron spectra.[60] The $[Li@C_{60}]^+[PF_6]^-$ sample is first heated to 373-423 K for 2 days to remove the $[PF_6]^-$ counter ions and any highly volatile residual solvents. Then, in order to limit decomposition and removal of the endohedral atom, it is carefully and slowly heated up to 623 K.

The laser beam propagates towards the chamber (shown by the red arrow in Figure 2.13) and interacts perpendicularly, inside the interaction chamber, with

the molecular beam. It should be noted that the laser beam propagation is parallel to the planes of the two detectors at either side of the interaction chamber. The point of interaction is at the centre of the ion optics assembly. The assembly is surrounded by a cylindrical μ-metal shield where the appropriate holes have been made to allow the propagation of both the laser and molecular beams. This is used in order to screen off any unwanted magnetic fields that could influence the electron trajectories. The laser beam is focused at the centre of the extraction electrodes HV_1 and HV_2, seen as the red dot in Figure 2.14. By manipulating the extraction fields, the two photoproducts can be selectively detected. It should be pointed out that simultaneous detections of both the cations and electrons is not possible with the current setup.

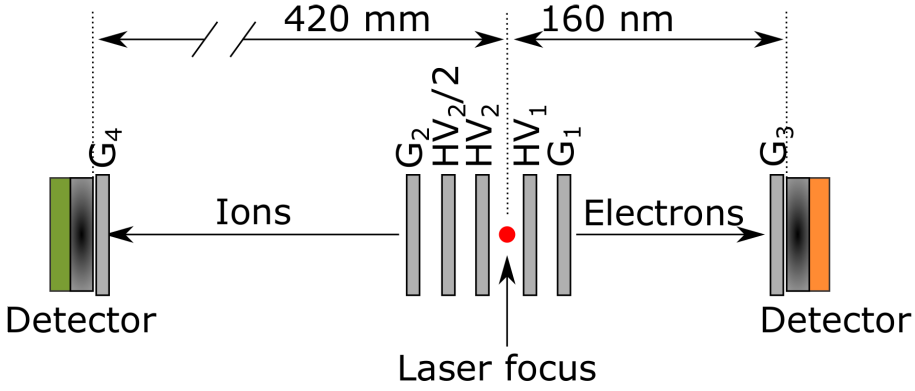

FIGURE 2.14: Schematic diagram of the ion optics assembly and the two detectors. Extraction electrodes: HV_1, HV_2 and $HV_2/2$. Ground electrodes: G_1, G_2, G_3 and G_4. Right hand side: VMI detector. Left hand side: TOF-MS detector.

An oven shutter was fitted to the chamber to allow for a better way to subtract the background signal. As will be explained in Section 2.4.3, before this addition a typical VMI data acquisition consists of two measurements. One where the laser beam interacts with the molecular beam (signal measurement) and

one where the laser beam is blocked (background measurement). The latter was then subtracted from the former to generate the pure sample VMI signal. This was done in order to ensure that any contribution from low background noises will be omitted. With this method however, signal from any contamination within the vacuum environment will not be properly subtracted. As a result, a custom oven shutter was built. The shutter consists of a zero-length reducing flange (DN160CF to DN63CF) where a hole has been bored from the side of the flange to the inner flange side. A metal tube was fitted through the hole and welded on the inner side to ensure that the vacuum was not broken. The other end of the tube was then welded on a blank flange (DN16CF). A hole with a smaller diameter than the inner diameter of the tube was bored through the smaller blank flange and a rotary feedthrough was installed. In order to increase the length of the rotary feedthrough, an extension arm was fitted to it. This consisted of a stainless steel rod that was fixed in place, on the rotary feedthrough, with a grub screw. An "L" shaped bracket was attached at the end of the arm. Therefore by rotating the assembly, the molecular beam was either let through or block off. This custom flange can be seen in Figure 2.15. The oven shutter assembly replaced an identical zero-length reducing flange that was used before to connect the hot source to the interaction chamber.

2.3 Mass Spectroscopy

For the detection of the cations, a linear time-of-flight mass spectrometer (TOF-MS) with a Wiley-McLaren arrangement was used.[61] A schematic diagram of

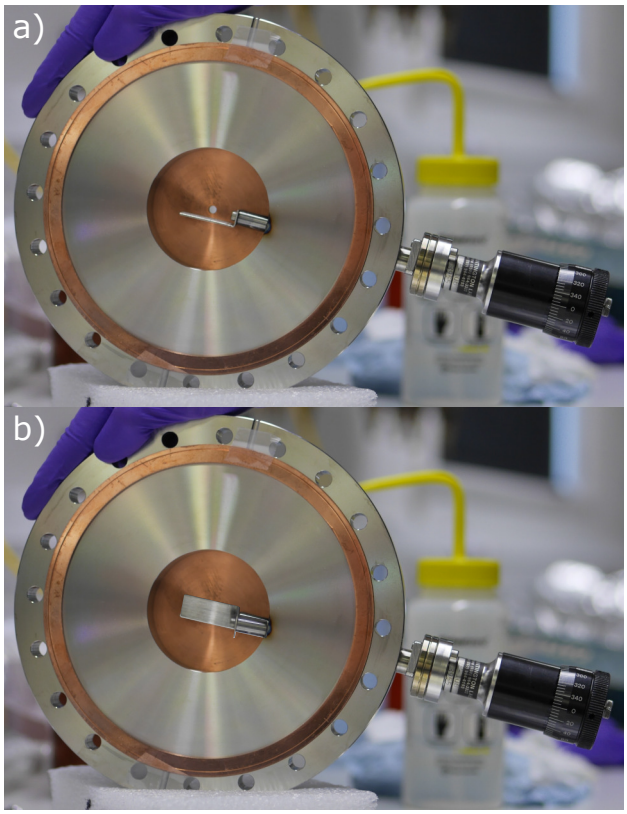

FIGURE 2.15: Photographs of the custom made oven shutter. In (a) the molecular beam is let through, whereas in (b) it is blocked.

the ion optics and TOF-MS setup can be seen in Figure 2.16. In order to highlight the advantage of using such an arrangement of ion optics, the working principle behind a standard TOF-MS will now be described. Ions of mass m and charge z created from the photoionisation event are extracted by a constant electric field, U, which is created from the repeller electrode (HV_1), towards the direction of a field-free region whose length, d, is known. The field-free region is created by grounding the electric field using two electrodes (G_2 and G_4) and allows the ions to propagate with no further acceleration. As such, the potential energy, E_P, gained by the ions from the extraction region is converted in the field-free region into kinetic energy, E_K, such as,

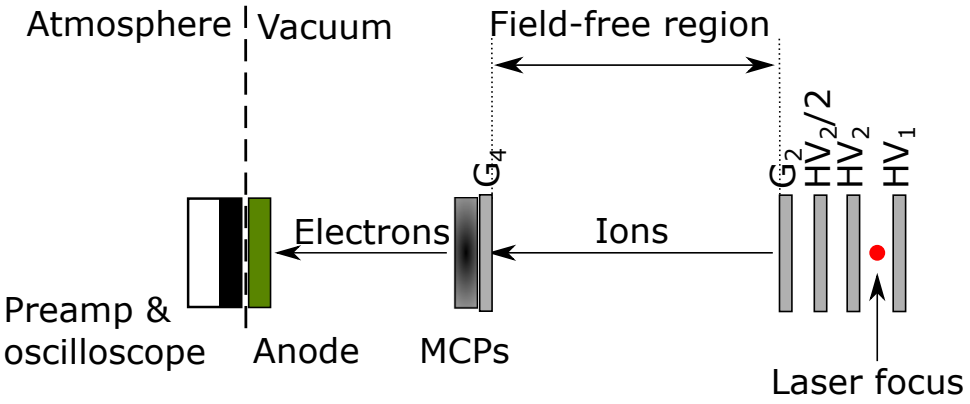

FIGURE 2.16: Schematic diagram of the TOF-MS ion optics, using the Wiley-McLaren extraction scheme, and the ion detector.

$$zU = E_P = E_K = \frac{1}{2}mv^2, \tag{2.9}$$

$$\frac{m}{z} = \frac{2U}{v^2} = \frac{2Ut^2}{d^2}, \tag{2.10}$$

where time, $t = d/v$, is proportional to the mass-to-charge (*m/z*) ratios by,

$$t = d\sqrt{\frac{m}{2zU}}. \tag{2.11}$$

From the above equations, it can be concluded that ions created at the same time and point in space and with the same *m/z*, will end up with identical final velocities and thus will reach the detector simultaneously.

The above is true only for ions which are produced at a point source. However, as was shown earlier, the focus of the laser beam has a specific size and thus

ions will be created over a certain spatial spread. The Wiley-McLaren arrangement was thus used to overcome this spatial spread and temporally focus the ions with respect to their *m/z*. This is achieved by adding a third electrode, the extractor (HV_2), between the repeller and the ground, which has a lower electric potential than the repeller. Ions created further away from the field-free region will gain a higher energy and will thus enter the field-free region with a larger velocity than the ones created closer to it. By carefully adjusting the electric field ratio of the repeller and extractor electrodes, ions of the same *m/z* will reach the detector simultaneously, irrespectively of the point in space that they were initially created. An additional electrode ($HV_2/2$) was introduced to achieve a more uniform potential drop between the extractor and ground electrodes.Typical extraction voltages used in the experiments are HV_1 = +1750 V and HV_2 = +780 V. The voltage optimisation was carried out by varying the values of HV_2 while keeping HV_1 constant and monitoring the resolution of the recorded mass spectrum.

A commercial microchannel plate (MCP) detector (Jordan TOF products Inc., part no. C-0701) housing a pair of Chevron-style MCPs (Photonics USA, part no. MCP 18/12/5 D 40:1 (PS30220)) was used in the TOF-MS setup. This consists of 2 MCPs sandwiched between 3 electrodes. Using a voltage divider, the applied voltage to the detector is such that across a single MCP the voltage is kept less than 1 kV. As each ion hits the detector, an electron cascade is produced within the MCP and is accelerated towards an anode. The anode, within the vacuum side, produces a current from the electron cascade and the signal is directed to a preamplifier (TA1800, FAST ComTec), which amplifies the signal by 10 times, followed by a digital 500 MHz oscilloscope (Agilent Technologies,

MS06054A) on the atmosphere side. The oscilloscope is triggered from the fast photodiode signal inside the Regen. It is connected via a USB cable to a computer where a LabVIEW program controls the settings of the oscilloscope and the accumulation of spectra. The recorded mass spectra provide the ion intensity as a function of arrival time which can later be converted into m/z by calibrating the scale with known mass peaks; for instance with the C_{60}^{+}/C_{60}^{2+} peaks or with the xenon isotope distribution (Figure 2.17).

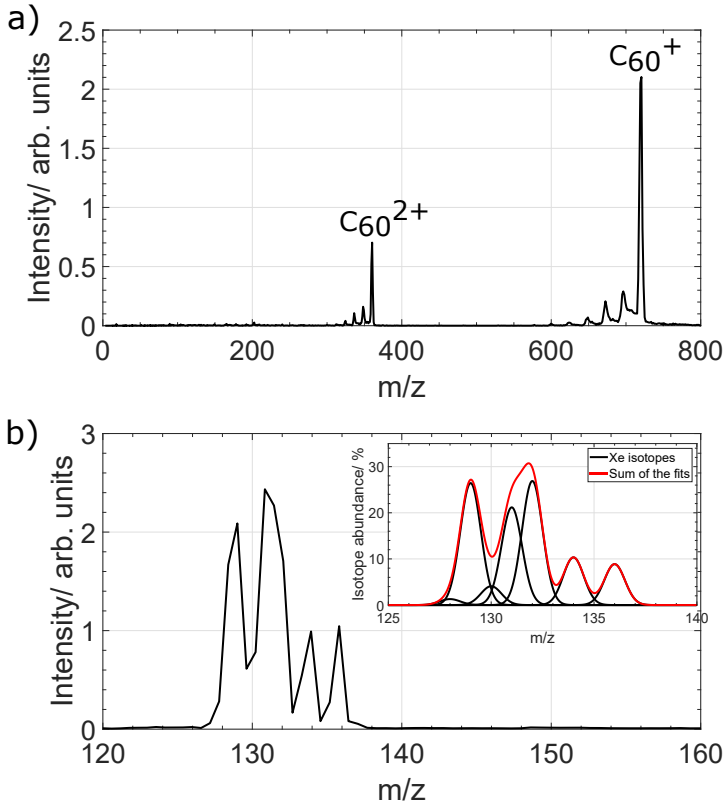

FIGURE 2.17: Spectra used to calibrate the mass spectrometer. (a) C_{60} mass spectrum showing the singly and doubly charged species of the parent ion. (b) Xe mass spectrum showing the singly charged isotropic distribution. The inlet shows the abundance of the Xe isotopes where the individual peaks have been fitted with Gaussian curves (black) and the sum of the fits is plotted in red. Both spectra were acquired using 267 nm, 120 fs pulses.

2.4 Photoelectron spectroscopy

2.4.1 Velocity map imaging

Many challenges in molecular dynamics require that a particle's speed and angular direction be recorded simultaneously. Let us consider the simplified example for photoionisation where a molecule, A, interacts with a photon of

energy, $h\nu$ to form the photoexcited complex A^*. Upon photoionisation, an electron, e^-, is ejected from the photoexcited complex leaving a cation, A^+,[62]

$$A + h\nu \rightarrow A^* \rightarrow A^+ + e^- + TKER. \tag{2.12}$$

The total kinetic energy release (TKER) describes the excess energy which is left after the internal energies of the two products are subtracted. From the laws of energy and momentum conservation, TKER will be shared amongst the cation and the electron according to the following relations,

$$\begin{aligned} (i)\, E_{KIN}(A^+) &= (M_{e^-}/M_A) \times TKER \\ (ii)\, E_{KIN}(e^-) &= (M_{A^+}/M_A) \times TKER, \end{aligned} \tag{2.13}$$

where the fractions in the brackets are called the mass partitioning factors. Given that the mass of the electron is much smaller than the cation, it essentially gains all of the TKER. Each photoionisation event thus yields two fragments, one of which can be considered static. By repeating identical events, the photoelectrons build up a distribution that is spherical in the velocity space. This distribution is called the newton sphere and it is schematically shown in Figure 2.18.[62]

In Velocity Map Imaging (VMI), the expanding in time newton sphere is extracted with the help of ion optics onto a position sensitive detector.[62] The 3-D distribution of the ejected electrons is projected and recorded on a 2-D plane. With the use of some mathematical transformations, details of which will be

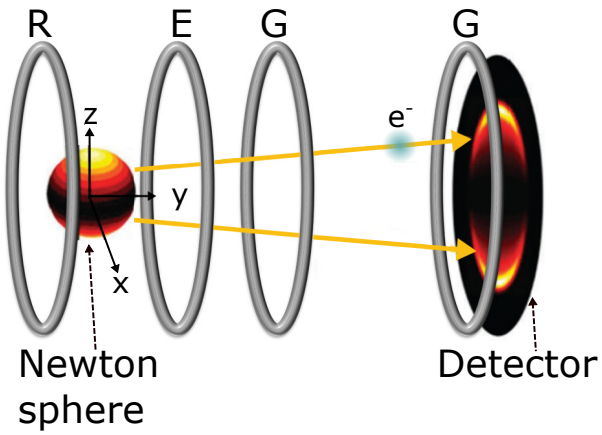

FIGURE 2.18: Schematic diagram showing the VMI ion optics and the projection of the newton sphere on the 2-D detector. Electrodes: R = repeller, E = extractor and G = ground. Figure adapted from Johansson *et al*.[17]

explained in the following paragraphs, the original 3-D distribution can be recovered from the 2-D image.[63]

The ion optics are composed of a set of extraction electrodes, the repeller (R) and extractor (E), that act as an electrostatic lens which accelerates the electrons onto the position sensitive detector (a combination of an MCP assembly and a phosphor screen).[62] A set of ground electrodes are added between the extractor electrode and the detector which create a field-free region, allowing the photoelectrons to expand, unaffected, in space. The above ion optics configuration enables one to correlate the detected position of the photoelectron on the screen, to the original direction and magnitude of its momentum.[62,63] In order to achieve space focusing, where photoelectrons with identical initial momentum that have been created at different parts of the extraction region appear at equal distances from the centre of the image, no mesh grids are used over the extractor and ground electrodes while a mesh grid is used on the

ground electrode right before the detector.[64]

As was previously mentioned, a mathematical algorithm is used on the recorded 2-D image in order to extract the original 3-D distribution of the photoelectrons.[63,65] Lets assume that in Cartesian space, the point of interaction of the light source (a linearly polarised laser pulse) with the molecular beam is the origin of the axes shown in Figure 2.19. Let the the laser beam propagation be along the *x*-axis; the laser polarisation vector be along the *z*-axis; and the detector plane be perpendicular to the *y*-axis. Due to using a linear polarised light source, from the optical selection rules, a directionality is introduced experimentally that results in a cylindrically symmetric velocity distribution of the photoelectrons along the *z*-axis. Taking into account the above, the recorded electron distribution on the detector is,

$$p(x,z) = \int_{-\infty}^{+\infty} s(x,y,z)\,\mathrm{d}y, \tag{2.14}$$

where $s(x,y,z)$ represents the 3-D distribution of the photoelectrons. By taking a slice across the 3-D distribution which is perpendicular to the axis of symmetry (a row along the *x*-axis for $z = z_0$),

$$f(x) = p(x,z_0) = \int_{-\infty}^{+\infty} s(x,y)\,\mathrm{d}y = 2\int_{0}^{+\infty} s(x,y)\,\mathrm{d}y, \tag{2.15}$$

since from the cylindrical symmetry the following is true,

$$\int_{-\infty}^{0} s(x,y)\,\mathrm{d}y = \int_{0}^{+\infty} s(x,y)\,\mathrm{d}y. \tag{2.16}$$

From expressing Equation 2.15 in polar coordinates, by substituting $r^2 = x^2 + y^2$, the Abel transform of $s(r)$ is derived,

$$f(x) = 2\int_{x}^{+\infty} \frac{rs(r)}{\sqrt{r^2 - x^2}}\,\mathrm{d}r, \tag{2.17}$$

The inverse Abel function is derived by applying the Fourier transform theorem on the above equation,

$$s(r) = \frac{1}{\pi}\int_{r}^{+\infty} \frac{\mathrm{d}f/\mathrm{d}x}{\sqrt{x^2 - r^2}}\,\mathrm{d}x. \tag{2.18}$$

The initial electron distribution, $s(r)$, can now be recovered from the measured $f(x)$. However solving the inverse Abel transform is time consuming and alternative reconstruction methods are used instead. A brief description of the method used in this work will be described in Chapter 2.4.3.

2.4.2 Photoelectron Angular Distribution

When using linear polarised light, the ejected photoelectrons have a characteristic distribution in the directionality of their velocities. These distributions are generally anisotropic and are known as photoelectron angular distributions (PADs). PADs offer information on the molecular orbitals and ionisation dynamics which is complimentary to the angle-integrated photoelectron spectra

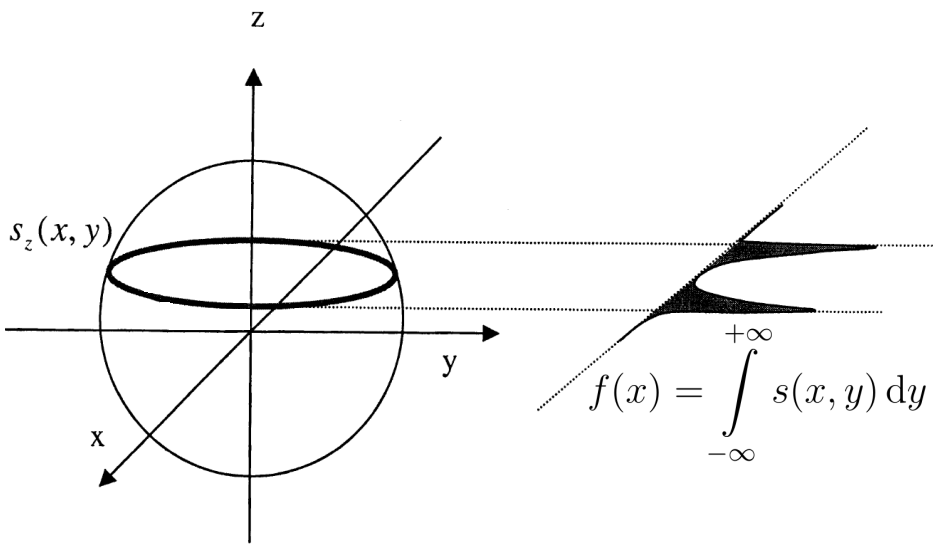

FIGURE 2.19: Representation of a cylindrically symmetric distribution. The projection of a slice across the axis of symmetry $z = z_0$ for a given row of x on the detector results in the distribution's Abel transform, plotted on the right hand side. Figure adapted from Whitaker.[63]

(AI-PES).[66] The wavefunction of an outgoing photoelectron can be expressed as a superposition of spherical harmonic functions ($Y_{lm}(\theta, \phi)$, known as partial waves) and takes the general form,

$$\psi_e = \sum_{lm} c_{lm} e^{i\delta_l} Y_{lm}(\theta, \phi), \tag{2.19}$$

where c_{lm} is a coefficient which contains the angular and radial information of the state that the electron was scattered from and δ_l is the phase shift induced from the scattering. m and l are the laboratory frame projection and orbital angular momentum quantum numbers respectively.[67] The square of this wavefunction results in the intensity of the PAD,

$$I(\theta,\phi) \propto \psi_e^* \psi_e = \sum_{L=0}^{L_{max}} \sum_{M=-L}^{L} B_{LM} Y_{lm}(\theta,\phi), \tag{2.20}$$

where B_{LM} is a coefficient which contains information about the contribution of each individual partial wave and the interference that it has with every other partial wave.[67] It is dependent upon the experimental geometry, the sample spatial distribution, the photoionisation energy and dynamics, and the orbital that the electron was ejected from. The quantum numbers L and M result from the angular momenta vector combination of the two wavefunctions and follow the relations: $|l - l'| \leq L \leq l + l'$ and $M = m + m'$. B_{00}, the first coefficient of the expansion, is proportional to the intensity of the angle-integrated photoelectrum spectrum.[67]

For a randomly oriented sample, as is the case in gas-phase experiments, the PAD following a single photon ionisation using linearly polarised light is given by,

$$I(\theta) = \frac{\sigma_{total}}{4\pi}(1 + \beta_2 P_2(\cos\theta)), \tag{2.21}$$

where σ_{total} corresponds to the angle-integrated cross-section, β_2 to the anisotropy parameter (values from $-1 \leq \beta \leq 2$) and P_2 to the second order Legendre polynomial ($P_2 = \frac{1}{2}(3 \times cos^2\theta - 1)$).[68] The angular distribution is cylindrically symmetric along the polarisation vector and hence it depends only on the angle θ which is the angle between the polarisation vector and the electron's ejection direction.[68]

In atomic systems, when the ejected electron comes from an orbital whose l is

a good quantum number, the photoelectron wavefunction is made up from the interference of only two partial waves, having orbital angular momenta equal to $l-1$ and $l+1$. For molecular systems, L can no longer be considered a good quantum number which results in the photoelectron wavefunction to be expressed by more than two partial waves.[67] However, in the case of fullerene C_{60}, due to the molecule's highly symmetric and hollow structure, an atomic like approach is implemented and L is considered to be a good quantum number. In this case it holds that,

$$\beta_2 = \frac{L(L+1)R_{L-1}^2 + (L+1)(L+2)R_{L-1}^2 - 6L(L+1)R_{L+1}R_{L-1}\cos(\delta_{L+1} - \delta_{L-1})}{(2L+1)(LR_{L-1}^2 + (L+1)R_{L+1}^2)}, \tag{2.22}$$

where $R_{L\pm1} = \int \psi_f^{L\pm1}(r)\,\psi_i^L(r)\,r^3\,dr$ describes the radial dipole matrix elements of the final, f, and initial, i, states and the orbital angular momentum quantum number L corresponds to the one from the initial state.[68,69] Hence, if the initial state has an s character (l = 0), due to the selection rules the outgoing wave will consist of only one partial wave, a p-wave with β_2 = 2. Similarly, if the initial state has a higher orbital angular momentum than 0, the outgoing wave will consist of the interference of two partial waves where the β_2 value will vary with respect to the electron's kinetic energy as a result of the phase shift between the two partial waves.[70] Therefore by comparing the measured β_2 as a function of using different excitation energies with the calculated ones, one can recover the symmetry properties of the states that the electrons have been ionised from and thus be able to assign the character of the SAMO peaks in the photoelectron spectra.[27,35,40,51,52] An example of a PAD analysis for the

SAMOs in C_{60} is provided in the next section.

2.4.3 VMI spectrometer

A VMI spectrometer projects charged species onto a position sensitive detector where the velocity and angular distributions can be simultaneously recorded. The photoionisation events occur between a set of extraction electrodes, namely the repeller (HV_2) and the extractor (HV_1), which act as an electrostatic lens that directs the photoelectrons towards the field-free region (space between ground electrodes G_1 and G_3). Within the field-free region, the photoelectrons are allowed to freely expand in space before reaching the position sensitive detector. The ratio of the voltages of the two extraction electrodes is carefully calibrated to ensure that photoelectrons created at different parts of the newton sphere, which have the same kinetic energy, will appear at equal distances away from the centre of the image on the detector. In order to achieve this space focusing, no mesh grids were used in electrodes HV_1 and G_1. A diagram of the VMI ion optics and detector is presented in Figure 2.20.

To record an image of the photoelectrons, a commercial detector assembly (Photonics USA Inc., part no. 31376) made up of a pair of Chevron-style MCPs and a phosphor screen coupled with fiber optics is used. To ensure that a true field-free region exists in front of the detector, an additional ground electrode was added (electrode G_3). Typical voltages that are applied across the electrodes in the detector are +1700 V for the MCP and +4700 V for the phosphor screen. As a photoelectron impinges on the pores of the MCPs, a cascade of electrons is created within the plates that amplifies the signal. As the electron signal collides with a point on the phosphor screen, fluorescence occurs. The

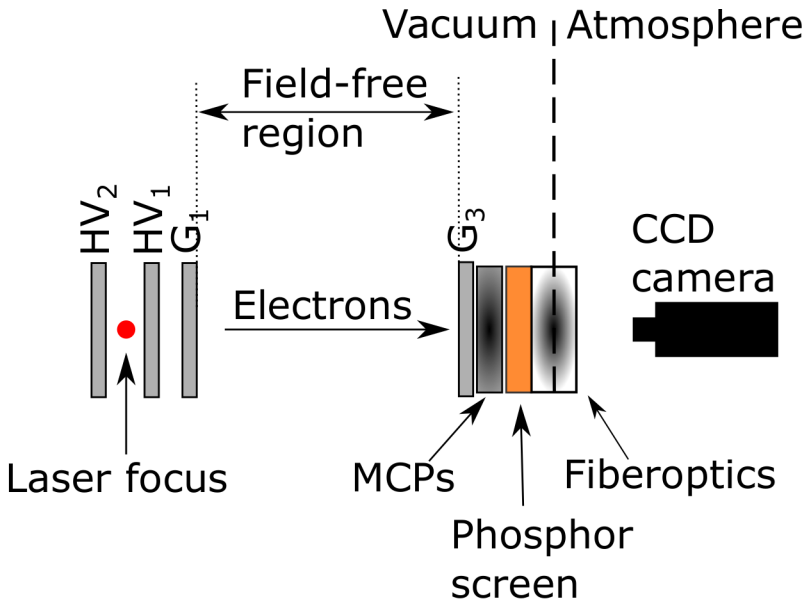

FIGURE 2.20: Schematic diagram of the VMI ion optics and the electron detector.

photons from the fluorescence travel through the fiber optics and are recorded at the atmospheric side of the detector with a CCD camera (Allied Vision Technology, Stingray), which in turn is connected to a computer through a FireWire cable. The camera has a resolution of 1388 x 1038 pixels, a maximum transfer rate of 15 frames per second and a maximum shutter speed of 82 ms. When using a 1 kHz laser, this translates to 82 laser shots per recorded image. Two different image acquisition protocols are used in this thesis and both were written in LabVIEW by Dr Olof J. Johansson.[59] In the continuous acquisition protocol, images get added up over thousands of laser shots, typically around 100k, which make up one data collection. In this protocol two sets of equal in duration data collections are recorded, one consisting of the sample and one of the background measurement. The background measurement is then subtracted from the sample measurement to reveal the true sample image. Initially the

background measurements were recorded by blocking the laser beam from the chamber, whereas after the oven shutter was built, the background measurements were recorded by blocking the molecular beam while the laser beam was let through. On average 10^7 ionisation events are present in an image that makes use of this protocol. When however a much smaller count of ionisation events is present in a measurement, usually this is the case when using low laser power, the single count acquisition protocol is used. With this protocol the user is able to define a threshold for each image so that only true ionisation events are recorded while the rest of the pixel count is set to zero. In addition, the protocol assigns the centre of mass of each recorded spot to a single pixel coordinate, a method known as centroiding which results in obtaining higher resolution images.

Optimising extraction voltages

As mentioned earlier, the resolution of a VMI image, as well as the energy range, depends on the ratio of the extraction electrodes voltages. This ratio can be optimised by ionising Xe and monitoring the structure of the VMI image. The goal is to obtain a VMI image with the narrowest possible rings. By varying only one of the extraction voltages, the extractor electrode, a set of images is recorded. After inverting the images, the velocity distributions can be obtained in terms of camera pixels. An example measurement series is shown in Figure 2.21 where Xe was ionised using 267 nmm 120 fs pulses. (a) shows how the arrival distribution of the Xe $P_{3/2}$ peak changes with the extraction conditions and (b) shows the dependence of the FWHM of the fitted Gaussian peaks on the extractor voltage. For this measurement, the ideal conditions are

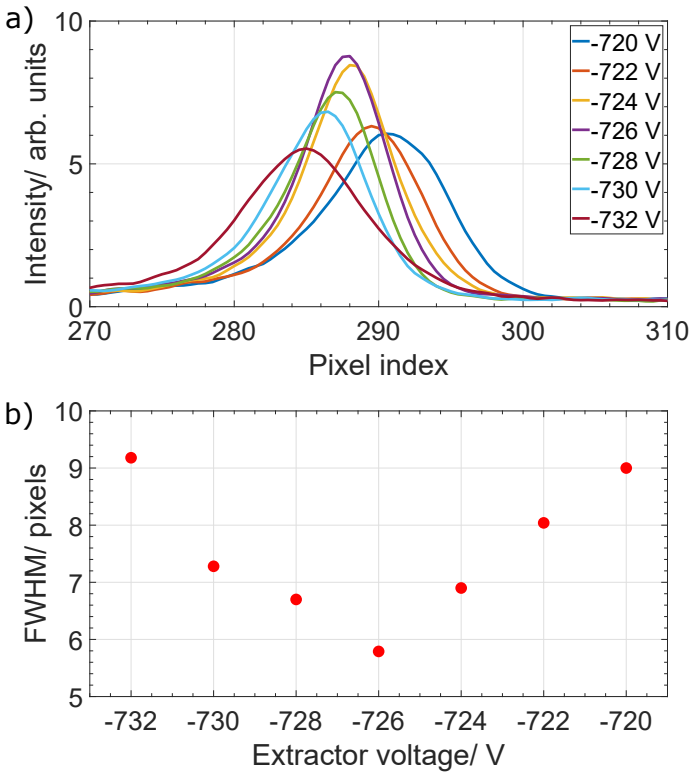

FIGURE 2.21: VMI extraction voltage optimisation using 267 nm 120 fs pulses. The voltage of the repeller electrode was kept constant at -1000 V while the extractor electrode voltage was varied. (a) shows the $P_{3/2}$ peak in pixel scale and (b) shows the FWHM from fitting a Gaussian curve on the peaks in (a).

met with extractor voltage = -726 V and repeller voltage = -1000 V.

Inversion method

The raw VMI images must be deconvoluted in order to recover the velocity and momentum distributions of the ejected photoelectrons. The images collected on the detector correspond to a 3-D object that has been projected onto a 2-D screen. The image reconstruction method that was used is based on the polar onion-peeling algorithm which has been modified to include Legendre

polynomials up to n = 10.[71–73] The program was developed by Dr Gordon G. Henderson and was named gPOP. In order to ensure that the extracted distributions using gPOP are real and not artefacts of the program, the results are always compared using a widely known alternative inversion method, BASEX.[74]

Using gPOP, the raw images are initially converted from Cartesian, $K(x, z)$, into polar space, $h(r, \theta)$. The centre of the raw image, $r = 0$, and the maximum radius, $r = r_{max}$, are set (beyond which no events are taken into consideration). The intensity of the measured 2-D distribution is fitted to the angular distribution,

$$I(\theta) = N(r) \sum_{n} \beta_n(r) P_n[cos(\theta)], \tag{2.23}$$

where $N(r)$ is an intensity factor, $\beta_n(r)$ is the anisotropy parameter and $P_n[cos(\theta)]$ is the nth order Legendre polynomial. As such, the experimentally observed $N(r)$ and $\beta_n(r)$ can be determined. For a certain radius r, basis functions, that are produced by integrating perfectly isotropic images, are used to create a polar image, $h_{ideal}(r, \theta)$. Using $N(r)$ and $\beta_n(r)$ in conjunction with this image, an idealised image can be generated from,

$$h_{fit}(r, \theta) = h_{ideal}(r, \theta) N(r) \sum_{n} \beta_n(r) P_n[\frac{r}{r_{max}} cos(\theta)], \tag{2.24}$$

where $\frac{r}{r_{max}}$ compares the amount of polar pixels found at radius r with that found at radius r_{max}. $h_{fit}(r, \theta)$ thus represents the ϕ-contribution responsible for the electrons found at radius r. Starting from $r = r_{max}$ and incrementally

decreasing to $r = 0$, $h_{fit}(r, \theta)$ is subtracted from the raw image $h(r, \theta)$, resulting in the inverted image.

VMI energy calibration

The velocity distributions extracted from the inverted raw images are presented as a function of camera pixels[2]. In order to convert the distributions into a kinetic energy scale, spectra of published structures need to be reproduced so that a calibration factor can be calculated. Each calibration factor is unique to the detector geometry and experimental conditions - wavelength, lens and extraction voltages. For the studies presented here, the well documented energy level structure of Xe is used.[75–77]

Xe has two well characterised ionisation potentials (IP): $Xe(^1S_0) \rightarrow Xe^+(^2P_{3/2})$ IP = 12.13 eV and $Xe(^1S_0) \rightarrow Xe^+(^2P_{1/2})$ IP = 13.437 eV. With the photon energies used in this study, multiple photons are required to access these states. Therefore depending on the intensity and wavelength, either the peak difference between the ionisation to the ground state $^2P_{3/2}$ and the first ATI peak or the ionisation to the ground state $^2P_{3/2}$ and the first excited spin-orbit state $^2P_{1/2}$ is used to calibrate the spectra. In the first case, the difference is equal to the photon energy while in the latter it is 1.307 eV. Examples of the two different methods of calibrating the energy scale are shown in Figures 2.22 and 2.23.

In Figure 2.22, Xe is ionised with 800 nm, 120 fs pulses. The leftmost peak in (c) and (d) is a result of an 8-photon (12.40 eV) non-resonant ionisation from the ground state. Due to the high intensity that was used, additional photons were coherently absorbed at the $^2P_{3/2}$ state and ATI peaks are visible.

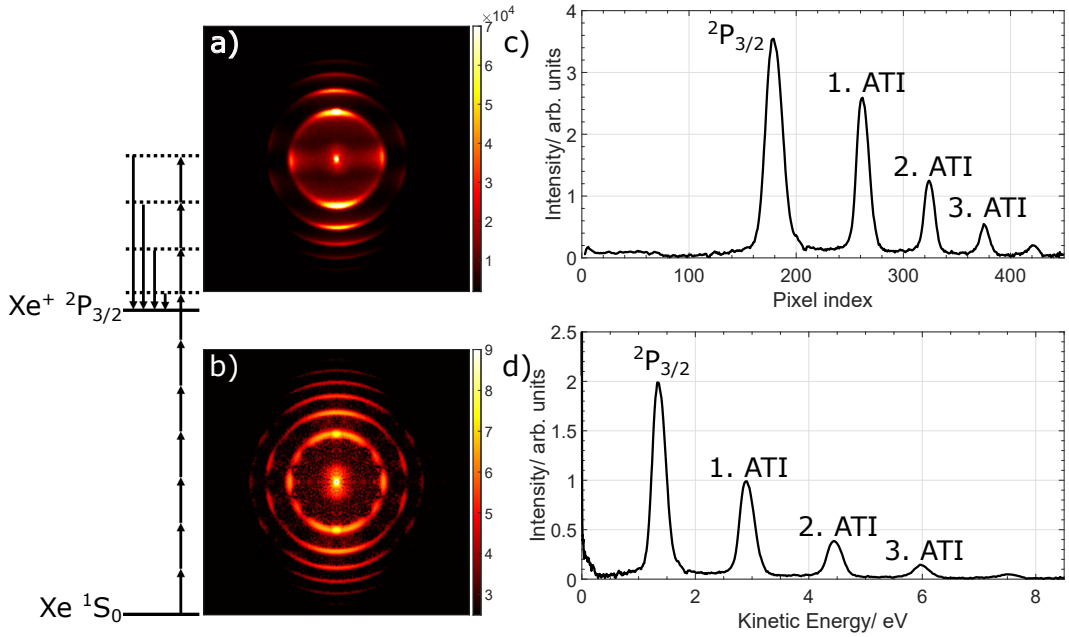

FIGURE 2.22: (a) and (b) show respectively the raw and inverted VMI images when Xe was ionised with 800 nm, 120 fs pulses. (c) and (d) show respectively the velocity distribution in pixel and kinetic energy scales. Energy diagram on the left depicts the ionisation mechanism.

In Figure 2.23, Xe is ionised with 267 nm, 120 fs pulses. In this 3-photon (13.93 eV) non-resonant ionisation the $^2P_{3/2}$ and $^2P_{1/2}$ are accessed.

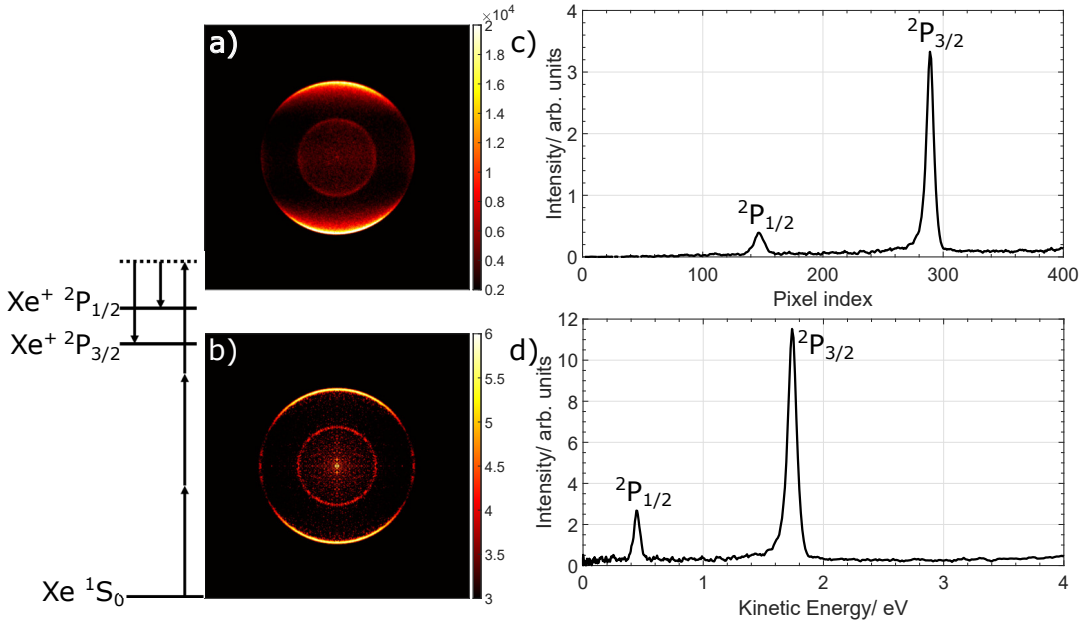

FIGURE 2.23: (a) and (b) show respectively the raw and inverted VMI images when Xe was ionised with 267 nm, 120 fs pulses. (c) and (d) show respectively the velocity distribution in pixel and kinetic energy scales. Energy diagram on the left depicts the ionisation mechanism.

Analysing PADs

To deconvolute the photoelectron angular distribution from an inverted image, the VMI image is centrosymmetrically divided into 10° intervals and the angular-resolved PES (AR-PES) is calculated by integrating the signal on each interval. Figure 2.24 shows the above for the 0-10°, 40-50° and 80-90° angular segments of a C_{60} inverted VMI image.[17] As can be seen from the figure, and from previous studies where C_{60} has been subjected to fs-ps excitation, the distribution of the PES is described as a peak structure that is superimposed on an exponentially decreasing thermal electron background.[17,51] After the thermal electron background is subtracted from the PES, the resulting signal is fitted

manually with Lorentzian peaks. The experimentally determined β vales for each specific kinetic energy peak can be obtained by fitting Equation 2.21 on a plot that compares the area of the peak with respect to the polar angle of the angular segment of the AR-PES. This procedure is repeated using different excitation wavelengths. An example of such a measurement series is shown in Figure 2.25 where each individual point corresponds to the β value of a specific peak taken using different excitation wavelengths. TD-DFT calculations of the β value (solid lines in Figure 2.25) are performed for the excited states that are of interest to aid with the peak assignment.

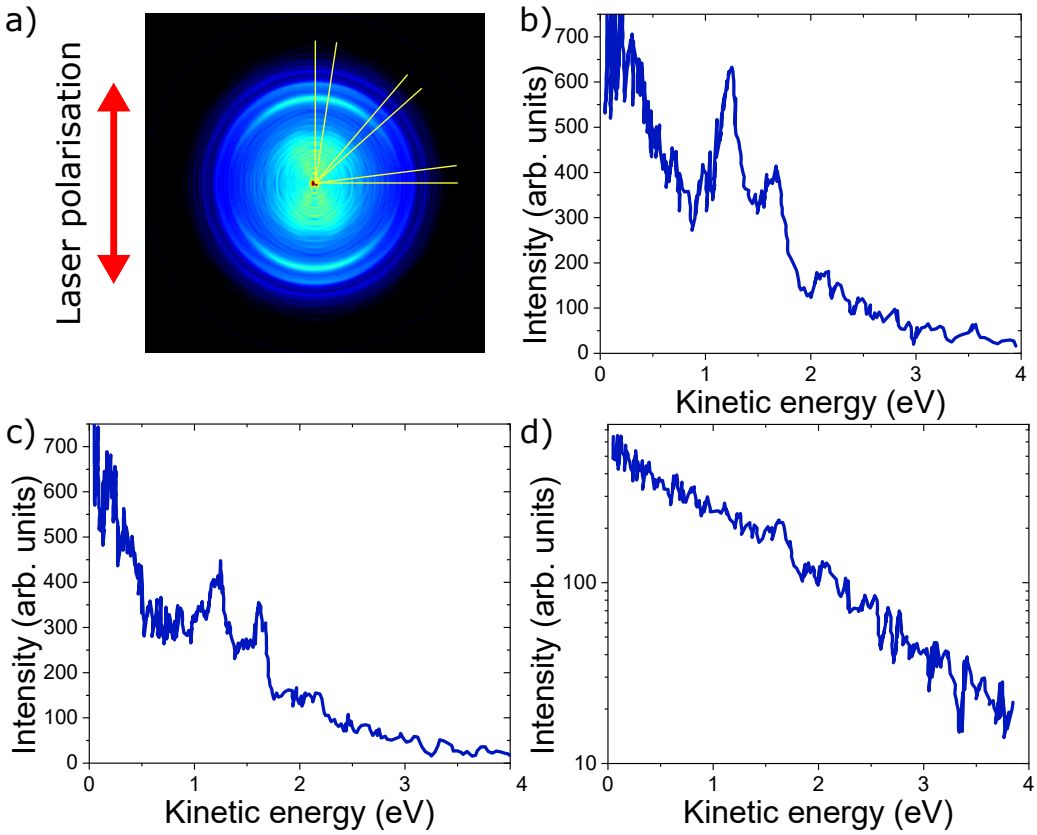

FIGURE 2.24: (a) Inverted VMI image of C_{60} ionised with 400 nm, 120 fs pulses. The image in (a) is divided into three 10° angular segments. The PES shown in (b), (c) and (d) correspond to the 0-10°, 40-50° and 80-90° angular segments respectively. (d) is plotted in a semi-logarithmic scale to clearly show the exponential nature of the thermal electron background. Figure adapted from Johansson *et al.*[51]

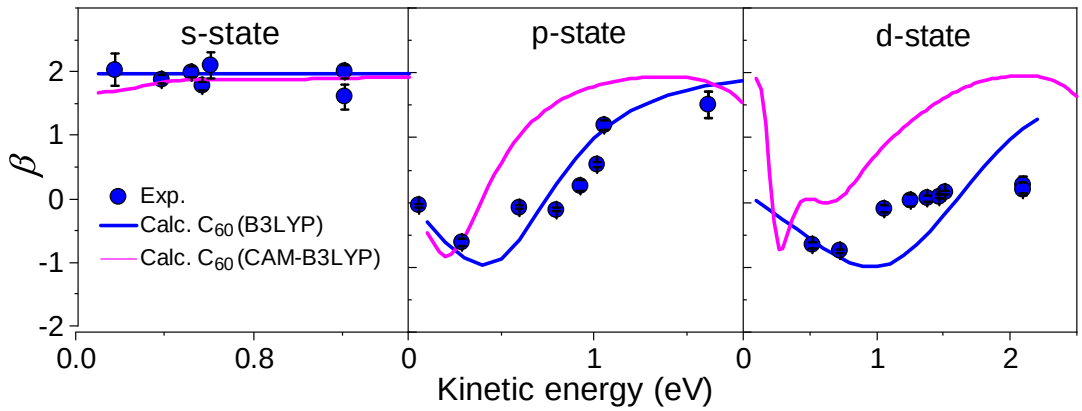

FIGURE 2.25: PADs of the S-, P- and D-SAMOs of C_{60}. Each point corresponds to a measurement taken under different excitation wavelengths. The solid lines correspond to the calculated β-values for C_{60} for a randomly oriented sample. Blue: TD-DFT/B3LYP/6-31+G(D) and purple: TD-DFT/CAM-B3LYP/6-31+G(D). Figure adapted from Johansson *et al.*[51]

2.5 Electronic structure methods

Computational investigations have an increasingly important role within the chemical and physical research. Simulations based on theoretical models have been used to support new findings, analyse experimental results and prove existing or new hypotheses. In this section, a brief description of the electronic structure methods that are later used will be given. All the calculations were performed using the Gaussian 09 software.[78]

2.5.1 Density Functional Theory

The time-independent Schrödinger equation can be written as,

$$\hat{H}\,\Psi = E\,\Psi, \tag{2.25}$$

where $\hat{H}$ is the Hamiltonian operator which acts on the wavefunction, Ψ, to yield the eigenvalues, E, of the system.[79] In molecules, the Hamiltonian operator describes the potential and kinetic energy terms: the kinetic energies of the (i) electrons and (ii) nuclei separately, (iii) the potential energy of the nuclear-nuclear repulsions, (iv) the potential energy of the electron-electron repulsions, and (v) the potential energy of the electron-nuclear attractions. The solutions of the Schrödinger's equation give a full quantum mechanical description of the studied system. However, it is impossible to be solved exactly for systems with more than one electron.

There are several theories that can be used which simplify the complexity of the Schrödinger equation, one of which is the Density Functional Theory (DFT).[80] DFT makes use of the Born-Oppenheimer approximation which separates the electronic and nuclear components of the wavefunction by fixing the position of the nuclei in space due to the large mass difference between the electrons and the nuclei. This transforms the Hamiltonian operator from a five-term to a three-term system given that the kinetic energy of the nuclei is now zero and the nuclear-nuclear repulsions become a constant external field which can be calculated classically from Coulomb's Law.[81] The foundations of DFT lie in the following Hohenberg-Kohn theorems which demonstrate that a unique functional, with which the electron density and ground state energy of a system can be exactly determined, exists.[82] The first theorem shows that the energy of a system can be expressed as a functional of the electron density and the second one shows that the energy of a system has a minimum value when the electron density is identical to the ground state electron density. The latter is also known as the variational principle. The above lead to the Kohn-Sham

equation,

$$\left[-\frac{1}{2}\nabla^2 + V_{ext}(r) + \int \frac{\rho(r')}{|r - r'|}\mathrm{d}r + V_{XC}(r) \right] \phi_i = \varepsilon_i \phi_i \,, \tag{2.26}$$

where the first term describes the kinetic energy of the electrons, $V_{ext}(r)$ is the attractive Coulomb potential between the electrons and the nuclei, the integral term is the repulsive Coulomb potential between the electron in the orbital of interest ϕ_i and the rest of the electrons in the system and $V_{XC}(r)$ is the exchange correlation potential which describes the remaining electron-electron interactions, namely the electron exchange and electron correlation, and is given by,

$$V_{XC}(r_i) = \frac{\delta E_{XC}[\rho(r)]}{\delta \rho(r)}, \tag{2.27}$$

where E_{XC} is the exchange correlation energy functional and $\rho(r)$ is the electron density.[79,83] Therefore, as $V_{XC}(r)$ is expressed in terms of the density, Equation 2.26 has to be solved self-consistently by using approximations to find $V_{XC}(r)$. A variety of choice for functionals is available to describe the exchange correlation potential and all are different with respect to what approximations have been used. Their choice is dependent upon the nature of the system that is subjected to investigations. Within this thesis, pure DFT generalised gradient approximation (GGA) functionals such as PBE as well as hybrid DFT functionals such as PBE0, B3LYP and CAM-B3LYP were used. In pure DFT functionals, the electron exchange and electron correlation are both approximated. In hybrid DFT functionals, pure DFT functionals are mixed with Hartree-Fock theory to provide a fraction of the exact electron exchange while the electron

correlation is approximated.[79] A summary of the different calculations for C_{60} and Li@C_{60} is presented in Chapter 3.2.3.

The time-independent density can be obtained by summing each occupied single electron Kohl-Sham orbital, $\phi_i(r)$,

$$\rho(r) = \sum_{i=1}^{n} |\phi_i(r)|^2. \tag{2.28}$$

2.5.2 Time-dependent DFT

With time-dependent DFT (TD-DFT), the excited state properties of a system are computed by analysing how the studied system responds to a time-dependent perturbation, for example a time-dependent laser electric field. Thus the time-dependent Schrödinger equation has to be solved,

$$i\hbar \frac{\partial}{\partial t} \Psi(r,t) = \hat{H} \Psi(r,t). \tag{2.29}$$

The foundations of TD-DFT are based on two theorems. The Runge-Gross theorem proves that for a given initial state (with Ψ_0), the time-dependent density of the system, $\rho(r,t)$, can be one-to-one mapped onto the time-dependent external potential.[84] This potential is defined by a purely time-dependent function which results in only the phase of the wavefunction to change while keeping the density of the system the same. Meaning that two densities which have evolved from the same initial state and have been subjected to two different external potentials will always be different.[85] Because of the one-to-one mapping,

the time-dependent wavefunction, $\Psi(r,t)$, is defined up to a time-dependent phase factor, $a(t)$,

$$\Psi(r,t) = e^{-ia(t)}\Psi\left[\rho(t), \Psi_0\right](t). \tag{2.30}$$

The second theorem is analogous to the Hohenberg-Kohn theorems that were described earlier for the time-independent DFT, and supports the variational theory principle. The above theorems lead to the time-dependent Kohn-Sham equation,

$$i\frac{\partial}{\partial t}\phi_j(r,t) = \left[-\frac{1}{2}\nabla^2 + v_{ext}(r,t) + \int \frac{\rho(r',t)}{|r-r'|}\mathrm{d}^3r + v_{XC}(r,t)\right]\phi_j(r,t), \tag{2.31}$$

where $v_{ext}(r,t)$ corresponds to the external time-dependent potential and the last term in the parenthesis corresponds to the exchange-correlation potential. Similar to the time-independent DFT, this potential is approximated using functionals which depend on the electron density of the system.

The time-dependent density can be obtained by summing each occupied time-dependent single electron Kohl-Sham orbital, $\phi_j(r,t)$,

$$\rho(r,t) = \sum_{j=1}^{n} |\phi_j(r,t)|^2. \tag{2.32}$$

Dr Benoit Mignolet and Prof Francoise Remaçle (University of Liège) performed the TD-DFT calculations on C_{60} and Li@C_{60} that are presented in Chapter 3 in

addition to computing the fullerene SAMO Dyson orbitals. Dyson orbitals represent the wavefunction of the ionised electron. They are obtained by overlapping the many-electron wavefunctions of the neutral and cation molecules. Due to the diffuse nature of the SAMO states, the hybrid, long-range corrected DFT functional CAM-B3LYP was implemented for the Dyson orbital calculations.

2.5.3 Basis set

In computational chemistry a basis set is a set of mathematical basis functions that are used to describe the molecular wavefunction of the system. Because the form of the real molecular wavefunction is not known, it is approximated through the linear combination of one-electron basis functions. These basis functions provide information about the size and shape of the atomic orbitals. The relative intensity that each basis function, ϕ_i, has when constructing the molecular wavefunction, Ψ, is described by the weighting coefficient, c_i, such that,

$$\Psi = \sum_i c_i \phi_i. \tag{2.33}$$

By altering the weighting coefficients, different wavefunctions can be constructed for a system. Keeping in line with the variational principle and using a self-consistent loop, the weighting coefficients are changed until the wavefunction can be mapped to the lowest possible energy within any specified constraints.

In the ground state calculations of C_{60} and Li@C_{60}, polarisation and diffuse functions as well as a split-valence basis set were used. These conditions afforded adequate qualitative results to assign the SAMO peaks in the STS spectra. However, because SAMOs are very diffuse states that have electron density located also in the centre of the fullerene cage, in the excited state calculations additional basis functions had to be implemented to correctly describe the SAMO energies and angular distributions. In the hope of reducing the computational expense of adding diffuse functions on each carbon atom, a ghost atom (Bq), an atom with no nuclear charge, was added in the centre of the fullerene cage. Five additional sets of basis functions were implemented on the ghost atom. In this way the electron density both inside and far from the cage was described correctly.

2.6 Scanning Tunnelling Microscopy and Spectroscopy

Scanning Tunneling Microscopy (STM) and Spectroscopy (STS) are experimental techniques which are used in surface science. They both make use of a scanning tunneling microscope apparatus which consists of a sharp metallic tip which is brought very close to a conducting sample. Due to the short distances between the tip and the sample, usually in the order of a few Å, their wavefunctions overlap. Upon the application of a voltage difference between the tip and the sample, V which is also referred to as a bias, electrons tunnel from the tip to the sample and *vice versa*, creating a measurable current.[86] This tunnelling current, I, depends on the overlap of the wavefunctions and for a

small bias it can be approximated by,

$$I \propto \frac{CV}{z} e^{-2\kappa z}, \tag{2.34}$$

where C is a constant, κ is the inverse decay length and z is the distance between the sample and the tip. For a positive bias, electrons tunnel from the conduction band of the tip to the unoccupied electronic states of the sample, while for a negative bias it is the opposite.

In constant-current STM imaging, Figure 2.26 (a), the tip position is scanned across the two dimensions of the sample and a feedback loop is applied using piezoelectric electronics to ensure that the distance between the tip and the sample is kept constant, hence keeping the measured current constant. The resulting information is an electronic topographic map of the sample.[87] Figure 2.26 (b) displays such a map for an island of C_{60} molecules which has been adsorbed on a Au(111) surface.[88] Each distinct feature in the topographic image corresponds to an individual fullerene molecule. The bright and dark areas correspond respectively to protrusions and depressions of the unoccupied electronic states which are found at +0.4 V.

In STS measurements, the tip is fixed in a predefined position and the differential conductance (dI/dV) can be measured using a lock-in technique as a function of the bias while keeping the current constant (feedback loop turned on) or the height constant (feedback loop turned off). The resulting constant-current (c.c.) or constant-height (c.h.) dI/dV spectra represent the electronic local density of states (LDOS) under that tip position.[86,87] Figure 2.26 (c) is a c.h. dI/dV spectrum of a C_{60} molecule from the island in (b).[88]

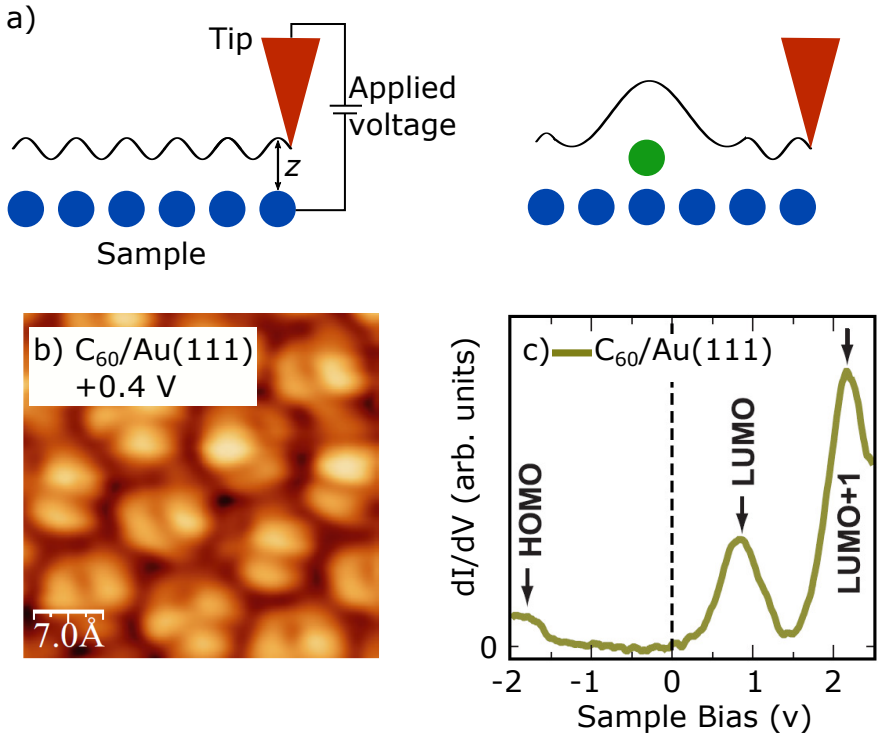

FIGURE 2.26: (a) STM constant-current topography schematic diagram. (b) Constant-current image of an island of C_{60} molecules adsorbed on a Au(111) surface, recorded at +0.4 V. Each distinct feature corresponds to an individual fullerene molecule. (c) Constant-height differential conductance (c.h. dI/dV) spectra of a C_{60} molecule from (b). Figures (b) and (c) adapted from Schulze *et al.*[88]

Henry J. Chandler and Dr Renald Schaub (University of St Andrews) performed the STM and STS measurements on C_{60} and Li@C_{60} as well as the Li switching measurements on Li@C_{60} which are presented in Chapter 3. The experiments were performed under ultra high vacuum (UHV), at near liquid helium temperatures (∼5 K) and using a commercially available STM microscope (CreaTec). Before sample deposition, the Au(111) and Cu(110) surfaces were cleaned with argon sputtering and annealing at 820 K and 770 K respectively. The Cu(110)-(2x1)O surface was produced by depositing molecular oxygen on

the Cu(110) surface. The evaporation conditions for the C_{60} and Li@C_{60} samples were identical to what was described for the gas-phase measurements in Chapter 2.2. For additional details on these experiments, the interested reader is referred to our published work.[89,90]

3 $Li@C_{60}$ Super-Atom Molecular Orbitals

3.1 Introduction

Endohedral fullerenes are a class of fullerene molecules where atoms, ions or molecules are encapsulated inside the fullerene carbon cage. Ever since the discovery of the fullerene C_{60}, endohedral fullerenes have been under investigation regarding their synthesis, their physical and chemical properties and their potential use in applications.[91,92] Endohedral fullerenes containing a metal atom (referred to as endohedral metallofullerenes) are designated by the chemical formula $M@C_{2n}$. They are most commonly produced in macroscopic amounts by using metal-filled graphite rods as electrodes within the arc-discharge method, followed by solvent extraction and HPLC purification of the soot. The above protocol has been successful in purifying endohedral metallofullerenes whose cage is larger than C_{60}, such as $La@C_{82}$, $Y@C_{82}$, $Sc_3N@C_{82}$.[93–96] There has not been much success in extracting $M@C_{60}$ fullerenes that have been produced with the arc-discharge method due to the fact that these molecules are highly reactive with the other fullerenes and carbon materials inside the soot. This behaviour has been partly attributed to the small

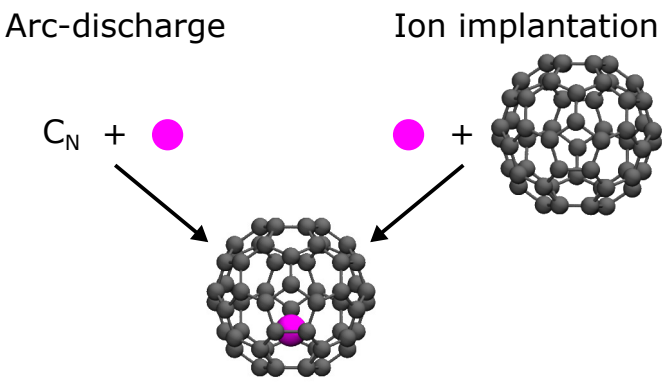

FIGURE 3.1: Methods of endohedral metallofullerene formation. Left hand side, arc-discharge. Right hand side, ion implantation.

HOMO-LUMO band gap of these materials. In addition, many M@C_{60} fullerenes have been shown to have a low solubility in the common fullerene extraction solvents.[97]

Another synthesis method exists where metal ions are implanted into an already formed fullerene cage, Figure 3.1. The ion implantation method was first demonstrated in the production of Li@C_{60}.[98,99] Difficulties existed with purifying and characterising the material due to its tendency to oligomerise in solution and in solid state as well as its tendency to decompose by eliminating the Li atom when exposed to air.[97,100,101] The amount of material that could be prepared by this method was small which hindered the ability of structural characterisation and elemental analysis. A major breakthrough came with the oxidation of Li@C_{60} to Li^+@C_{60}.[102,103] The authors used the plasma implantation method, that is based on principles related to the ion implantation method, to form a mixture of Li@C_{60} and C_{60}, followed by a one-electron reduction to form a monomeric Li@C_{60} cation which was stabilised as a PF_6 or $SbCl_6$ salt. Using this method, commercialised production of the salt has made

characterisation studies feasible.[102–104] From x-ray diffraction measurements of the salt materials, the off-centre position of the Li atom inside the cage which has been proposed from calculations was confirmed, being 1.4-1.5 Å off-centre towards the centre of a six-membered ring.[102,104–108]

Recently, from an ultraviolet and x-ray photoelectron spectroscopy investigation of the $[PF_6]^-$ salt, it was found that the ion counterpart is ejected upon heating, leaving neutral Li@C_{60} molecules.[109] In addition, in the same study it was estimated that the ionisation potential of Li@C_{60} is 1.1 eV smaller than that of C_{60}. This is consistent with previous gas-phase experiments where the ionisation potential of C_{60} was found to be 7.6 eV[110] while that of Li@C_{60} to be 6.5 eV.[111] Moreover, in neutral Li@C_{60} an electron transfer from the Li to the C_{60} cage effectively creates an ion-cation pair.[105,112,113] In the monomeric form, Li@C_{60} is a radical species that shows an increased reactivity with its surroundings, seen from its tendency to oligomerise, react with oxygen and decompose.[112,114–116]

The implantation methods offer an important advantage over the arc-discharge method which is that the cage structure of the resulting endohedral molecule is identical to the empty fullerene cage. With the arc-discharge method the carbon cage grows around the endohedral species. As a result of charge transfer between the endohedral species and the cage during growth, in many cases the most stable cage structure is an isomer that is not the most energetically stable form of the equivalent C_{2n} empty cage. Hence a direct comparison between, for example, Li@C_{60} and C_{60} can be used as a benchmark to investigate the exact influence that the encapsulated atom has on the chemical and physical properties.

In the following chapter, the influence that the encapsulated Li atom has on the electronic structure of the Li@C_{60} molecule will be investigated through a combination of gas-phase photoelectron spectroscopy, DFT and TD-DFT calculations and low-temperature scanning tunnelling microscopy and spectroscopy. Particular interest will be placed on the SAMO excited states and how they might contribute to the switching phenomenon that takes place in surface bound molecules.

From the data presented below, Dr Benoit Mignolet and Prof Francoise Remaçle (University of Liège) performed the TD-DFT calculations and computed the Dyson orbitals of C_{60} and Li@C_{60}. The STM and STS data that are presented were acquired in collaboration with Henry J. Chandler and Dr Renald Schaub (University of St Andrews). An extensive analysis of the STM/STS experimental data will not be provided in this thesis as the majority of that work was done by our collaborators from the University of St Andrews while we contributed to the experimental design and the data interpretation. For more information the interested reader is however directed to our published work[89,90] and to Henry J. Chandler's PhD thesis.[117]

The visualisation of the MOs of C_{60} and Li@C_{60} from the DFT calculations was achieved using the VMD software,[118] while the images were rendered using the Tachyon plugin.[119]

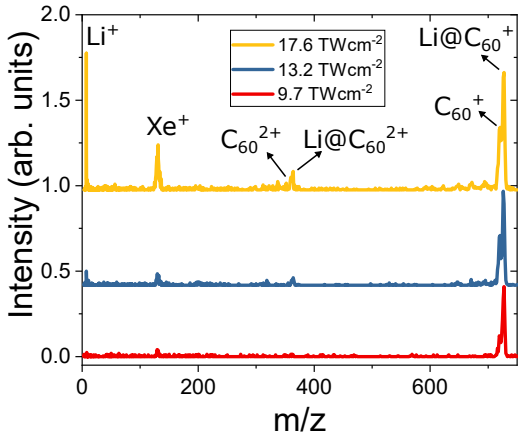

FIGURE 3.2: Li@C_{60} mass spectra obtained using 540 nm, 35 fs for a range of laser intensities. Blue = 17.6 $\pm$ 0.9 TWcm^{-2}. Red = 13.2 $\pm$ 0.9 TWcm^{-2}. Yellow = 9.7 $\pm$ 0.9 TWcm^{-2}. The Xe^+ isotope distribution is visible due to the calibration protocol.

3.2 Results and Discussion

3.2.1 Sample characterisation

The $[Li@C_{60}]^+[PF_6]^-$ salt was heated up to 620 K according to the procedure which was described in Chapter 2.2. Following this procedure, the recorded mass spectra show no signs of PF_6 or any other impurities. When low intensity fs laser pulses are used for photoionisation, signals from both C_{60} and Li@C_{60} ions are detected, Figure 3.2. With an increasing laser intensity a higher relative C_{60}^+ peak intensity was observed, along with doubly-charged prompt ion species, small fullerene cage structures and a signal corresponding to Li^+. The Li^+ peak is detected only after the onset of fragmentation which suggests that a decay channel exists where the endohedral atom is removed and ionised when the fullerene cage starts to fragment.

In a recent ultraviolet and x-ray photoelectron spectroscopy investigation of

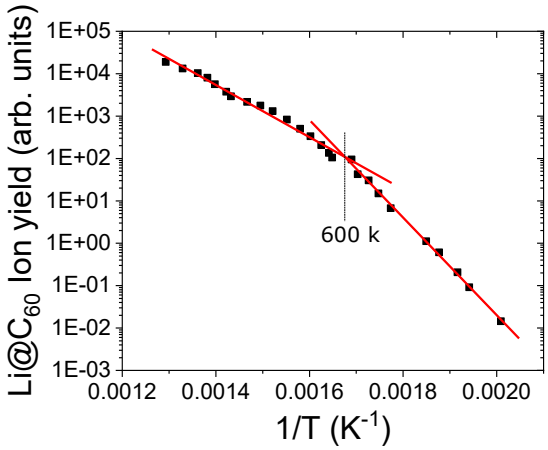

FIGURE 3.3: Li@C_{60} ion yield as a function of the inverse oven temperature recorded with 540 nm, 35 fs laser pulses. The start of thermal decomposition is evident by the change in slope, occurring at 600 K. The red lines are the linear best fit lines for the data before and after the onset of thermal decomposition.

thin films created using the same starting material, sublimation at 623 K resulted in films where neutral Li@C_{60} was present and PF_6 was absent.[109] The authors were not able to confirm whether C_{60} was absent or not in their films. They did however report that increasing the sublimation temperature beyond 823 K diminished the intensity of the UPS signals that were attributed to the endohedral molecule and the overall signal became similar to that of the empty cage, suggesting that the encapsulated atom is ejected at those temperatures. In line with the above, from an oven temperature dependence investigation the starting material decays above 600 K, Figure 3.3. Moreover, it was observed that with the standard heating procedure, subliming at 620 K, the ratio of the endohedral and empty cage parent ion peaks was affected as the material was heated for a longer time. Similar observations were reported in the past from thermal desorption spectroscopy and photoionisation studies of Li@C_{60}.[111,116] Therefore over the course of the photoelectron spectra measurements, mass

Excitation wavelength / nm	267	400	500	540	600
$Li@C_{60}^+$:C_{60}^+ mass peak ratio	0.6	1.3	3.8	4.6	1.8

TABLE 3.1: The dependency of the $Li@C_{60}^+$:C_{60}^+ mass peak ratios on the excitation energy that is used. In all the cases, the laser intensity was selected so that no fragmentation was visible.

	Excitation wavelength / nm	Oscillator strength	Configuration
Excited state	265	0.1171	HOMO-1 $\rightarrow$ LUMO

TABLE 3.2: Computed excitation wavelength, oscillator strength and configuration of the transition in C_{60} which becomes resonant with the 267 nm photon energy. Computed at TD-DFT/CAM-B3LYP/6-31+G*-Bq(6-31(6+)G*).[40]

spectra were recorded to monitor the parent ion peaks' ratio. From the above it was conclude that the presence of C_{60} in the mass spectra is likely to be a result of thermal decomposition reactions that occur in the oven due to the high temperatures.

In the gas-phase measurements, the reduced symmetry of the endohedral molecule results in a larger probability of dipole transitions which have significant oscillator strengths compared to the empty C_{60} molecule. Hence there is a higher probability for electrons in $Li@C_{60}$ to be excited with the laser pulse. Therefore the ratio of the parent ion peaks in the mass spectra is expected to overestimate the relative intensity of $Li@C_{60}$ molecules in the molecular beam. The relative ratios are expected to be dependent on the laser wavelength due to differences in the absorption cross sections and ionisation probabilities. Table 3.1 shows a summary of the ratios when using different excitation wavelengths. The ratio at 267 nm shows a higher intensity for the C_{60} peak while

with all the other wavelengths the relative intensity of Li@C_{60} is higher. The TD-DFT calculations indicated that the reason behind this difference is that there is an intermediate valence excited state in C_{60} which becomes resonant with the first 267 nm photon absorption, resulting in an enhanced ionisation probability. As shown in Table 3.2, the HOMO-1 $\rightarrow$ LUMO transition has a non-zero oscillator strength with an excitation energy of 265 nm.

Another quantitative method for measuring the relative amounts of C_{60} and Li@C_{60} which are sublimed is through the following LT-STM studies. The same starting material was heated with the same temperature and heating time as in a typical gas-phase experiment in order to remove any impurities and allow a direct comparison. Figures 3.4 (a) and (b) show the STM image of a hexagonally closed packed fullerene island which has been deposited on a Au(111) surface. The island was formed by evaporating the previously heated material at 665 K for 4 min and subsequently annealing at 573 K for 30 sec. Both (a) and (b) show the exact same area of the deposited island. (a) was recorded at a bias of -2.5 V and (b) at +2.5 V, imaging the occupied and unoccupied states respectively. In these images, each distinct feature is a fullerene molecule, either C_{60} (empty cage) or Li@C_{60} (filled cage). Four different species have been identified and highlighted with a circle in (a)-(b) and are shown in the highly magnified STM images in (c)-(f). The dI/dV spectra of those four species are displayed in (g) where the colour coding is taken from (c)-(f). The three grey traces in (g) are almost identical which suggests that they correspond to the same molecule, while the red traces shows a substantially different resonance

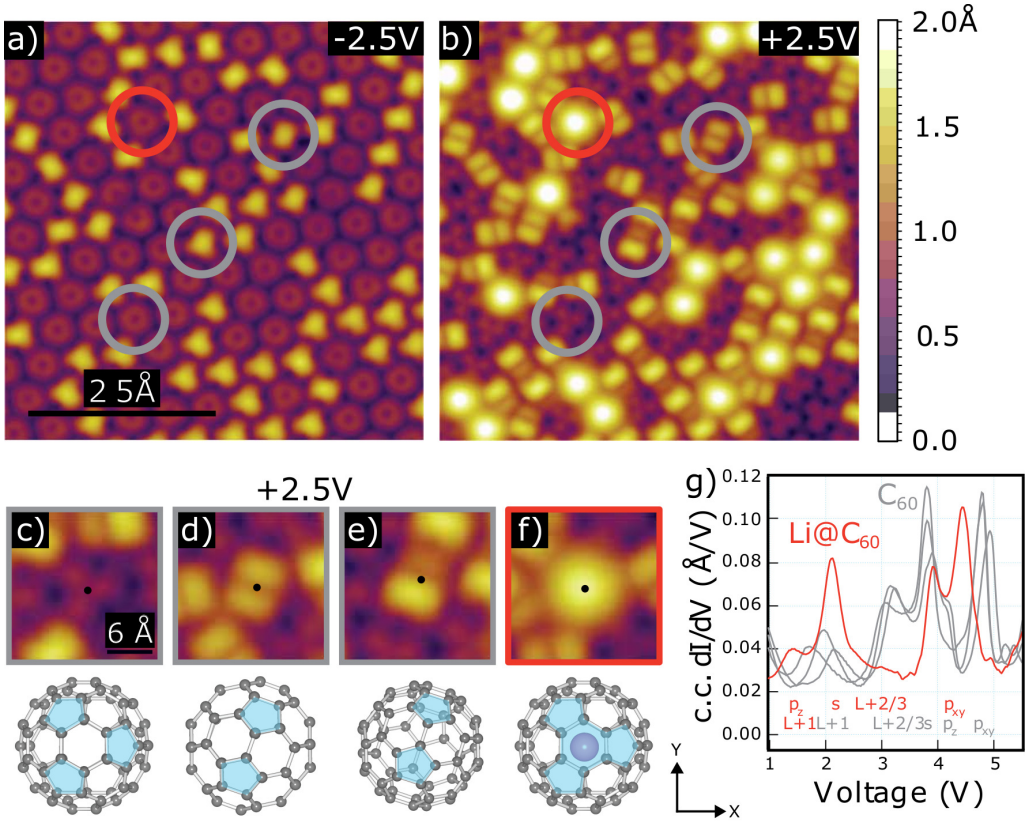

FIGURE 3.4: LT-STM images of a Li@C_{60}/C_{60} island deposited on Au(111) surface. Topographic images of the same area recorded at a bias of (a) -2.5 V and (b) +2.5 V. The four different species that are highlighted in (b) are magnified in (c)-(f). (c) C_{60} fullerene adsorbed on a hexagonal face. (d) C_{60} fullerene adsorbed on a C=C double bond which is joining two adjacent hexagonal faces. (e) C_{60} fullerene adsorbed on a carbon atom which joins two adjacent hexagonal faces and one pentagonal face. (f) Li@C_{60} fullerene adsorbed on a hexagonal face. (g) Constant-current dI/dV spectra of the four different species in (c)-(f). Figure adapted from Chandler *et al.*[90]

structure. Extensive work has already been published on LT-STM measurements of C_{60} deposited on Au(111), where it has been reported that the orientation of the C_{60} molecule affects the topographic image and the dI/dV spectrum.[120,121] Hence by comparing the data of Figure 3.4 with the above studies,

the species highlighted in grey are identified to correspond to C_{60} molecules which are adsorbed on the surface in different orientations. To aid with the visualisation, ball and stick models are provided under the magnified images. In Figure 3.4 (c) the C_{60} molecule is adsorbed with a hexagonal face on the substrate; in (d) it is adsorbed with a C=C double bond which is joining two adjacent hexagonal faces; and in (e) it is adsorbed with a carbon atom which joins two adjacent hexagonal faces and one pentagonal face. The fourth species in (f) shows a diffuse bright circular shape which has no distinct structure, similar to the S-SAMO in C_{60}.[39] That species is thus attributed to Li@C_{60}. From a statistical analysis of large deposited islands, 13% of the absorbed fullerenes were identified as Li@C_{60} while the rest were C_{60}. This ratio is substantially lower than the ones typically found from the gas-phase measurements on fresh material, indicating that the assumptions presented in the previous paragraph are correct.

Moreover, from a statistical analysis it was concluded that all Li@C_{60} molecules exhibited the same orientation, being adsorbed through a hexagonal face. This would suggest that the specific orientation would be the most thermodynamically favourable due to a stronger interaction between the substrate and the molecule with that orientation. Similar observations were reported in a room temperature STM study of Li@C_{60} films.[107] DFT calculations from the same study showed that Li@C_{60} had a stronger interaction with the substrate (binding energy of 2.91 eV) compared to the one for C_{60} with the same orientation (binding energy of 2.24 eV). In addition, they reported that the most energetically favourable orientation of the Li@C_{60} molecules was when they were adsorbed through a hexagonal face and when the Li endohedral atom was 1.54

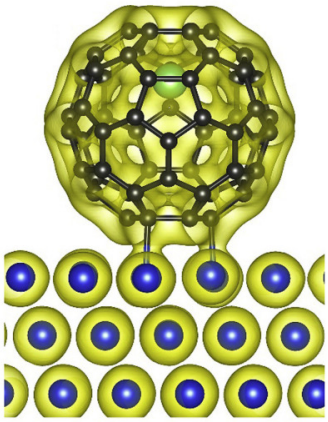

FIGURE 3.5: Computed Li@C_{60} adsorption orientation on Cu(110). In the energetically favourable configuration, the Li atom is 1.54 Å off-centre away from the surface, towards the centre of a hexagonal face. Figure adapted from Yamada *et al.*[107]

Å off-centre, towards the side of the cage that was furthest from the substrate, Figure 3.5.

3.2.2 Gas-phase spectroscopy

VMI images of the photoelectrons from the evaporated Li@C_{60} sample were recorded for a range of laser wavelengths, where the laser intensities were carefully chosen so that no multiple-ionised species or extensive fragmentation was present in the mass spectra. Due to the presence of C_{60} in the mass spectra, the raw VMI and PES data are referred to as Li@C_{60}/C_{60} in the following analysis. Figure 3.6 shows the (a) inverted VMI image, (b) the AI-PES together with the thermal electron background and (c) the AI-PES with the thermal background subtracted of Li@C_{60}/C_{60} for the conditions used to obtain the lowest intensity mass spectrum in Figure 3.2 (540 nm, 35 fs, 9.7 $\pm$ 0.9 TWcm^{-2}).

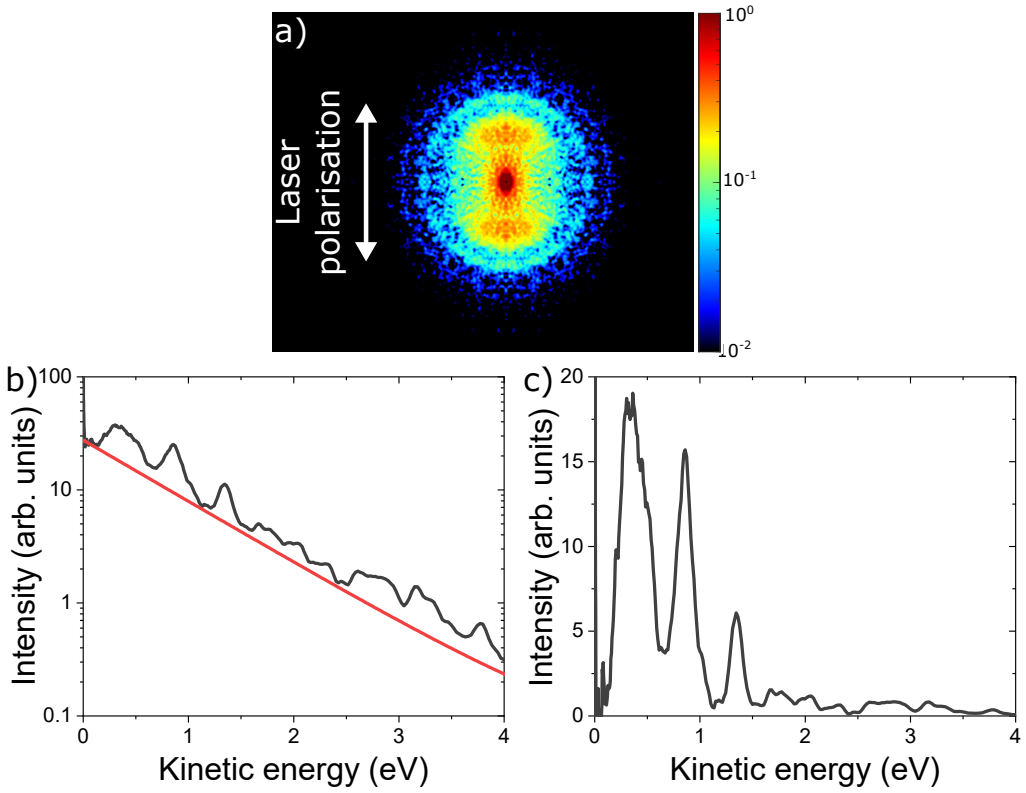

FIGURE 3.6: (a) Li@C_{60}/C_{60} inverted VMI image recorded with 9.7 $\pm$ 0.9 TWcm^{-2}, 540 nm, 35 fs laser pulses. The laser polarisation is indicated with the double headed arrow. (b) AI-PES plotted in a semi-logarithmic scale. The red line corresponds to the fitted thermal electron background. (c) AI-PES after thermal background subtraction.

Due to the fact that the C_{60} beam is formed from heating the material in the oven, it will also produce a signal in the VMI acquisition. Therefore, in order to obtain the pure Li@C_{60} PES signal, the C_{60} component had to be subtracted according to the relative intensities of the peaks in the mass spectra. In addition, for the subtraction to be correct, the C_{60} spectra had to be recorded under identical ionisation conditions compared to the Li@C_{60}/C_{60} samples. Figure 3.7 shows the comparison of the relative intensity of the C_{60} component in the Li@C_{60}/C_{60} PES presented in Figure 3.6 which has to be subtracted.

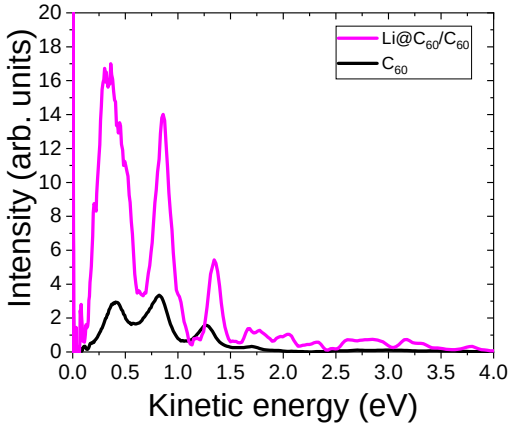

FIGURE 3.7: AI-PES after thermal background subtraction of C_{60} (black) and Li@C_{60}/C_{60}(purple) recorded with 540 nm, 35 fs laser pulses. The intensities have been normalised to indicate the relative contribution of the C_{60} component in the Li@C_{60}/C_{60} data according to the ratio of the peaks in the mass spectrum (Table 3.1).

Following the above subtraction procedure, in Figure 3.8 the AI-PES of the pure Li@C_{60} is compared with the one from C_{60} for a range of different excitation wavelengths. The structure of the Li@C_{60} photoelectron spectra resemble the ones corresponding to the SAMO peaks structure found for C_{60}.[52] However, despite the similarities between the two data sets, differences in the relative intensities and positions of the SAMO peaks are observed. In all the spectra, the grey curves correspond to Lorentzian peak fitting functions. In the Li@C_{60} data more functions were needed to fit the SAMO peaks, suggesting that the peaks were broader or split compared to the C_{60} case.

The assignment of the peaks that were fitted in the PES of Figure 3.8 is based on two criteria. The first is by measuring the gas-phase photoelectron angular distributions for a range of excitation wavelengths to extract the trend of the anisotropy parameter value with respect to the photoelectron kinetic energies

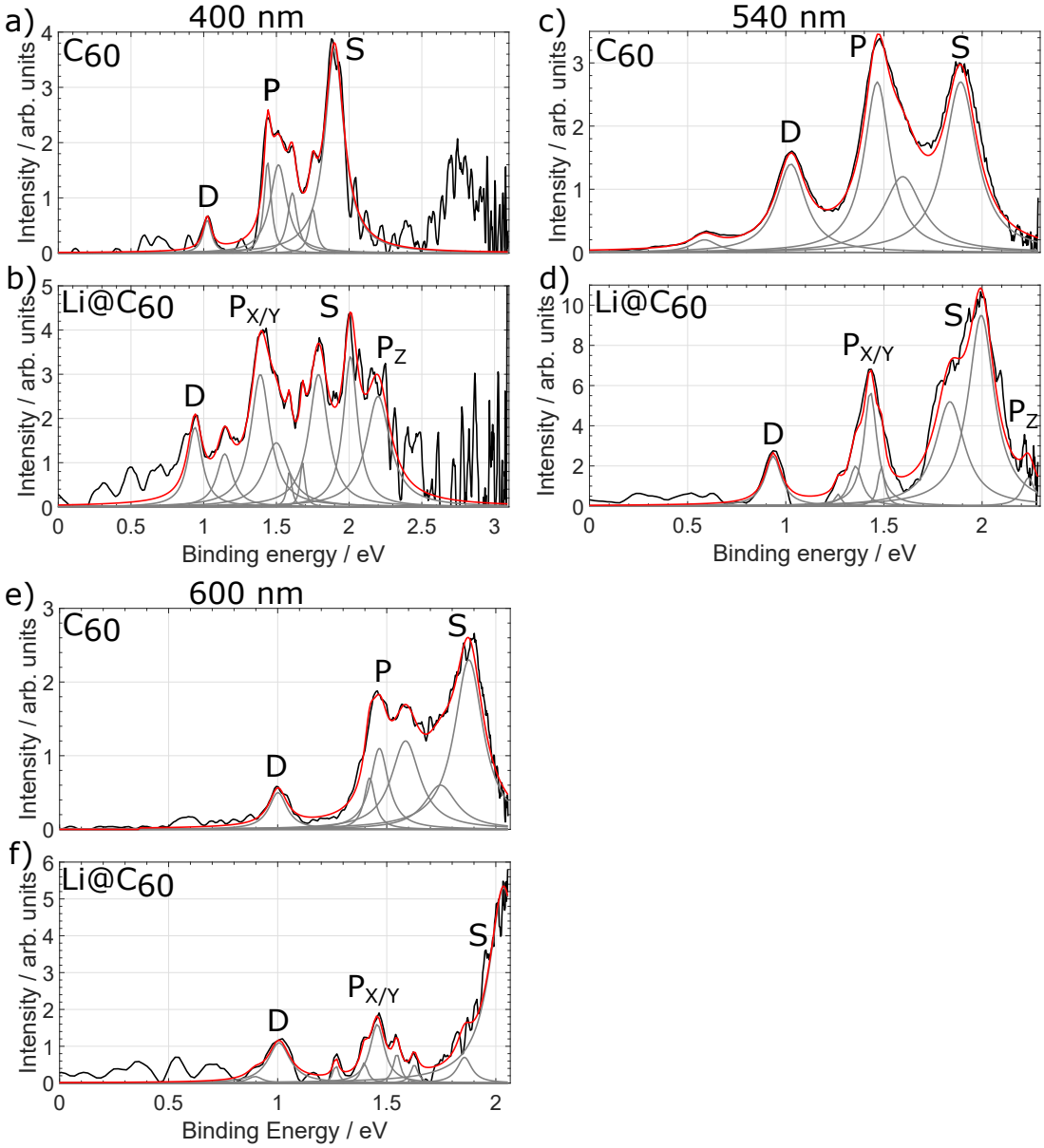

FIGURE 3.8: AI-PES after thermal background subtraction of C_{60} and Li@C_{60} obtained with: (a)-(b) 400 nm, (c)-(d) 540 nm, and (e)-(f) 600 nm respectively. The C_{60} spectra correspond to the C_{60} component which has been subtracted from the original Li@C_{60}/C_{60} data. The grey lines correspond to the single Lorentzian peak fitting functions and the red lines are the summation of those functions.

for a specific peak and comparing this trend with the theoretically computed one. An example of such a analysis is given in Figure 3.9, where the anisotropy parameter for two of the peaks from the 540 nm Li@C_{60} data are determined and from Figure 3.10, where the gas-phase experimental anisotropy parameter values of the S-, P- and D-SAMOs of Li@C_{60} and C_{60} are comared with the calculated ones. The second criterion is by comparing the Li@C_{60} gas-phase SAMO binding energies with the theoretical binding energies (see Table 3.4) as well as the previously determined binding energy values for C_{60}. A summary of the Li@C_{60} SAMO peak assignment is displayed in Table 3.3. The C_{60} values in the last column are calculated by averaging the previously reported values which were recorded with different excitation wavelengths.[52]

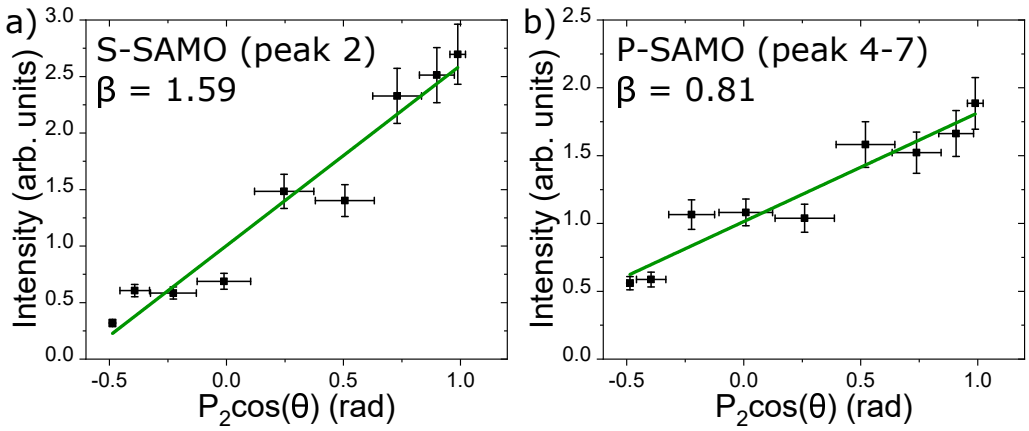

FIGURE 3.9: Angular dependence of the intensity of the (a) S-SAMO and (b) P-SAMO peaks. The value of the anisotropy parameter, β, is calculated by fitting Equation 2.21 to the data. Data shown is for Li@C_{60} recorded with 540 nm, 35 fs laser pulses. (a) peak 2 and (b) peak 4-7 from the labelling in Table 3.3.

Peak no.	SAMO	Binding energy / eV			
		400 nm	540 nm	600 nm	C_{60}
1	P_Z	2.17 ± 0.04	2.22 ± 0.01	-	-
2	S	2.03 ± 0.02	2.00 ± 0.02	2.02 ± 0.03	1.90 ± 0.10
3	S	1.84 ± 0.03	1.82 ± 0.02	1.83 ± 0.03	-
4-7	$P_{X/Y}$	1.40 ± 0.15	1.43 ± 0.06	1.42 ± 0.08	1.47 ± 0.02
8	$P_{X/Y}$	1.13 ± 0.02	-	1.14 ± 0.04	-
9	D	0.97 ± 0.03	0.95 ± 0.02	0.98 ± 0.05	1.02 ± 0.01

TABLE 3.3: Binding energies of the SAMO peaks in Li@C_{60} for a range of excitation wavelengths. The average from previously published values for C_{60}, recorded with different wavelengths, is shown in the last column.[52]

Peak no.	SAMO	Binding energy / eV		
		1.58 Å	0.8 Å	0 Å
-	S_1	3.71	4.30	4.63
2-3	S_2	1.43	1.48	1.53
1	P_Z	1.70	2.00, 2.23	2.63
4-8	$P_{X/Y}$	-	1.87	1.30
9	D	1.15	1.16	1.18

TABLE 3.4: Calculated Li@C_{60} SAMO binding energies for 3 isomers where the Li atom is in different positions (centre of the cage, 0.8 Å and 1.58 Å off-centre) along the axis that passes through the centre of the cage and the centre of a hexagonal face. The most stable isomer is for a Li position of 1.58 Å off-centre. The peak numbering is based on the assignment from Table 3.3. Computed at TD-DFT/CAM-B3LYP/C:6-31+G(d) + Li:6-311+G(2df) + Bq:6-31G(d)5+(SPD).

The anisotropy parameter values of the peaks which have binding energies of 2.02 and 1.82 eV (peaks 2 and 3 respectively in Table 3.3) do not significantly change as a function of the photoelectron kinetic energy, Figure 3.10 (a). This is a characteristic of an electronic state which has an S-like character. However, for a perfectly symmetric S-state, as is the case for C_{60}, the anisotropy parameter should stay constant at a value of 2. Two S-SAMO Li@C_{60} Dyson orbitals were computed, shown in Figure 3.11. In S_1-SAMO, the electron density is

centred on the off-centre Li atom, resulting in the symmetry to break slightly from the perfectly spherical symmetric S-SAMO of C_{60}. The S_2-SAMO's electron density is largely localised outside of the carbon cage. The spherical symmetry is heavily distorted and has a mushroom-like shape where most of the electron density is situated at the opposite side of the cage from where the Li is.

The computed binding energy of the S_1-SAMO, Table 3.4, is substantially higher compared to the rest of the SAMOs by roughly 2 eV. A state with a remarkable high binding energy and having a similar symmetry to the computed S_1-SAMO Dyson orbital has been reported in a recent theoretical investigation of endohedral Li fullerenes.[108] In the study, the authors identify this excited state as a cage-electron state, in contrast to the charge-separated states that typically describe the rest of the valence and superatomic states in $Li^+@C_{60}^-$. They report that the addition of an electron to the Li 2s atomic orbital is the reason behind this cage-electron state. The excitations energies used within the gas-phase experiments presented in this thesis are not high enough to ionise such a state, so it is not expected to appear in the PES. Therefore the focus is directed to the S_2-SAMO.

The computed anisotropy parameter values for the S_2-SAMO, red line in Figure 3.10 (a), oscillates around 1.5. The lower average values indicate that the excited state's wavefunction spherical symmetry is distorted. The gas-phase values of peaks 2 and 3 are in good agreement with the computed values of the S_2-SAMO and thus those peaks are assigned to that state. Interestingly enough, the β values of peak 2 (full squares) are closer to 2 than the ones of peak 3 (full diamonds) which would suggest that the spherical symmetry of

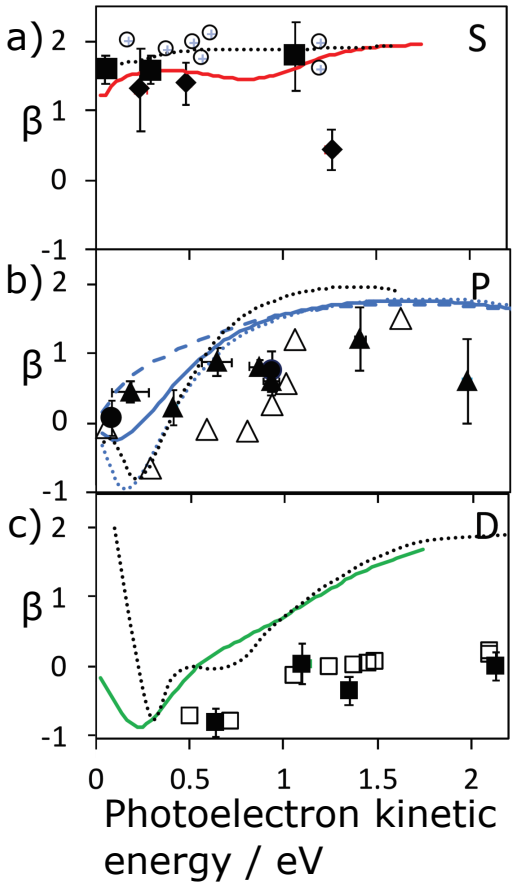

FIGURE 3.10: Anisotropy parameter, β, of the Li@C_{60} SAMO states, (a) S-SAMO, (b) P-SAMO and (c) D-SAMO, plotted against the photoelectron kinetic energy. The TD-DFT calculations which are plotted are for the conformer where the Li atom is 1.58 Å off-centre, towards the centre of a hexagonal face. For comparison, the previously reported C_{60} calculated results as well as the gas-phase experimental values are shown with the black dotted lines and black empty symbols respectively. The labelling for the experimental values is based on Table 3.3 and the labelling of the computed PAD states is based on Table 3.4. (a) S-SAMO: peak 2 = full diamonds, peak 3 = full squares and S_2 state = full red line. (b) P-SAMO: peak 1 = full circles, peaks 4-8 = full triangles, P_Z state = dashed blue line, $P_{X/Y}$ state = dotted blue line and average of the whole P-band = full blue line. (c) D-SAMO: peak 9 = full squares and D state = full green line.

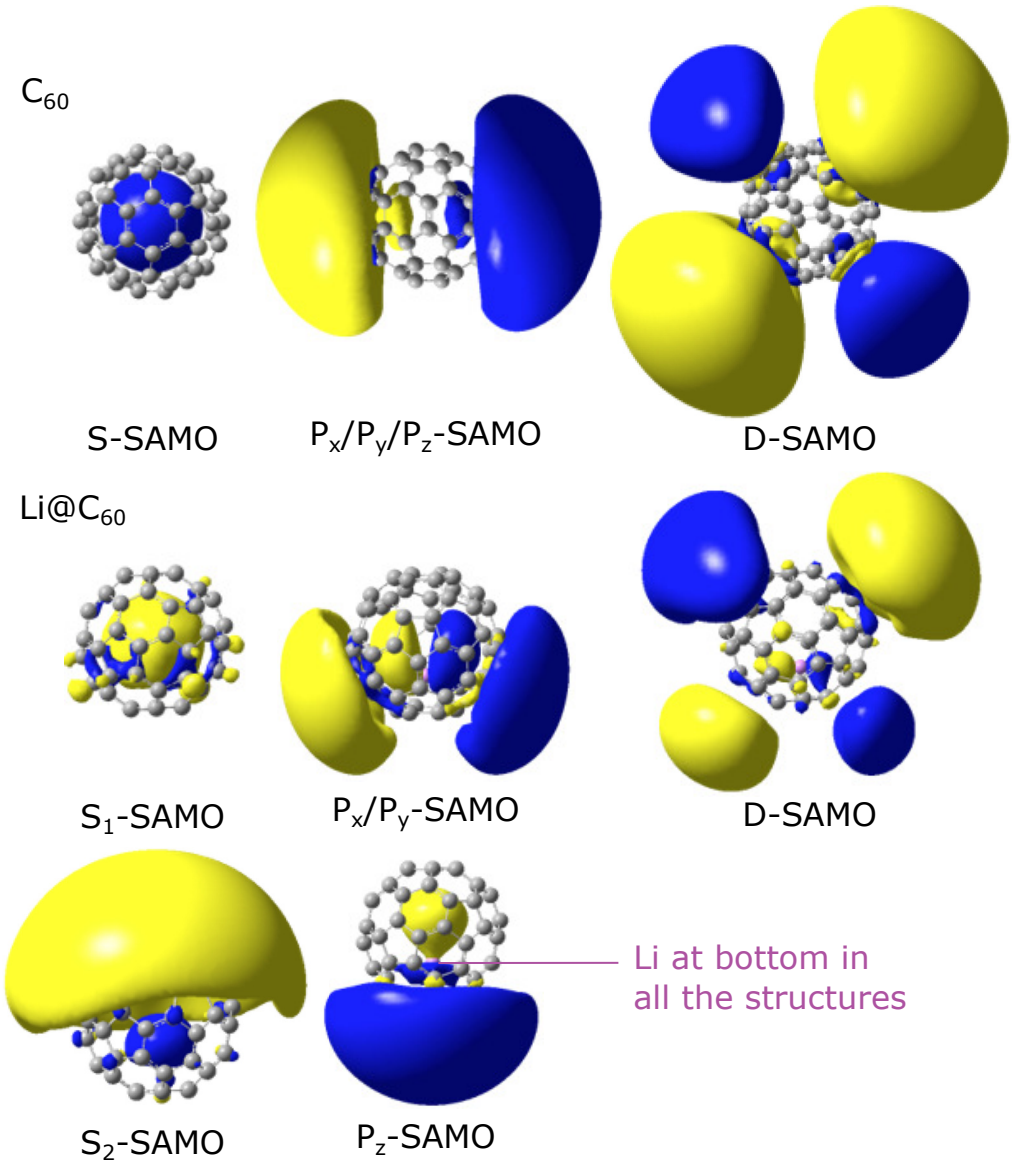

FIGURE 3.11: Dyson orbitals of the S-, P- and D-SAMO states of C_{60} (top) and Li@C_{60} (bottom). Computed at TD-DFT/CAM-B3LYP/C:6-31+G(d) + Bq:6-31G(d)5+(SPD) for C_{60} and TD-DFT/CAM-B3LYP/C:6-31+G(d) + Li:6-311+G(2df) + Bq:6-31G(d)5+(SPD) for Li@C_{60}. The Li atom in Li@C_{60} is placed 1.58 Å off-centre, towards the centre of a hexagonal face.

the state from peak 3 is more strongly distorted. As will become clear from the following paragraphs, due to the high temperatures in the experiments, the Li

atom does not stay in a fixed position. In addition, from computations where the Li atom in Li@C_{60} is placed at the centre of the cage, the S-SAMO retains the overall spherical symmetry.[45,122] From the above information it is suggested that peak 2 may originate from an S-state where the Li atom is at the centre of the cage while peak 3 from an S-state where the Li atom is off-centre. Overall, both peaks are assigned as the S-SAMO which has the S_2-SAMO Dyson orbital symmetry.

The second set of peaks with binding energies around 2.20 eV (full circles) and 1.42 and 1.13 eV (full triangles) (peaks 1, 4-7 and 8 respectively in Table 3.3) exhibit an almost linear increase of the anisotropy parameter as a function of the photoelectron kinetic energy between 0 and 1.5 eV, Figure 3.10 (b). A similar observation was made for the P-SAMO of C_{60}, empty triangles.[27] From the P-SAMO Dyson orbitals it is clear that the off-centre Li atom has a stronger influence on the symmetry of the P_Z component, the dimension which passes from the centre of the cage and the endohedral atom, while the two perpendicular components, P_X and P_Y, are only slightly distorted when compared with the C_{60} P-SAMO (the lobes of the P_X and P_Y Li@C_{60} SAMOs are bent slightly towards the side of the cage where the Li atom is). Hence, the trend of the β values for the x- and y-components is expected to be similar to the C_{60} data. The two-lobe structure has completely changed in the P_Z-SAMO, having mainly one lobe localised outside the cage towards the side where the Li atom is. The effect of the symmetry difference between the P-SAMOs is clearly seen in the computed anisotropy parameters where the x- and y-components (dotted blue line) are very similar to the C_{60} data (black dotted line) while the z-component is not; the dip below 0.5 eV is missing (dashed blue line). Due

to the agreement between the computed PADs with the experimental values, this set of peaks are labelled as P-SAMO. From the calculated binding energies shown in Table 3.4, the P_Z-SAMO has a binding energy even larger than the S-SAMO. A similar behaviour in the binding energies is seen from peak 1 in the gas-phase measurements. Therefore it is concluded that peak 1 is originating from the P_Z-SAMO while peaks 4-8 from the $P_{X/Y}$-SAMOs. Further confirmation of the P_Z-SAMO assignment is provided from the STS analysis in Chapter 3.2.4. Lastly, the splitting of the P-SAMOs into several peaks can be explained due to the fact that the degeneracy of these states is lifted given that their symmetries are so different, as well as the fact that the Li atom moves inside the cage during the gas-phase experiments.

The Li@C_{60} D-SAMO Dyson orbital has most of the electron density outside of the cage and as such the Li atom does not greatly affect the symmetry when compared to the C_{60} orbital (Figure 3.11), hence the computed β values are similar (Figure 3.10 (c)). The β values of the peak with an average binding energy of 0.96 eV are close to the experimental values for the D-SAMO in C_{60}. Due to the above comparison, peak 9 is assigned as the D-SAMO of Li@C_{60}. The similarity of the gas-phase values between the two molecules confirms that the Li atom does not affect greatly the symmetry of these states.

As has been shown theoretically, in Li@C_{60} the Li atom is only loosely bound inside the fullerene cage.[105,106] So one would expect that with the elevated temperatures in the gas-phase experiments, the Li atom can move inside the cage into different positions. Thus accessing a large variety of isomers which will affect the excitation energy of the excited electronic states. To estimate how the SAMO energies are affected by the Li position, calculations were performed

for three different isomers; placing the Li atom in the centre of the cage and 0.8 Å and 1.58 Å off-centre, along the axis which connects the centre of the cage with the centre of a hexagonal face. The most stable isomer is for a Li position of 1.58 Å off-centre which is comparable with recent theoretical investigations (1.5 Å).[45,108] As shown in Table 3.4, the SAMO binding energies are indeed affected by the Li position. This would explain why several Lorentzian peaks are required to fit the PES, the Li atom indeed moves inside the cage during the measurements. When compared with the experimental values from Table 3.3, the computed energies differ by several meV. Therefore, for a more reliable comparison the experimental Li@C_{60} SAMO binding energies are compared with the experimental C_{60} values, as it has been portrayed in the analysis in the previous paragraphs and as shown in Table 3.3.

The photoelectron spectra of Li@C_{60} and C_{60} recorded with 267 nm laser pulses are shown in Figure 3.12. As has been demonstrated in a previous study, the C_{60} spectrum taken with 267 nm fs pulses shows no indication of a thermal background and no SAMO peak structure is visible.[22] This is in contrast to the results when using 267 nm ns pulses where thermal electron emission is observed.[123] As is characteristic with Rydberg Fingerprint PES, the signal cut-off in both cases is around the photon energy, 4.55 eV. Therefore Rydberg-like states are expected to be responsible for the features which will be identified. With 267 nm fs pulses, the first photon absorption does not have a high enough energy to populate the SAMO states in C_{60} since the photon energy is smaller than the excitation energy required to populate the lowest SAMO state, which is 5.7 eV. Absorption of a second photon would directly lead to ionisation. In Figure 3.12 (b) there is a low intensity tail that extends to roughly 4.55 eV. This

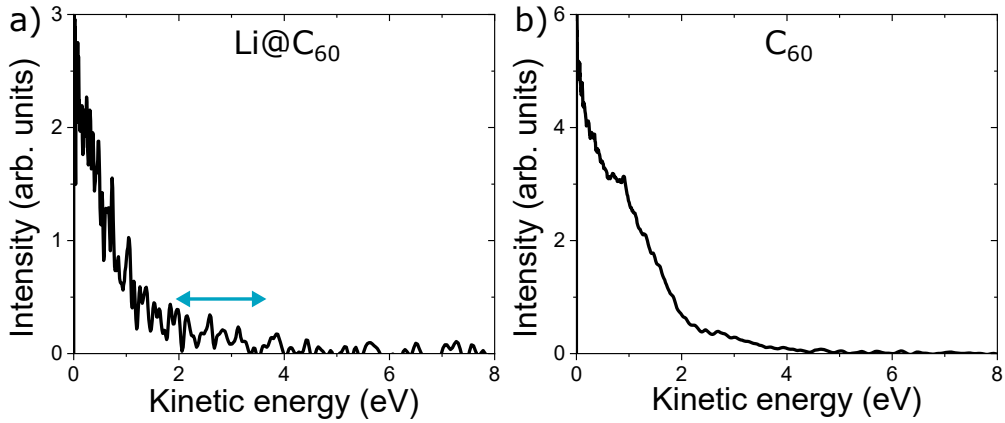

FIGURE 3.12: AI-PES, without the thermal electron background subtraction of (a) Li@C_{60} and (b) C_{60} obtained with 267 nm. The double-headed arrow in (a) indicates the low intensity structure which is associated to be originating from the SAMO states. No such structure is seen in (b).

would suggest that an energy relaxation mechanism exists in C_{60} where highly excited valence states and unresolved Rydberg states are populated and are subsequently ionised through a 3-photon process.

Given that Li@C_{60} has a lower ionisation potential than C_{60}, the excitation energy to populate the lowest SAMO state is below the photon energy at 4.5 eV (S-SAMO with a binding energy of roughly 2 eV). Due to the lower symmetry of the endohedral molecule, direct optical excitations to the SAMO states are allowed, as is portrayed from the non-zero oscillator strengths from the TD-DFT calculations in Table 3.5. This is in contrast to C_{60} where direct optical excitation to the S-SAMO state is forbidden due to the selection rules. Despite having noisy data, a small intensity structure can be identified in the region of 2-3.5 eV in the PES of Li@C_{60} which is similar to the SAMO peak structure that has been identified with different excitation energies. A conclusive assignment, however, is not possible due to the poor signal to noise ratio.

Peak no.	SAMO	Transition dipole moment / a.u.
-	S_1	0.06
2-3	S_2	0.63
1	P_Z	0.04
4-8	$P_{X/Y}$	-
9	D	0.09

TABLE 3.5: Calculated Li@C_{60} SAMO transition dipole moments for the most stable isomer, having the Li positioned 1.58 Å off-centre, along the axis that passes through the centre of the cage and the centre of a hexagonal face. The peak numbering is based on the assignment from Table 3.3. Computed at TD-DFT/CAM-B3LYP/C:6-31+G(d) + Li:6-311+G(2df) + Bq:6-31G(d)5+(SPD).

3.2.3 Surface bound

Scanning tunnelling spectroscopy is a technique that probes the occupied and unoccupied orbitals of a surface bound molecule. The C_{60} and Li@C_{60} spectra shown in Figure 3.4 (g) are that of molecules that are within a deposited island of fullerenes. Given that interactions from neighbouring molecules will affect the local electronic density of the target molecule, STS spectra had to be acquired for isolated molecules. As a result, comparison with the gas-phase studies and DFT calculations would be possible. It should be noted that at the time of the investigation, the TD-DFT calculations described earlier were not performed and the assignment of the peaks in the STS spectra was preliminarily made by qualitatively analysing the ground state DFT calculations of the isolated molecules.

As is shown from Tables 3.6 and 3.7, care was taken to find the right level of theory that would match as accurately as possible the gas-phase HOMO-SAMO and LUMO-SAMO gaps of C_{60} and use that to estimate the energies of Li@C_{60}, Table 3.8. The assignment of the computed orbitals was made by

analysing the symmetries of the molecular orbitals (MOs) as seen from Figures 3.13 and 3.14. In the optimised structure, the encapsulated Li atom is 1.58 Å off-centre towards the centre of a hexagonal face, staying in accordance with the TD-DFT calculations from the previous section and with published results.[105–108]

	Δ(HOMO-X) / eV				
X=	LUMO	S-SAMO	P-SAMO	D-SAMO	2S-SAMO
Experimental gas-phase	1.60	5.70	6.13	6.60	6.70
B3LYP /6-31+G(d)	2.72	6.12	6.92	7.40	7.66
CAM-B3LYP /6-31+G(d)	4.89	8.17	8.93	9.35	9.63
PBE0 /6-31+G(d)	1.65	5.22	6.07	6.55	6.71

TABLE 3.6: Comparing the computed C_{60} HOMO-LUMO and HOMO-SAMO energy differences at different level of theories with the gas-phase experimental results.

	Δ(LUMO-X) / eV			
X=	S-SAMO	P-SAMO	D-SAMO	2S-SAMO
Experimental gas-phase	4.10	4.53	5.00	5.10
B3LYP /6-31+G(d)	3.40	4.20	4.67	4.94
CAM-B3LYP /6-31+G(d)	3.28	4.04	4.46	4.74
PBE0 /6-31+G(d)	3.57	4.42	4.91	5.07

TABLE 3.7: Comparing the computed C_{60} LUMO-SAMO energy differences at different level of theories with the gas-phase experimental results.

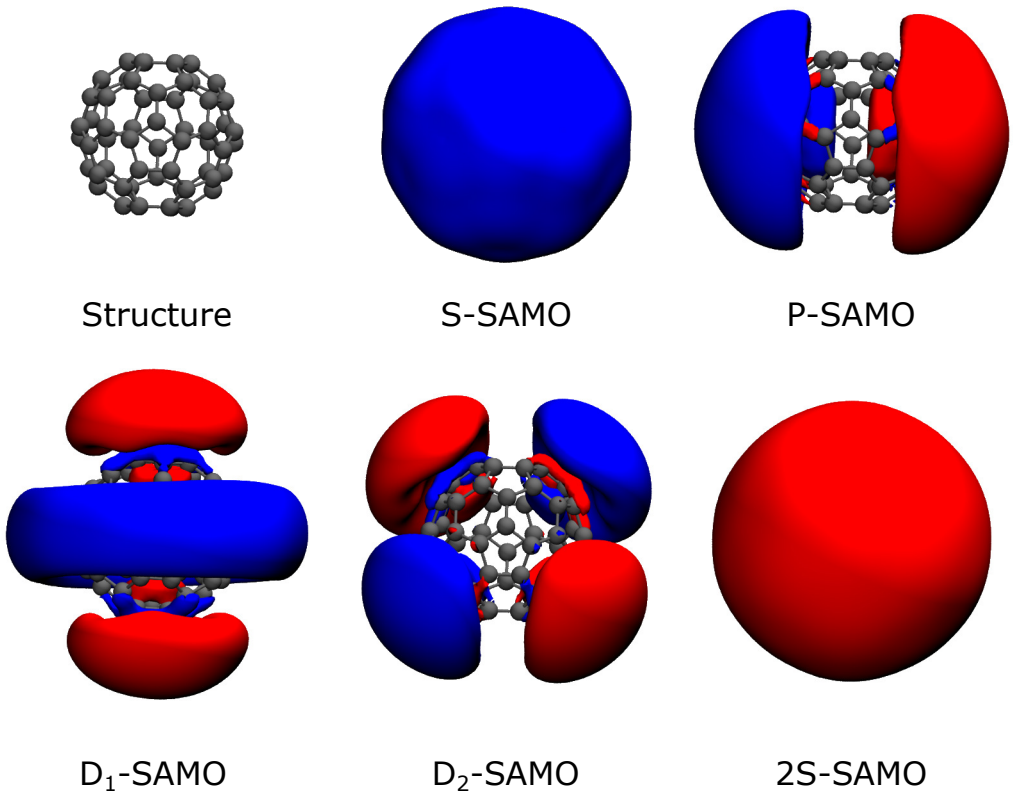

FIGURE 3.13: C_{60} SAMO MOs computed at the DFT/PBE0/6-31+G(d) level.

	Δ(LUMO-X) / eV				
X=	$S_{(2)}$-SAMO	$P_{X/Y}$-SAMO	P_Z-SAMO	D-SAMO	2S-SAMO
Li@C_{60} PBE0 /6-31+G(d)	4.03	3.82	3.94	5.01	5.99
C_{60} PBE0 /6-31+G(d)	3.57	4.42		4.91	5.07

TABLE 3.8: Comparing the computed Li@C_{60} and C_{60} LUMO-SAMO energy differences at the DFT/PBE0/6-31+G* level.

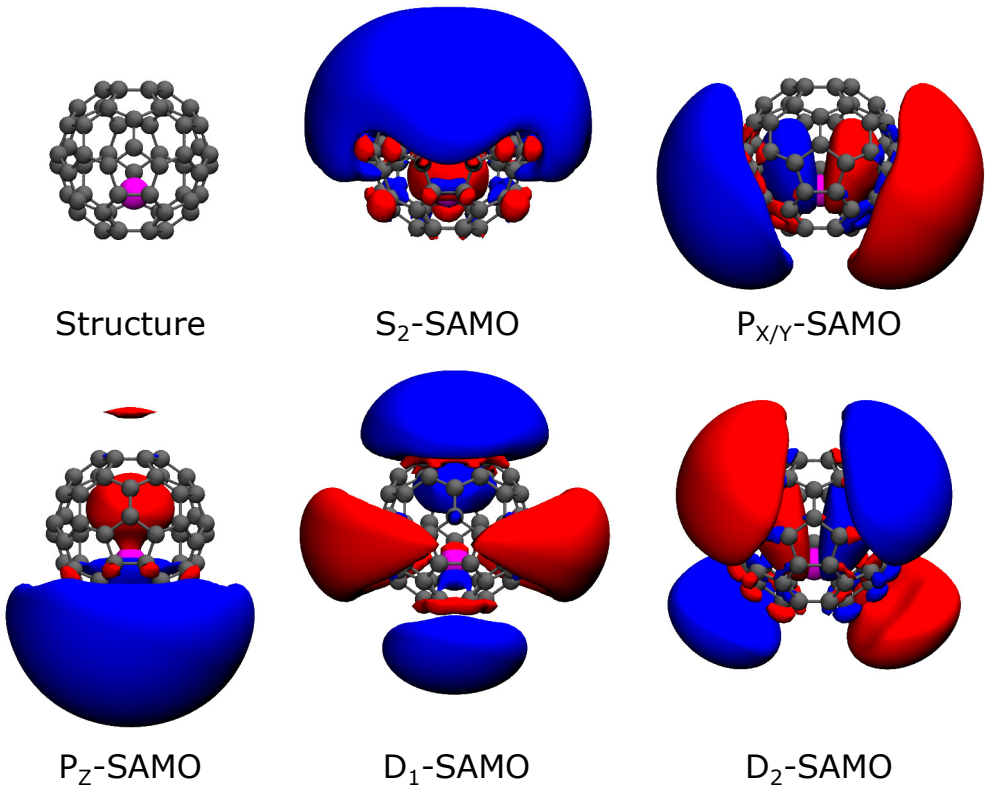

FIGURE 3.14: Li@C_{60} SAMO MOs computed at the DFT/PBE0/6-31+G(d) level.

The computed local density of state (LDOS) graphs are shown in Figure 3.15 (a) and (c) for C_{60} and Li@C_{60} respectively where the energy scale has been normalised so that the Fermi level = 0 eV. For C_{60}, the Fermi level is the mid-point between the HOMO-LUMO gap while for Li@C_{60}, it is at the SOMO (Singly Occupied Molecular Orbital). In (b) and (d) the corresponding constant current dI/dV spectra of the isolated molecules which are deposited on a Au(111) substrate are displayed. Using topographic imaging, it was identified that both of the isolated molecules were adsorbed with the same cage orientation. Therefore, any discrepancies between the two spectra would be a direct

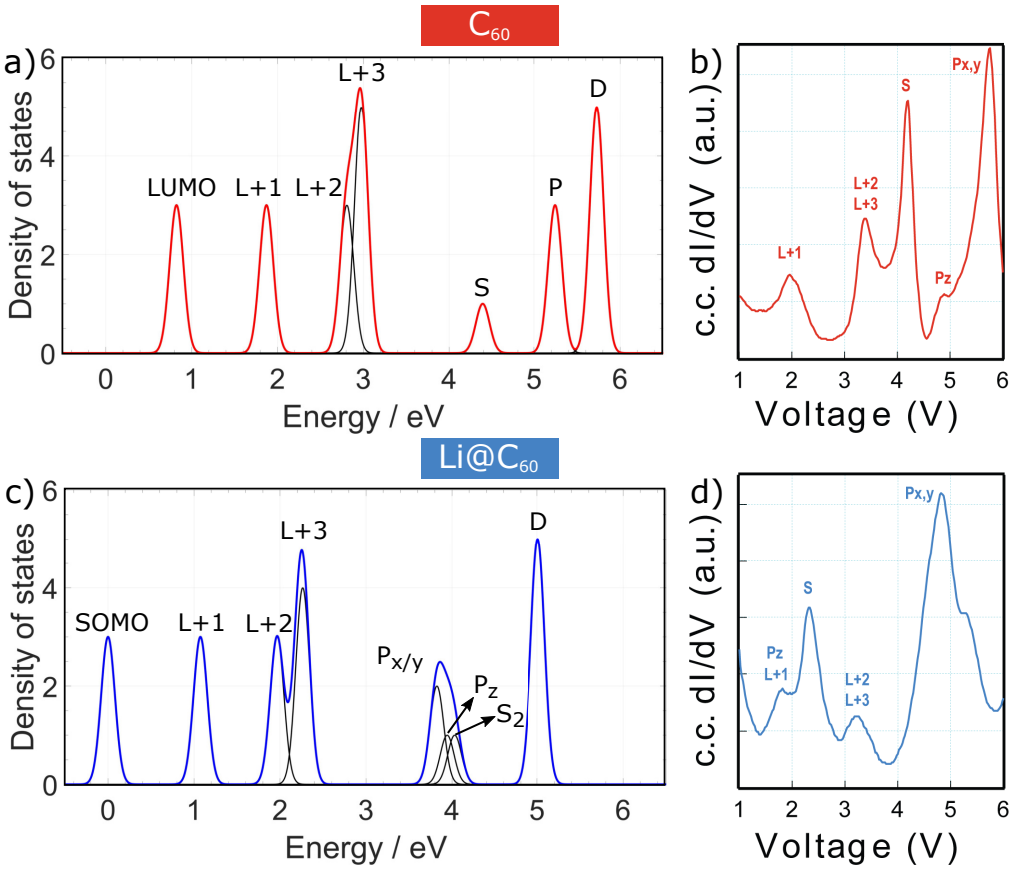

FIGURE 3.15: LDOS of isolated molecules for (a) C_{60} and (c) Li@C_{60} computed at the DFT/PBE0/6-31+G(d) level. The energy scale has been normalised so that the Fermi level = 0 eV. For C_{60} this is the midpoint between the HOMO and the LUMO states while for Li@C_{60} it is at the SOMO. Experimental constant current dI/dV spectra of (b) C_{60} and (d) Li@C_{60} deposited on a Au(111) substrate.

result of the presence of the Li atom inside one of the cages.

Bonding and charge transfer between a C_{60} molecule and a metal substrate have been shown to stabilise the fullerene electronic resonances. The varying degrees of stabilisation depend on the nature of the substrate where Au(111) was shown to be the least reactive.[124] Given that Li@C_{60} is a radical species which has a non-uniform charge distribution on the fullerene cage, it is more

strongly bound to substrates, leading to an increased degree of stabilisation compared to the C_{60} case. Moreover, at the low temperatures where the samples are probed, $\sim$5 K, the Li atom is expected to be fixed in space in the off-centre position closer to the hexagonal face which is furtherest from the substrate, in contrast to the gas-phase experiments where the Li atom is moving inside the cage. This results in keeping the SAMOs at specific orientations with respect to the metal surface; the S- and P_Z-SAMOs will be orthogonal while the $P_{X/Y}$-SAMOs will be parallel to the substrate.

Because no metal substrate was included in the calculations, the computed absolute peak values are not reliable, however certain trends can be recovered from the data. From a qualitative comparison between the DFT LDOS and the experimental spectrum of C_{60}, the resonance peaks can be identified in Figure 3.15 (b). The degeneracy of the P-SAMOs is lifted from interactions with the metal substrate where the P_Z-SAMO is shifted to lower energies than the $P_{X/Y}$-SAMOs.[125] The reason behind this phenomenon is the higher degree of overlap between the P_Z-SAMO and the metal substrate's d-orbitals which stabilises the SAMO resonance. The orientation of the P_Z-SAMO is such that it is situated perpendicular to the metal surface and could thus penetrate it more efficiently, whereas the $P_{X/Y}$-SAMOs are parallel to the metal surface, pictorially seen in Figure 3.16. The assignment was also confirmed by comparing the peak positions with previously reported data for C_{60}.[120,125]

The computed LDOS of Li@C_{60}, Figure 3.15 (c), shows a similar peak pattern to the computed LDOS of C_{60}, however all the peaks have been shifted to lower energies. This overall stabilisation can be explained from the effect of hybridising the Li atomic orbitals with the fullerene orbitals. The degree of stabilisation

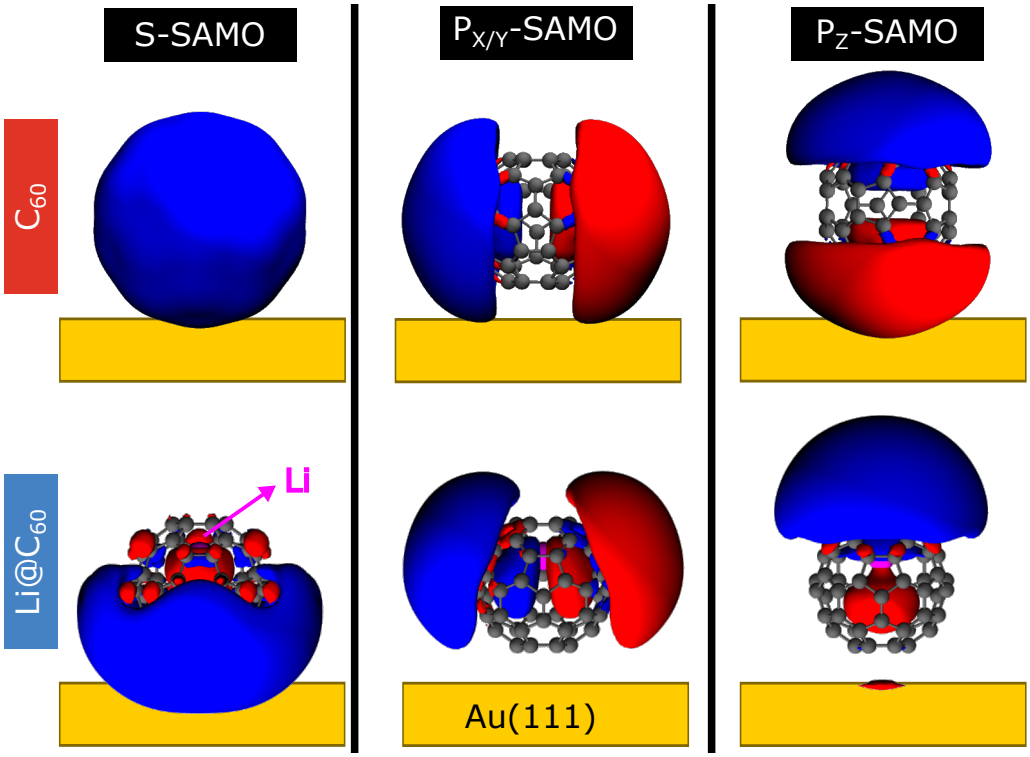

FIGURE 3.16: Visualisation of the C_{60} and Li@C_{60} S-, $P_{x/y}$- and P_z-SAMO orbitals overlap with the metal substrate. The distance between the bottom fullerene hexagonal face and the metal substrate has been normalised according to an STM study of C_{60} molecules adsorbed on a Au(111) surface.[126]

is different between the LUMOs and the SAMOs. All LUMOs exhibit a similar shift of ∼0.8 eV whereas the SAMOs show a varying degree. The most notable differences between the two calculated LDOS is that: for Li@C_{60} (i) the S_2-SAMO is found at a slightly higher energy than the P-SAMOs and (ii) due to the different symmetries, the P-SAMOs do not hold their degeneracy and are split into 2 peaks corresponding to the $P_{X/Y}$- and P_Z-SAMOs. Feng *et al.* reported similar observations in the comparison between the computed LDOS of isolated C_{60} and Li@C_{60} molecules.[39] In their calculations however, the encapsulated Li atom was placed in the centre of the cage, thus maintaining the

icosahedral symmetry.

The experimental Li@C_{60} data, Figure 3.15 (d), show similar observations to what was seen with the calculated LDOS. All of the peaks have been stabilised but the amount of stabilisation varies between the LUMOs and the different SAMOs. Given that the Li@C_{60} SAMOs have distorted shapes compared to the C_{60} SAMOs, the amount of coupling between the individual SAMOs and the metal substrate will alter and hence the degree of stabilisation will be different compared to C_{60}. With the above in mind and by comparing the experimental and computed spectra, the assignment of all of the peaks apart from the P_Z-SAMO was possible. After consideration of the results from the Li-switching section (Chapter 3.2.4), and comparison with the gas-phase data (Table 3.3) and TD-DFT calculations (Table 3.5) where a P-like orbital was seen at higher binding energies than the S-SAMO, the peak at 1.7 V is assigned to the P_Z-SAMO with possibly some contribution from the LUMO+1 state. The sharp peak just above 2 V is the S-SAMO which is the electronic state which was responsible for the bright, circular image that was identified in Figure 3.4 (b) when the acquisition bias was set to +2.5 V. This peak has been stabilised greatly, $\sim$2 V lower compared to C_{60}. The enhanced stabilisation of both the P_Z- and S-SAMO in Li@C_{60} is partly due to the stronger coupling of the molecule with the surface, resulting from the polarised charge distribution on the fullerene cage, and partly due to the asymmetric shape of the SAMO orbitals. As seen in Figure 3.16, at the thermodynamically favourable position where the Li atom is positioned furthest away from the metal substrate, most of the electron density of the S-SAMO is on the side of the substrate. This potentially results in an increased overlap and thus stronger coupling between the S-SAMO and

the metal d-orbitals. Although from the Figure one would expect that the C_{60} P_Z-SAMO will have a larger overlap with the metal substrate compared to the Li@C_{60} P_Z-SAMO, the higher reactivity of the endohedral molecule may result in the increased stabilisation that is seen in the experimental spectra, $\sim$3 V lower compared to C_{60}. The broad peak at 4.5-5.5 V is assigned to the $P_{X/Y}$-SAMO and the shoulder on the right hand side of the peak indicates some contribution from some higher LUMO+X state.

In order to compare the experimental gas-phase SAMO binding energies with the SAMO resonant energies recorded with STS, the LUMO-SAMO energy differences were investigated. Because it was not possible to record the C_{60} LUMO state when the deposition was on the Au(111) subtrate, the discussion below will be based on the STS spectra taken for fullerenes deposited on a O/Cu(110) substrate.[89] The values in Table 3.9 are produced by taking into account the following: for Li@C_{60} the resonant energies correspond to the SOMO-SAMO differences due to the molecule being a radical, having an unpaired electron; the gas-phase ionisation energy of C_{60} is taken to be 7.6 eV;[110] the HOMO-LUMO gap to be 1.6 eV;[127] and the gas-phase ionisation energy of Li@C_{60} is taken to be 6.5 eV.[111] For C_{60} deposited on the O/Cu(110) substrate the stronger shift is seen for the S-SAMO (0.9 eV), followed by the P_Z-SAMO (0.5 eV) and then the $P_{X/Y}$-SAMO (0.1 eV). For Li@C_{60} the overall trend is similar but the shifts are larger. The P_Z-SAMO has the stronger shift (3.1 eV) followed by the S-SAMO (2.4 eV) and the $P_{X/Y}$-SAMO ($\sim$1.0 eV). Similar to what was discussed earlier, the larger shifts for the endohedral molecule are explained due to the higher reactivity of the molecule with the metal substrate and due to the asymmetric shapes of the S- and P_Z-SAMO electron densities.

	ΔE(LUMO-SAMO) / eV			
	C_{60} on O/Cu(110)	C_{60} PES	Li@C_{60} on O/Cu(110)	Li@C_{60} PES
S-SAMO	3.2	4.1	2.1	4.5
P_Z-SAMO	4.0	4.53	1.2	4.3
$P_{X/Y}$-SAMO	4.4	4.53	4.0-4.7	5.0-5.4

TABLE 3.9: Differences between the LUMO-SAMO energy gaps of C_{60} and Li@C_{60} when comparing the gas-phase data with the STS of the molecules deposited on a O/Cu(110) substrate. The gas-phase ionisation potential of Li@C_{60} was taken to be 6.5 eV[109] and for C_{60} the ionisation potential was taken to be 7.6 eV and the HOMO-LUMO energy gap to be 1.6 eV.[127]

3.2.4 Li switching

The following section will focus on the manipulation of the endohedral atom of a surface bound Li@C_{60} molecule and will show how the SAMOs play a key role in the switching phenomenon.

Molecular electronics is the field of study which aims at fabricating electronic components which are made up from molecular building blocks, in the hope of surpassing the semiconductor material's physical limit associated with miniaturising electronic devices. This concept was first proposed by Aviram and Ratner where they theoretically designed a unimolecular rectifier.[128] Since then, various different molecular devices have been developed which mimic functionalities from solid state macroscopic devices such as wires, transistors and switches.[54,129,130] A molecular switch is a device which can adopt two or more stable states (ie. magnetic, conductance, conformational) and can interchange reversibly between them upon the application of an external stimuli, ie. an electric or magnetic field. Such devices could effectively be used for data storage and data transport. With current employed technologies a single bit of

information, either 0 or 1, is made up of around 1 million atoms. Molecular switches could drastically reduce this number, thus creating high density memory storage devices.

In the scope of advancing solid state technologies even further, a single molecule switch which has more than two states can result in even higher memory storage densities. An example of such a molecular switch is proton transfer in the tetraphenyl-porphyrin molecule which is initiated using an STM tip to access four distinct molecular states.[131] Such multi-state switches can often involve large complex molecules which undergo very intricate physical and chemical processes to perform. Endohedral fullerenes have been shown to posses the ability to act as single-molecule multi-state switches by manipulating the position of the endohedral species. Due to the stable carbon shell, endohedral fullerenes offer the advantage of not compromising the molecular integrity during a switching event. Making them desirable for molecular switching applications as they could maintain electrical contact, independent of the active state, when they are incorporated into nano-architectures. The current-driven axial rotation of Sc_3N in $Sc_3N@C_{80}$ is an example where 6 independent switching states were identified for a single molecule.[54]

As was shown earlier in this chapter, when Li@C_{60} is adsorbed on a metal surface at the near liquid helium temperatures that the experiments are performed at, the encapsulated Li atom is stabilised in an off-centre position. Therefore the presence of the metal surface effectively lifts the degeneracy of all the hexagonal faces of the C_{60} cage, resulting in 6 'levels' of hexagonal and pentagonal faces within the cage. In both the ball and stick model and the

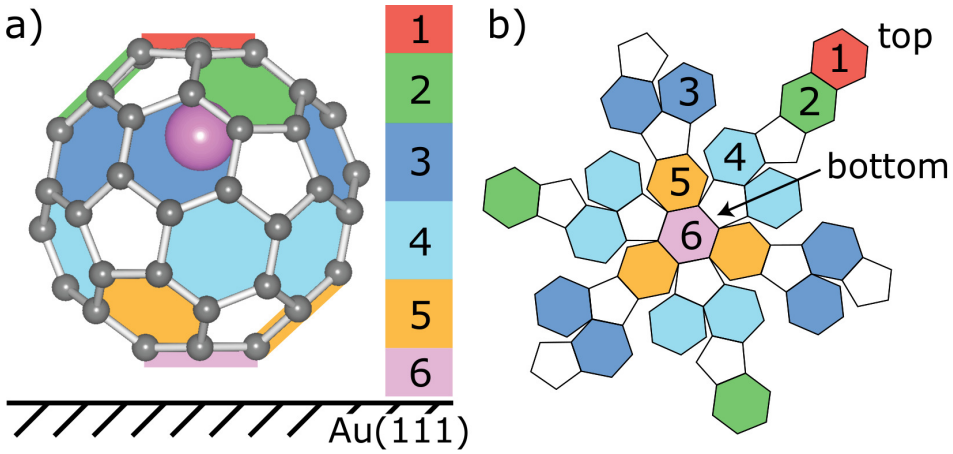

FIGURE 3.17: Colour-coding the 6 different levels of hexagonal faces on the C_{60} cage when Li@C_{60} is adsorbed on a metal substrate. (a) side perspective of the ball and stick model. (b) deconstructed cage diagram. A colour-coded Schlegel diagram is provided in the Appendix Figure A.1.

deconstructed cage diagram in Figure 3.17, the hexagonal faces corresponding to the different levels have been colour-coded. It should be noted that this colour scheme will be used in the remainder of this section to identify each level. Given that in the thermodynamically favourable position the Li atom is closest to the hexagonal face that is furthest from the metal substrate, that orientation has been labelled level 1. As is shown from the diagrams, the distribution of the hexagonal faces around the surface of the cage has a 1:3:6:6:3:1 ratio for levels 1 to 6 respectively, totalling in 20 hexagonal faces all together. Levels 1 (red) and 6 (pink) have 1 hexagonal face each. Levels 2 (green) and 5 (orange) have 3 hexagonal faces each. The faces in each level have a 3-fold symmetric distribution (rotated by 120°) and between the two levels the faces are mirror-symmetric (rotated by 180°). Levels 3 (blue) and 4 (cyan) have three pairs of adjacent hexagonal rings (sharing a C=C double bond) which have a 3-fold symmetric distribution across each level and between the two levels they

are mirror-symmetric. Therefore if the Li atom can be controllably relocated between all the hexagonal faces of the cage, Li@C_{60} could in theory act as a single-molecule 20-state switch.

This is not however the first time Li@C_{60} has been experimentally investigated for its ability to act as a molecular switch. Previous studies were based on applying temperature on the bulk $[Li@C_{60}]^+[PF_6]^-$ salt to initiate a phase transition.[132–135] Above 100 K, the Li^+ cations are able to move inside the cage via hopping and tunnelling motions between the 20 potential wells which are under each hexagonal face. At 100-24 K, the Li^+ motion is limited to only tunnelling between two specific opposite hexagonal faces. And below 24 K, only one of those two states is preferentially populated due to interactions between the Li^+ cations and the PF_6^- anions. However, in all of these studies the researchers were not able to achieve either control or identification of a switching event from a single molecule. Using a low-temperature STM apparatus switching events can be explored and facilitated with atomic precision.

As is shown from the DFT MOs, Figure 3.14, the S- and P_Z-SAMOs of Li@C_{60} are most strongly affected by the encapsulated atom. Their rotational axis of symmetry will always follow the axis that passes through the centre of the cage and the Li atom. Therefore, by having the metal substrate as a fixed frame of reference, relocating the position of the Li atom will effectively shift the electron density of those SAMOs in space. This is schematically shown in Figure 3.18 where the DFT MOs of the S- and P_Z-SAMOs of the potential 6 different Li level orientations are illustrated. Since the fullerene SAMOs extend beyond the carbon cage itself, moving the Li atom will vary the degree of overlap between the SAMO electron cloud and the d-orbitals of the metal substrate.[40,136] This

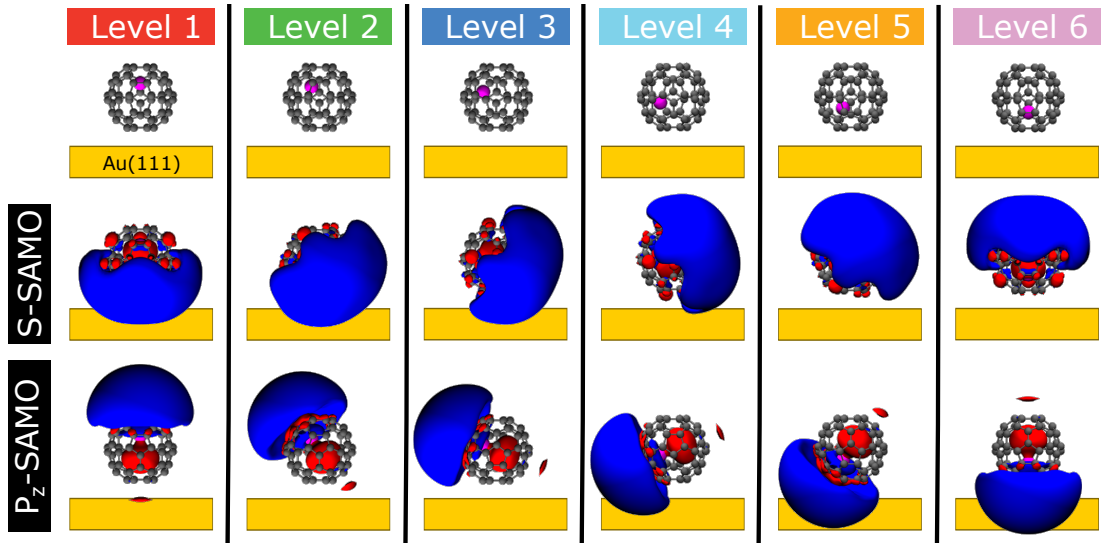

FIGURE 3.18: Graphic visualisation of how the electron densities of the S- and P_Z-SAMOs of Li@C_{60} will rotate with respect to the 6 different Li level orientations.

will change the amount of energy stabilisation which will be recorded in the resonance structure of the dI/dV spectra. In addition, the changed position of the Li atom should be possible to be visualised by recording STM topographic images at a bias corresponding to the energies of these SAMO resonances.

After having identified a Li-containing fullerene within a fullerene island which was deposited on a Au(111) surface, the STM tip was placed above it to achieve a selective manipulation. A tunnelling current was selected and the feedback loop was disengaged, allowing a constant tunnelling bias to be applied to the target molecule. The conditions that were usually used were +5.0 V and ~2.0 µA. Once these constant conditions were applied, the tunnelling current was recorded as a function of time, producing the I(t) graphs. Any abrupt changes in the current would indicate that a different molecular state is being accessed. Figure 3.19 (a) is an example of such a measurement. Once the

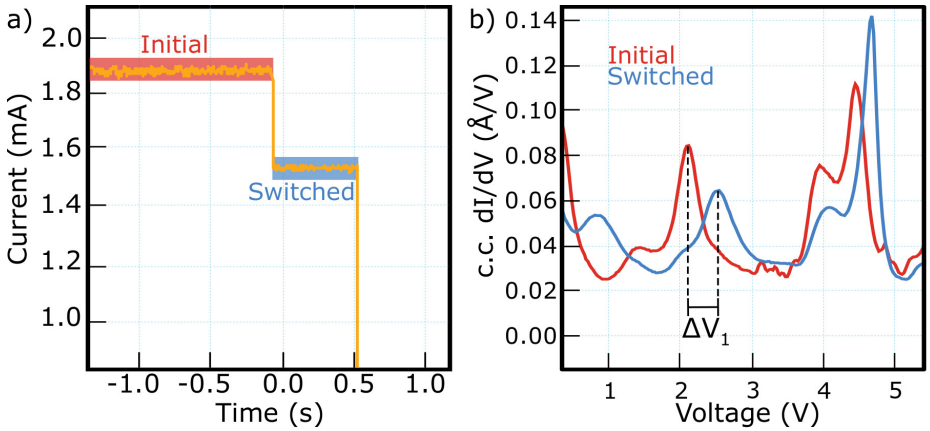

FIGURE 3.19: Inducing a switching event. (a) I(t) graph acquired with +5.0 V and 1.85 µA. A switched state is indicated by a sudden decrease in the current. (b) constant current dI/dV spectra of the initial (red trace) and switched (blue trace) states.

current changed, the excitation conditions were turned off and that molecular state remained constant (the new current value did not change). In order to understand this behaviour, STM images and dI/dV spectra were recorded before and after each event (in the figures these events are labelled initial and switched respectively. The initial state corresponds to a Li atom in a level 1 position.). The overall shape of the dI/dV spectra before and after the application of the excitation conditions, Figure 3.19 (b), are similar. This suggests that the target molecule maintains the Li@C_{60} structure. The blue trace however shows differences in the relative intensities and positions of some peaks. The S-SAMO experiences a +0.5 V shift (indicated by ΔV_1 in the figure). Changes below 1.5 V are observed but due to the superposition of the P_Z-SAMO and the LUMO+1 it is difficult to extract all the information at this point. Roughly no shifts are seen for the LUMOs. If the Li atom changed position during this excitation event, the above observations are to be expected since the SAMOs

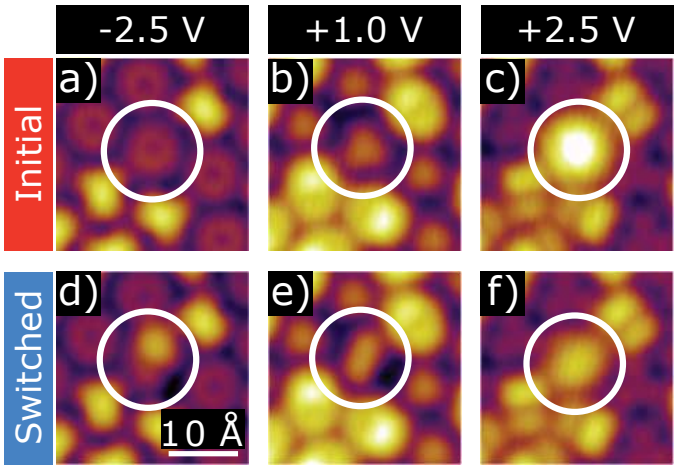

FIGURE 3.20: STM topographic images of the initial (top row) and switched (bottom row) states recorded at (a), (d) -2.5 V, (b), (e) +1.0 V and (c), (f) +2.5 V. These are the same states presented in Figure 3.19.

are influenced by the position of the Li atom while the LUMOs are centred on the carbon cage and any change in the position of the Li atom would not affect them greatly.

In Figure 3.20, the STM images corresponding to the initial and switched states in Figure 3.19 are presented. The STM images of the initial state have been presented briefly earlier and correspond to Li@C_{60} in a level 1 orientation; (a) a dark ring shape at -2.5 V; (b) a 3-fold symmetric bright shape at +1.0 V; and (c) a bright circular shape at +2.5 V. In the switched state the STM images show irregularities. (d) an asymmetric kidney bean shape at -2.5 V; (e) an oval shape with uniform height that is pointed in the same axis as the kidney bean at +1.0 V; and (f) an almost circular shape which has a reduced apparent height compared to (c) at +2.5 V. The data presented in Figures 3.19 and 3.20 can only be understood as a proof that the Li atom switched to a different position within the cage.

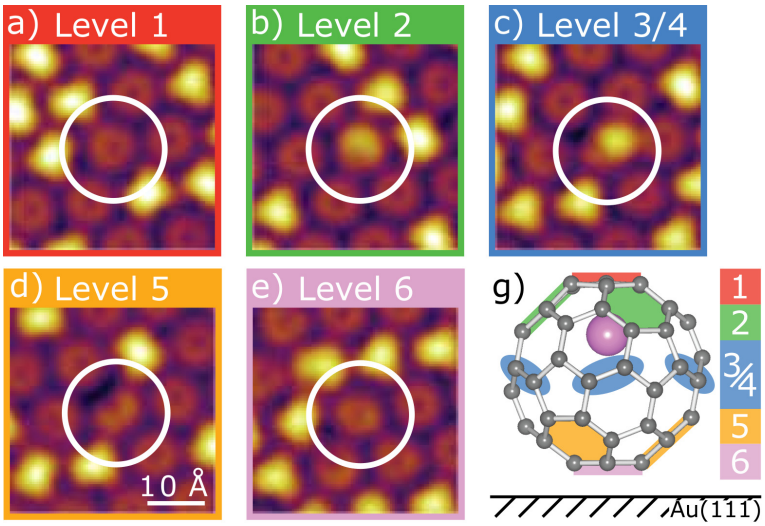

FIGURE 3.21: (a)-(e) STM topographic images of the 5 different species recorded at -2.5 V. (g) Updated assignment of the observed 5 different potential Li coordination levels.

From almost 300 different switching events, where each endohedral fullerene was only excited once, 14 distinct species which were divided into 5 different topographic groups were identified, Figures 3.21 (a)-(e). All these images were recorded at -2.5 V and can be described by either an off-centre bright protrusion or dark depression. Similar images were never seen when the excitation was directed to an empty C_{60} molecule. From a statistical analysis, the bright protrusion of (b) was found at 3 different orientations which were rotated by 120°. The dark depression of (d) was also found at 3 different orientations rotated by 120° and were also mirror-symmetric to the ones from (b). These correspond to the symmetry behaviours of the hexagonal faces between levels 2 and 5. The species in (c) was found at 6 different orientations rotated by 60°. Each direction was pointing in the middle of the expected directions from the hexagonal faces of levels 3 and 4. The above observation is interpreted as the Li atom moving into an equatorial position in front of the C=C double bond

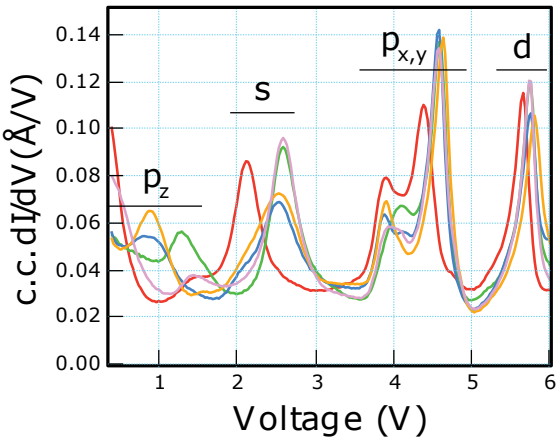

FIGURE 3.22: Constant current dI/dV spectra of the 5 different species presented in Figure 3.21.

that joins the 2 adjacent hexagonal faces of levels 3 and 4, thus being named level 3/4. The topography in (e) was found at only one orientation which was similar to the one in (a) but with having a lower apparent height. This was rationalised to correspond to level 6. The updated available Li levels are shown in (g) which satisfy the 14 distinct species having a ratio of 1:3:6:3:1.

The dI/dV spectra associated with the 5 different Li level positions are shown in Figure 3.22. As mentioned earlier, the exact position of the Li atom will influence the degree of hybridisation between the SAMOs and the d-orbitals of the metal substrate. Figure 3.23 shows a graphical representation of how the S-, P_Z and $P_{X/Y}$-SAMOs of Li@C_{60} will move in space. A close inspection of the dI/dV spectra reveals that the S-, $P_{X/Y}$- and D-SAMOs for all the switched states exhibit a blueshift in energy. Therefore a similar behaviour is to be expected for the P_Z-SAMO as well. This assumption allows us to identify that the peak ∼+1 V for the switched states corresponds to the P_Z-SAMO. Hence for level 1 the P_Z-SAMO is found at ∼+0.5 V. A similar trend in the energies

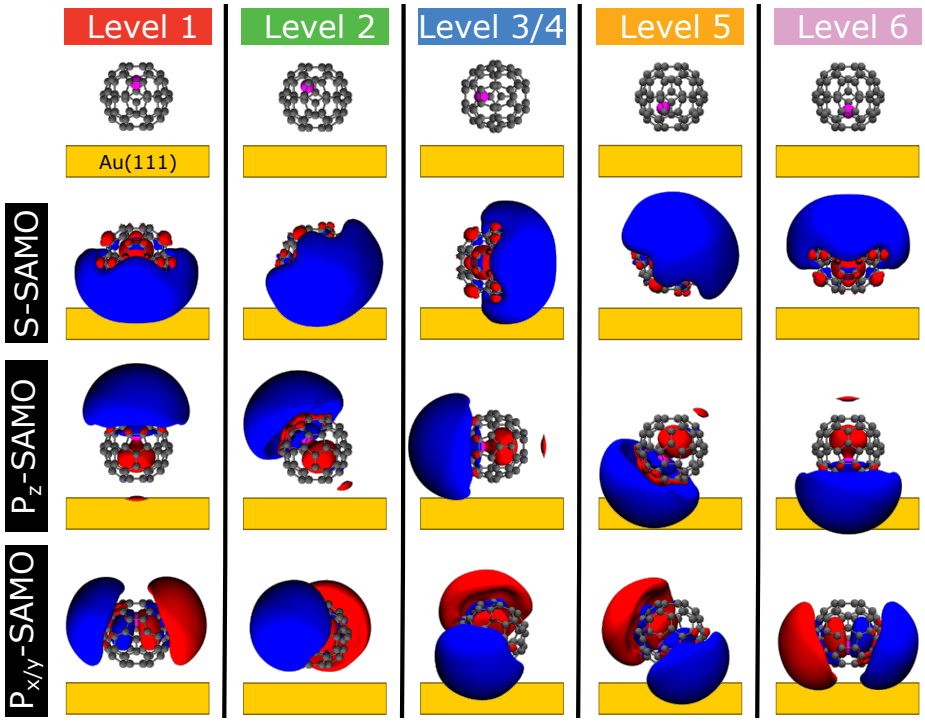

FIGURE 3.23: Graphic visualisation of how the electron densities of the S-, P_Z and $P_{X/Y}$-SAMOs of Li@C_{60} will rotate with respect to the 5 different Li level orientations.

of the SAMOs was found in the TD-DFT calculations and the gas-phase experiments. The S-SAMO of all the switched states has been shifted upwards by ~0.5 V. By viewing the DFT MOs, this behaviour is to be expected as by moving the Li atom from level 1 to 6, the overlap between the S-SAMO and the metal substrate is consistently reduced. On that note, one could suggest that the coupling between the S-SAMO and the metal d-orbitals affects the placement of the Li atom in the most energetically favourable coordination when a Li@C_{60} molecule is adsorbed on a metal substrate at low temperatures. The $P_{X/Y}$- and D-SAMOs are only slightly affected from the Li switching positions, indicating that these resonances couple only weakly to the metal substrate. This is shown

in the DFT representation where the electron density of the $P_{X/Y}$-SAMO is effectively parallel with the surface.

The two most common non-thermal activation methods that have been found in single-molecule switches are electric field (EF)[137–141] and inelastic electron tunnelling (IET).[131,142,143] Although both of these methods show similarities with the Li migration, EF switches depend on the bias and IET switches depend on the tunnelling current, they are not sufficient enough to explain the switching behaviour in Li@C_{60}. In EF switches, an opposite bias polarity is required to induce the reversible switching event. However, in Li@C_{60} reversible switching was observed with a constant polarity bias, hence this mechanism was ruled out. IET switches, on the other hand, are polarity independent and reversible switching takes place with either a positive or a negative bias. Since no switching event was induced using a negative bias, this mechanism was ruled out as well.

In the experimental investigation, it was found that for a switching event to take place an excitation condition of at least +3.0 V had to be applied, where the best results were found at +5.0 V. Since the S- and P_Z-SAMOs of a level 1 state, peaks located below +3.0 V, exhibit strong coupling with the metal d-orbitals, resonant tunnelling through them effectively removes the excitation electrons and disperses them very efficiently into the substrate. The $P_{X/Y}$-SAMOs however, which are found just before +5.0 V, show little coupling with the substrate. Thus the excitation electrons cannot be transferred as efficiently, resulting in a higher probability to induce coupling between the $P_{X/Y}$-SAMOs and the motional degrees of freedom of the Li atom.

The switching mechanism which is proposed is a new type of molecular switching mechanism which is based on resonant tunnelling through the $P_{X/Y}$-SAMOs to activate the Li atom migration. In resonant tunnelling, incident excitation electrons can couple to molecular states to induce molecular rearrangement. This mechanism has been presented in a theoretical investigation where the Li atom in a Au-Li@C_{60}-Au junction can switch between the opposite two ends of the junction.[144] Resonant tunnelling through the LUMO+X of C_{60} has been shown to result in heating followed by destruction of the cage.[88] This can be explained from the fact that LUMOs are centred on the carbon cage, thus resonantly exciting the LUMOs will likely lead to an efficient coupling with the vibrational degrees of freedom of the cage which in turn leads to cage heating and eventually to cage destruction. Since SAMOs are centred on the core of the cage, by resonantly exciting them there is a higher probability to interact with the Li atom. Overall, 14 reversible switching states were identified for Li@C_{60} molecules bound within an island of Li@C_{60} and C_{60} that was deposited on Au(111) surface. Up to date, this is the largest number of switching states that have been identified for a single-molecular switch.

4 Dependence of the ionisation of C_{60} on the laser conditions

4.1 Introduction

A series of measurements were performed to understand how the laser pulse duration, laser fluence and laser bandwidth affect the ionisation mechanism of C_{60} and the energy resolution of the SAMOs. For the broadband excitation, the SHG of the fundamental output was used where the pulse duration was varied by detuning the compressor inside the regenerative amplifier. For the narrowband excitation, the SHBC output was used. In both cases, the fluence was varied using a set of neutral density filters.

The results presented in this chapter show the preliminary tests of the two-colour fs-ps pump-probe setup which was briefly described in Chapter 2.1.4. The aim of this experiment is to investigate the fundamental electron dynamics and relaxation processes that occur when large molecules interact with ultrafast laser electric fields. Previous pump-probe experiments on C_{60}, where fs pulses were used on both beams, have not managed to achieve adequate energy and time resolution given that the photoionisation lifetimes of the SAMOs are comparable with those timescales and thus both pump and probe pulses

efficiently ionise the electrons.[40,43] In the planned experiment, a low intensity 800 nm fs broadband beam will be used to pump the system, taking care of using an intensity that does not efficiently ionise the electrons. Due to the incoherent population of the SAMOs when using fs pulses, a broadband pump beam will increase the probability of populating the SAMOs as it will result in a larger band of states to be initially populated.[35] An 800 nm beam was chosen as the pump beam given that 800 nm photons have a smaller photoionisation cross section than shorter wavelength photons. As a result, they are less efficient in climbing up the electronic ladder and inducing direct multiphoton ionisation.[28] Following this, the excited system will be probed with a 400 nm ps narrowband beam. Using this ionisation mechanism, an improvement from the current energy resolution of the SAMO states is hoped to be achieved.

Despite the fact that the actual pump-probe experiment was not performed due to time constraints, the setup was built and the individual beams, broadband and narrowband, were tested on C_{60}. In the following chapter, the results from the one-colour investigations will be presented (both beams were 400 nm for a more direct comparison).

4.2 Results and Discussion

4.2.1 Decay dynamics in C_{60}

The timescale of excitation and the laser intensity play an important role in which ionisation channel takes place for a photoexcited fullerene molecule.

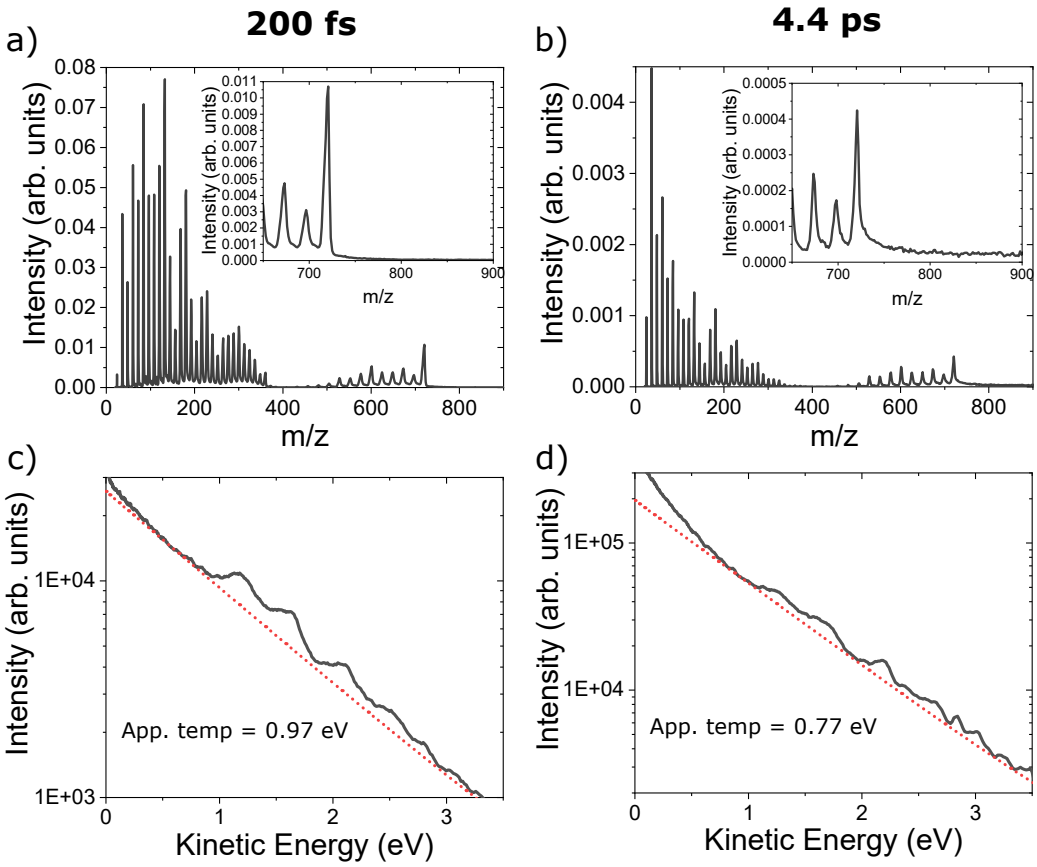

FIGURE 4.1: C_{60} mass spectra, (a) and (b), and PES spectra, (c) and (d), recorded using 200 fs and 4.4 ps respectively, while keeping the fluence constant at 0.26 Jcm^{-2}. All the data were acquired using 400 nm broadband (FWHM 3 nm) pulses. The PES in (c) and (d) are plotted in a semi-logarithmic scale and the red dotted lines are the fitted thermal background of the data.

Figure 4.1 shows typical mass spectra and PES spectra comparing the excitation in the fs (left hand side) and ps (right hand side) regimes. All the spectra were acquired using the same laser fluence, 0.26 Jcm^{-2}; meaning that the energy per pulse available to the system is the same. The time between photon absorption, however, affects the observed outcome. In the ps regime, the electronic energy that is applied to the system has time to be redistributed from

the electronic to the vibrational degrees of freedom.[17–19] As such, the apparent thermal electron emission temperature in the PES spectrum is lower than in the fs case. The molecules become vibrationally hot and start to fragment with subsequent C_2 emissions, forming smaller carbon cages (down to C_{30}), while if the supplied energy is high enough the cages are destroyed with subsequent C emissions forming carbon chains and carbon rings.[13] Delayed ionisation on the µs timescale is also observed on the mass spectrum, evident from the tail on the prompt ion peak. In addition, no multiple ionised species are observed. In the fs regime however, before the onset to delayed ionisation has been passed, the excitation energy is contained within the electronic degrees of freedom.[24–26] A larger apparent electron temperature is observed in the PES spectrum while multiple ionisation and no delayed tail is observed in the mass spectrum. In the following paragraphs, an investigation on the timescale for the onset to delayed ionisation using data either from the ion or the electron signals will be presented.

A series of spectra were acquired for varying laser fluences while keeping the pulse duration and laser bandwidth constant. Figure 4.2 shows the investigation using 525 fs broadband pulses. It can be seen that as the fluence increases, the apparent temperature of the emitted electrons increases as well (seen as a less steep slope in the semi-logarithmic plot).

The dependence of the apparent temperature with the fluence was scanned using different pulse durations. The results for a few pulse durations are shown in Figure 4.3. A linear trend was observed for the fluence range that was investigated. In addition, the fitted straight lines for all the pulse duration show a very similar y-axis intercept at 0.86 eV with a standard deviation of 0.04 eV.

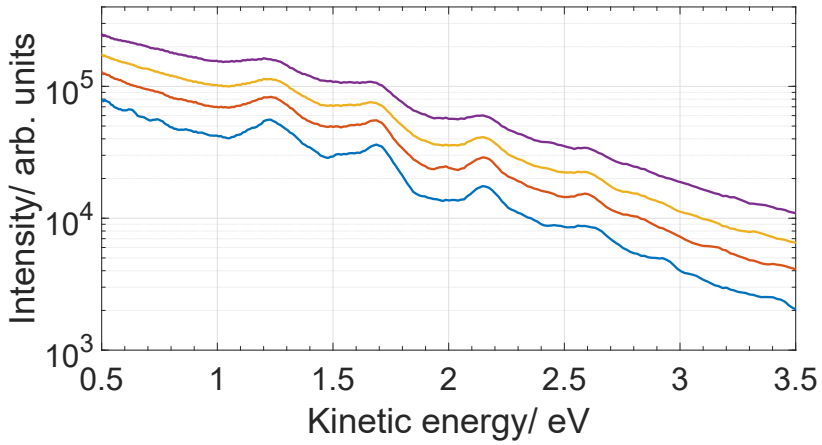

	Fluence/ Jcm^{-2}(±2%)	Intensity/ $TWcm^{-2}$(±2%)	App. temp/ eV (±0.02)
—	0.06	0.11	0.84
—	0.08	0.14	0.85
—	0.11	0.19	0.88
—	0.17	0.31	0.91

FIGURE 4.2: C_{60} AI-PES spectra plotted in a semi-logarithmic scale. Data acquired using 525 fs 400 nm broadband (FWHM 3 nm) pulses of varying laser fluence.

Such observations have also been reported when C_{60} was excited with 800 nm pulses.[24] However, direct comparison of the intercept values between data presented in this thesis and Hansen *et al*[24] is not feasible due to the fact that in that paper the asymmetry of the emitted photoelectrons with 800 nm was not yet known.[26] Their data correspond to the angle-integrated PES instead of taking into account only the apparent temperature from the perpendicular to the laser polarisation PES. Nevertheless, seeing similar observations, independent of the laser excitation energy fits with the model of the release of electrons being a statistical process independent of the laser excitation conditions.[22] The physical significance of the ordinate value could be related to the threshold of internal energy that is required in the system to induce statistical electron

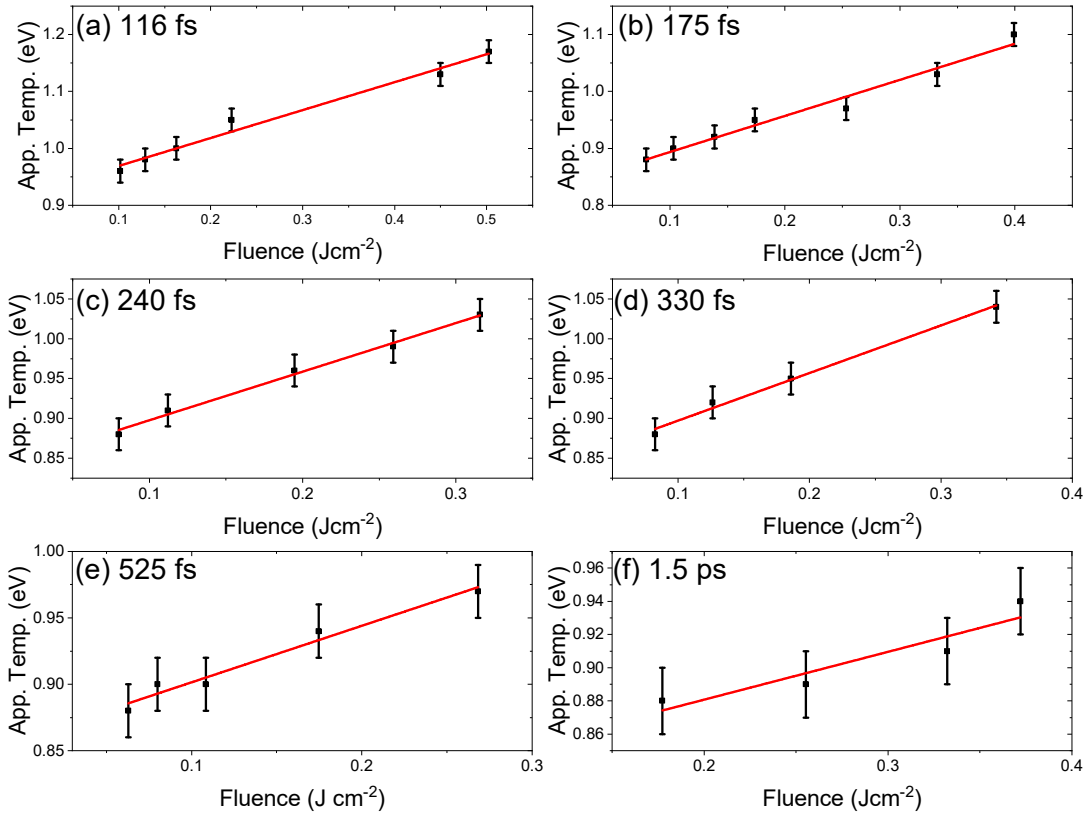

FIGURE 4.3: Dependence of the apparent temperature to the laser fluence for the cases of (a) 116 fs, (b) 175 fs, (c) 240 fs, (d) 330 fs, (e) 525 fs and (f) 1.5 ps. The red straight lines are the least squares fits to the data. Data acquired using 400 nm broadband (FWHM 3 nm) pulses.

emission. In other words, the lowest apparent electron temperature which can be recorded in an experiment, using the lowest possible laser fluence that results in detectable electron emission, should be related to the aforementioned threshold and it should be independent of the laser pulse duration.

In Figure 4.4, the gradients of the fits from the data in Figure 4.3 have been plotted against the pulse duration. The 800 nm values were taken from the literature and show remarkable similarities with the 400 nm data.[24] An initial

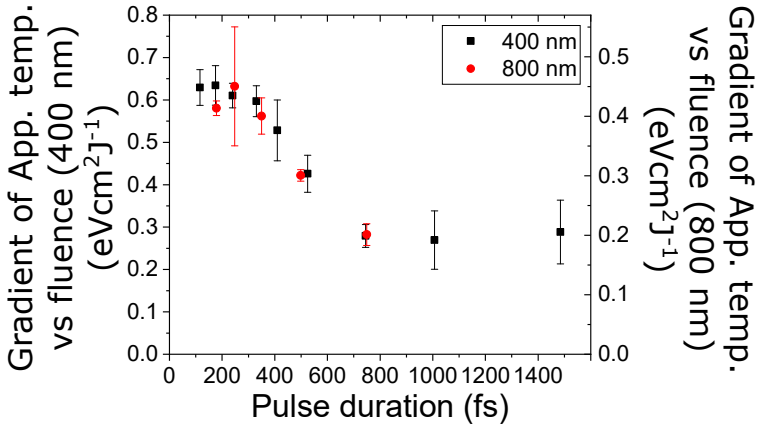

FIGURE 4.4: Gradient of the apparent temperature against the fluence (from Figure 4.3) plotted against the pulse duration. Data acquired using 400 nm broadband (FWHM 3 nm) pulses. The 800 nm values were adapted from Hansen *et al.*[24]

constant relationship is observed followed by a continuous quasi-linear decrease from 240 fs until 750 fs where a plateau is reached. The initial change at 240 fs indicates the time constant for the electronic energy to couple to the vibrational degrees of freedom. This value is in agreement with the literature values of 240-250 fs.[24,28,44] Once all, or a significant part, of the hot electron energy is equilibrated on the vibrational manifold, the values in Figure 4.4 should plateau, this is seen from 750 fs. As will become clearer after the analysis of the remaining results of this section, a time constant of 650-750 fs has been identified as the time required for a considerable amount of the electronic energy to be equilibrated on the vibrational degrees of freedom, after which the physical phenomena are dominated from having a vibrational excited system.

Figure 4.5 shows how the apparent temperature changes as a function of the pulse duration for two different laser fluences. As the pulse duration increases, the electronic energy has more time to couple during the pulse to the vibrations

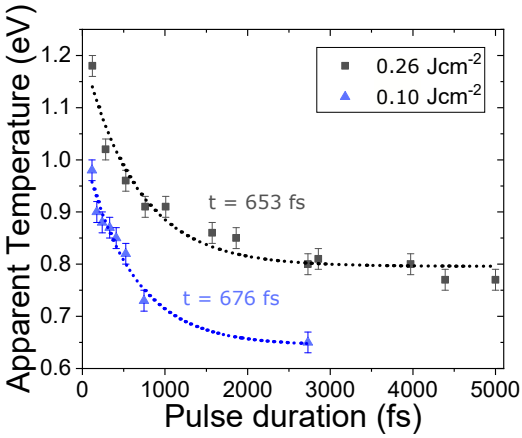

FIGURE 4.5: Apparent temperature as a function of the pulse duration for two different laser fluences, grey = 0.26 Jcm^{-2} and blue = 0.10 Jcm^{-2}. The dotted lines are the exponential best fit lines with time constant of 653 fs and 676 fs for 0.26 and 0.10 Jcm^{-2} respectively. Data were acquired using 400 nm broadband (FWHM 3 nm) pulses.

which leads to a lower effective electron temperature. The data exhibit an exponential behaviour that can be fitted with a time constant of 653 fs and 676 fs for the measurements with 0.26 and 0.10 Jcm^{-2} respectively. This time constant describes the interplay between the hot and the thermionic electron emissions and should not be confused with the vibronic coupling timescale. Thermionic emission becomes more significant with a higher fluence at the shorter pulse durations due to the competition between the two statistical emission mechanisms. A higher fluence allows for more ionisation channels to be available which results in a more efficient coupling within the system. Hence, an effectively faster slope is seen in Figure 4.5.

When exciting large molecules such as C_{60}, a large density of states is excited which result in a fast and efficient energy redistribution that populates a wide range of vibrational and electronic states.[17] To model such dynamics in an *ab*

initio way would prove very computationally expensive. Using a simple model based on statistical electron emission, Hansen *et al*[24] and Johansson *et al*[28] have quantitatively reproduced the experimental electron yields and apparent temperature trends in the PES of C_{60}. The model treats the valence electrons as a free-electron gas. Photons from a laser pulse are absorbed incoherently by the gas which results in an increase in the temperature of the system, followed by a suppression of the excited electronic energy by coupling to the vibrational manifold. The energy relaxation utilises a single decay constant. By incorporating the same model and without changing or adding any new parameters (using a vibronic coupling time of 240 fs), Figures 4.4 and 4.5 were qualitatively reproduced. These are shown respectively in Figures 4.6 (a) and (b).

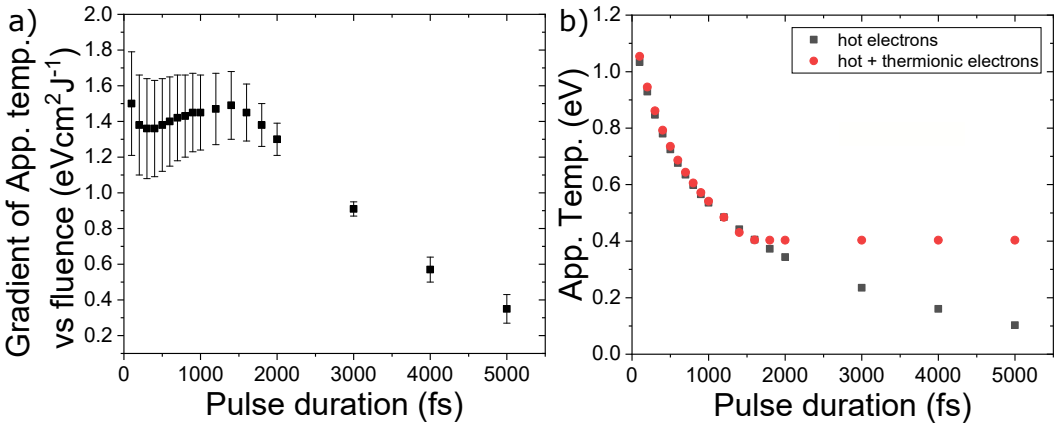

FIGURE 4.6: Calculations using the model as is described in,[28] using a 240 fs vibronic coupling constant. (a) Gradient of the apparent temperature against the laser fluence as a function of the pulse duration. (b) Trend in the apparent temperature as a function of the pulse duration for a laser fluence of 0.10 Jcm^{-2}. Red = modelling both hot and thermionic electrons and Grey = modelling only the hot electrons.

In Figure 4.6 (a), an initial constant gradient at short pulse durations is followed by a linear decrease, showing a similar trend to the experimental data

of Figure 4.4. Figure 4.6 (b) shows the difference in the trend of the apparent temperature as a function of pulse duration for a constant fluence (0.10 Jcm^{-2}) between: (i) when the thermionic electrons are accounted for (red) and (ii) when they are disregarded (grey) in the model. Given that an almost linear, continuous drop is seen at long timescales when only hot electrons are taken into account, the flattening out indicates that the signal is dominated by thermionic electrons. A similar exponential decay behaviour was reported earlier in Figure 4.5. The point of deviation between the two dataset in Figure 4.6 (b) is after the 1.4-1.6 ps mark. That is also the point after which the constant values in Figure 4.6 (a) start to decrease. In order to further investigate the above observations, the components of the total electron yield are plotted in a semi-logarithmic plot in Figure 4.7 for a range of different pulse durations around that value. Before 1.4 ps, the electron yield is dominated by hot electrons, while at 1.4 ps the hot electron and thermionic electron yields become comparable with each other, followed by a dominating thermionic electron yield for the longer pulse durations. Overall, even when using such a simplistic modelling approach, the qualitative agreement between the model and the experimental results is remarkable.

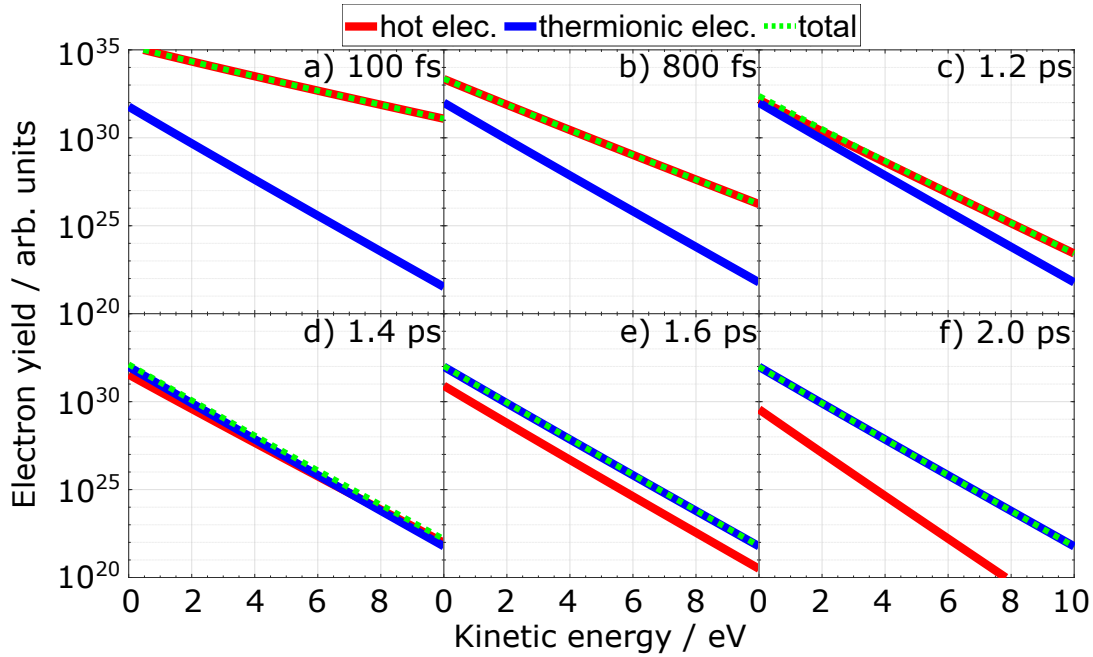

FIGURE 4.7: Calculations using the model as is described in,[28] using a 240 fs vibronic coupling constant. Breakdown of the components of the electron yield for various pulse durations. (a) 100 fs, (b) 800 fs, (c) 1.2 ps, (d) 1.4 ps, (e) 1.6 ps and (f) 2.0 ps. Solid red line = hot electron yield, solid blue line = thermionic electron yield and dashed green line = total electron yield = hot + thermionic electron yields.

The onset of delayed ionisation was also investigated using mass spectroscopic analysis. As was described by Hansen and Echt, by assuming that the internal energy distribution is flat, the intensity of the delayed ionisation tail of the prompt C_{60}^{+} peak follows a power law. This results in a linear behaviour when the time of flight data are plotted in a double logarithmic plot.[145] In their experiments using 266, 355 and 532 nm ns pulses, the power law was valid between the time range of 0.1 to 10 µs after the prompt peak. This power law is given by,

$$I(t) = I_0 t^{-p}, \tag{4.1}$$

where $I(t)$ is the intensity at time t and p is the exponent which is approximately equal to the ratio of the ionisation potential of C_{60} over the activation barrier for C_2 emission from the neutral molecule.[145] The graphs in Figure 4.8 show the mass spectra in double logarithmic plots for a range of pulse durations, where the fluence was kept constant, as a function of the ion arrival time where the C_{60}^+ peak has been set to t = 0 s. (a) shows the data for up to 30 µs while (b) shows a close up, up to 2 µs. The most interesting feature is that the delayed ionisation tail in (a) does not seem to follow the linearity of the power law that would be expected for times up to 10 µs.[146] Instead, after an initial linear trend there seems to be a discontinuity in the slope which can be described by a plateau between 2-8 µs, followed by a sudden change in slope at around 8-10 µs. This unexpected feature which is present in all the pulse durations will become more apparent and will be subject to further investigations in Chapter 4.2.3.

In (b), the data for 732 fs up to 5 ps pulse durations follow a linear behaviour that can be fitted by the power law (solid lines). Initially it was assumed that the deviation from the power law fit at the shorter pulse durations was a result of a greater relative isotope contribution in the spectra. Only the C_{60} isotopes that had either 1 or 2 ^{13}C were considered, since the intensity of the heavier isotopes would be well below the noise level. These isotopes should respectively arrive at 0.03 and 0.06 µs after the C_{60}^+ peak. Given that the analysis starts from 1 µs, the isotope argument could not describe the observed trends. As it

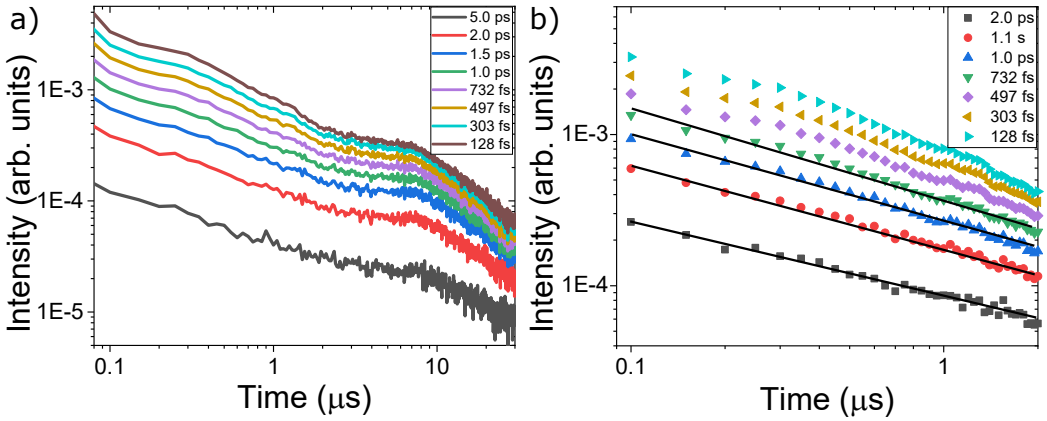

FIGURE 4.8: C_{60} mass spectra acquired using different pulse durations plotted in a double logarithmic scale as a function of the ion arrival time. The C_{60}^{+} peak has been set to t = 0 s. All the spectra were recorded using the same fluence, 0.26 Jcm^{-2}. (a) displays the data for up to 30 μs and (b) for up to 2 μs. In (b) the solid lines correspond to the fitted power law. Data were acquired using 400 nm broadband (FWHM 3 nm) pulses.

was described in the previous paragraphs, it is only after about 750 fs that a considerable amount of excitation energy has been redistributed into the vibrational manifold, which results in a stronger contribution from thermionic emission (seen earlier) and also would result in a greater contribution from delayed ionisation. Therefore, the deviation from the power law at the short pulses durations in Figure 4.8 (b) can be explained from the point of view that there is less contributions from delayed ionisation as most of the electronic excitation has not had enough time to redistribute. Similar observations have also been reported in literature.[147]

Figure 4.9 displays the relative intensities between the smaller fullerene fragments as a ratio of C_{x+2}^{+}:C_{x}^{+} which is plotted against the pulse duration, while the fluence in all the measurements was kept constant. After the transition

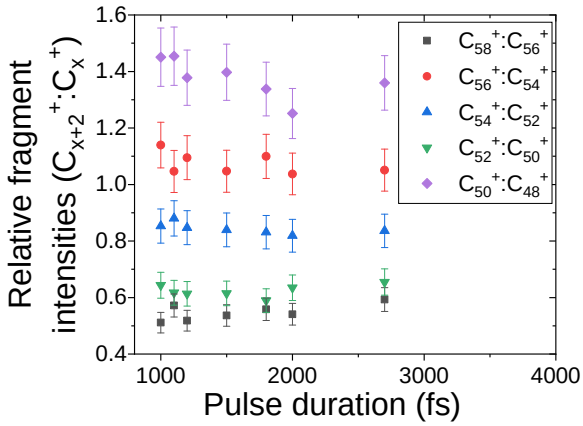

FIGURE 4.9: Relative fullerene fragment intensities of the form C_{x+2}^+:C_x^+, derived by the mass spectra of C_{60} that were acquired using different pulse durations while keeping the fluence constant at 0.26 Jcm^{-2}. Grey square: C_{58}^+:C_{56}^+, red circle: C_{56}^+:C_{54}^+, blue triangle: C_{54}^+:C_{53}^+, green triangle: C_{52}^+:C_{50}^+ and purple diamond: C_{50}^+:C_{48}^+. Data were acquired using 400 nm broadband (FWHM 3 nm) pulses.

to delayed ionisation the ratios stay roughly the same throughout the measurement series. This indicates that the production of the prompt fragments is independent of the excitation timescale, but rather dependent on the total energy of the pulse, the fluence. These observations are also independent of the laser excitation energy, since similar conclusions were observed with 790 nm photons.[147]

While keeping the fluence constant, the intensity of the delayed tail in the mass spectra was investigated over a range of pulse durations. Figure 4.10 (a) shows that the intensity of the delayed tail has a linear relationship, passing through the origin, as a function of the pulse duration. By referring back to the observations from Figure 4.4, where it was found that from 750 fs pulse durations the gradient of the apparent temperature against the fluence is constant, this

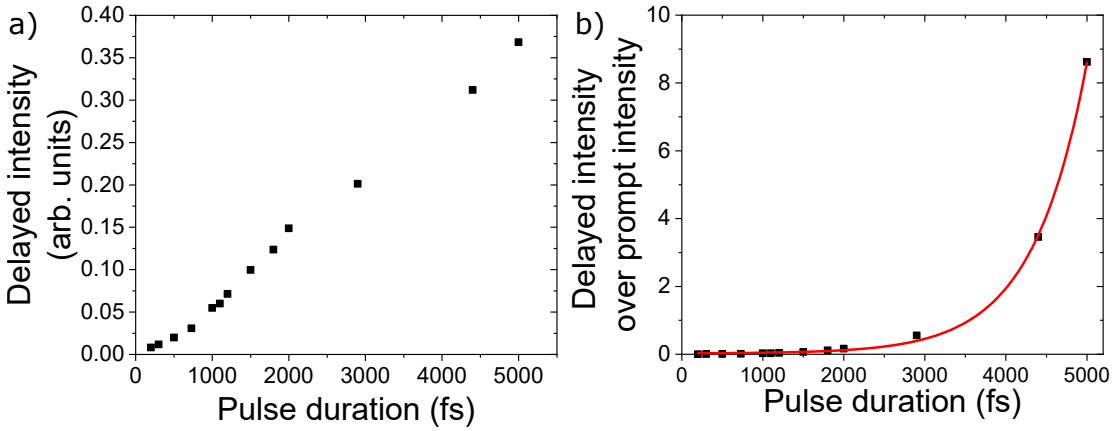

FIGURE 4.10: (a) Intensity of the delayed ionisation tail as a function of the pulse duration taken at a constant fluence of 0.26 Jcm^{-2}. (b) The ratio of the delayed ionisation tail over the prompt ionisation intensity as a function of the pulse duration taken at a constant fluence of 0.26 Jcm^{-2}. The red line is the fitted exponential function with a time constant of 668 fs. Data were acquired using 400 nm broadband (FWHM 3 nm) pulses.

means that the observed electronic energy past the 750 fs mark remains constant. In addition to this, as the pulse duration increases, there is more time for more energy to be coupled to the vibrations, which thus leads to the increased delayed tail in Figure 4.10 (a). In (b) the ratio of the delayed intensity over the intensity of the prompt peaks is presented as a function of the pulse duration. An exponential behaviour is observed with a fitted time constant of 668 fs. This is a very similar value to the time constant that was extracted from the photoelectron spectra that were taken using the same laser fluence in Figure 4.5.

It should be pointed out that the mass spectra have not been corrected for the detection efficiency of the channel plates - the detection propability decreases for larger mass ions due to the reduced secondary electron production at the

channel plates. For singly charged carbon clusters it has been shown that the detection efficiency increases exponentially with the ion velocity.[148,149] Given that all the spectra were taken with the same acceleration field, the correction should not influence the rise time of the data, hence a similar time constant should be extracted.

4.2.2 SAMO

In the following section, the effects of the laser conditions on the excitation and energy resolution of the SAMOs will be investigated. In a series of measurements, the pulse duration was varied while the bandwidth (broadband FWHM 3 nm) of the pulse and the laser fluence (0.26 Jcm^{-2}) were kept constant. The results showed that the central kinetic energy of the SAMOs varied linearly with pulse duration, and with the same rate between the different SAMOs, see Figure 4.11. Given that the bandwidth is constant, there is no reason to expect such a trend. However, this could be explained from the fact that in order to produce pulses longer than 120 fs, a blueshift chirp was introduced. With such a chirp, the arrival time of the photons is stretched in time, where the red photons arrive before the blue photons. The results show a blueshift in the central energies of the SAMOs which suggest that the SAMOs are ionised at the later part of the laser pulse.

From a SAMO peak fitting investigation where the quality of the fit was tested using either Lorentzian or Gaussian distributions, it was concluded that inhomogeneous broadening was present when chirped pulses were used. Figure 4.12 shows the comparison of the fitting between 282 fs and 1 ps broadband pulses. For the shorter pulse duration, both (a) Lorentzian and (b) Gaussian

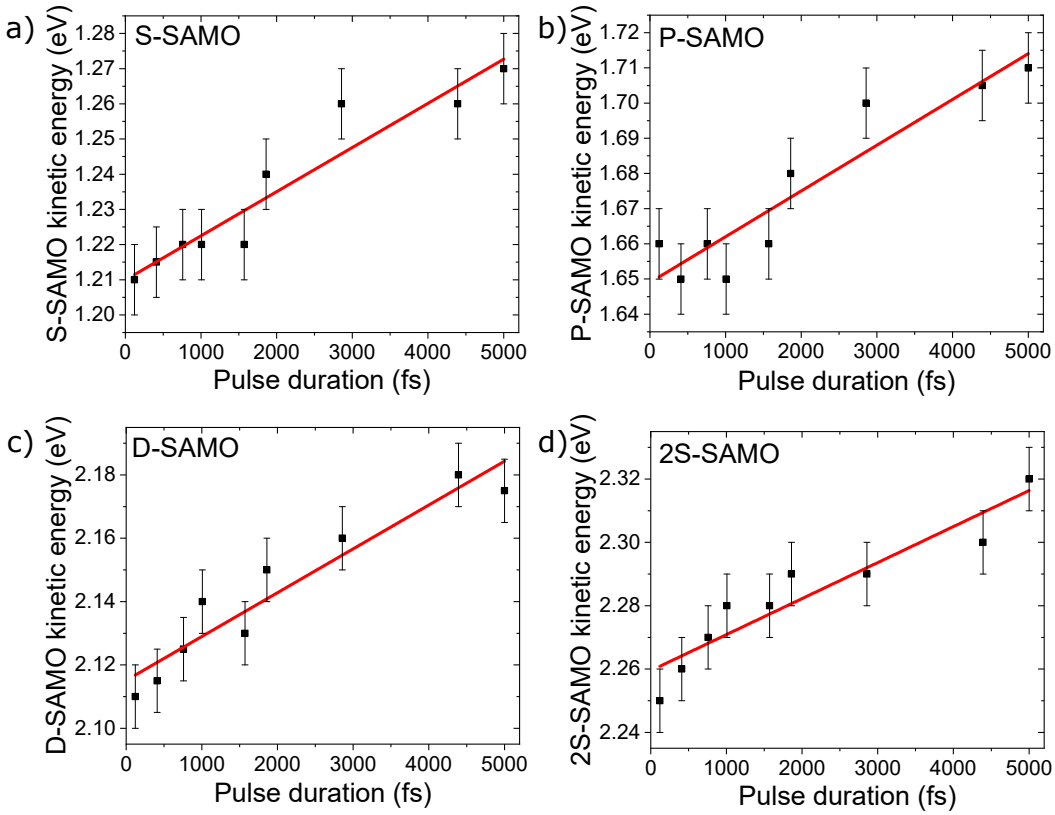

FIGURE 4.11: C_{60} SAMO kinetic energy as a function of the pulse duration, taken at a constant fluence of 0.26 Jcm^{-2}. (a) S-SAMO, (b) P-SAMO, (c) D-SAMO and (d) 2S-SAMO. The red straight lines are the least squares fits to the data. The average slope is 1.27×10^{-5} with a standard deviation of 0.09×10^{-5}. Data were acquired using 400 nm broadband (FWHM 3 nm) pulses.

distributions could fit well the experimental PES. Given that with short pulses Lorentzian functions can reproduce the data, the peak widths can be considered to be closer to the natural linewidth. However, from 1 ps pulses and longer, only (d) Gaussian distributions could acceptably fit the data. With Lorentzian, (c), the shoulders between the P- and D-SAMOs were always exaggerated (arrow in the figure). The fact that Lorentzian functions could not,

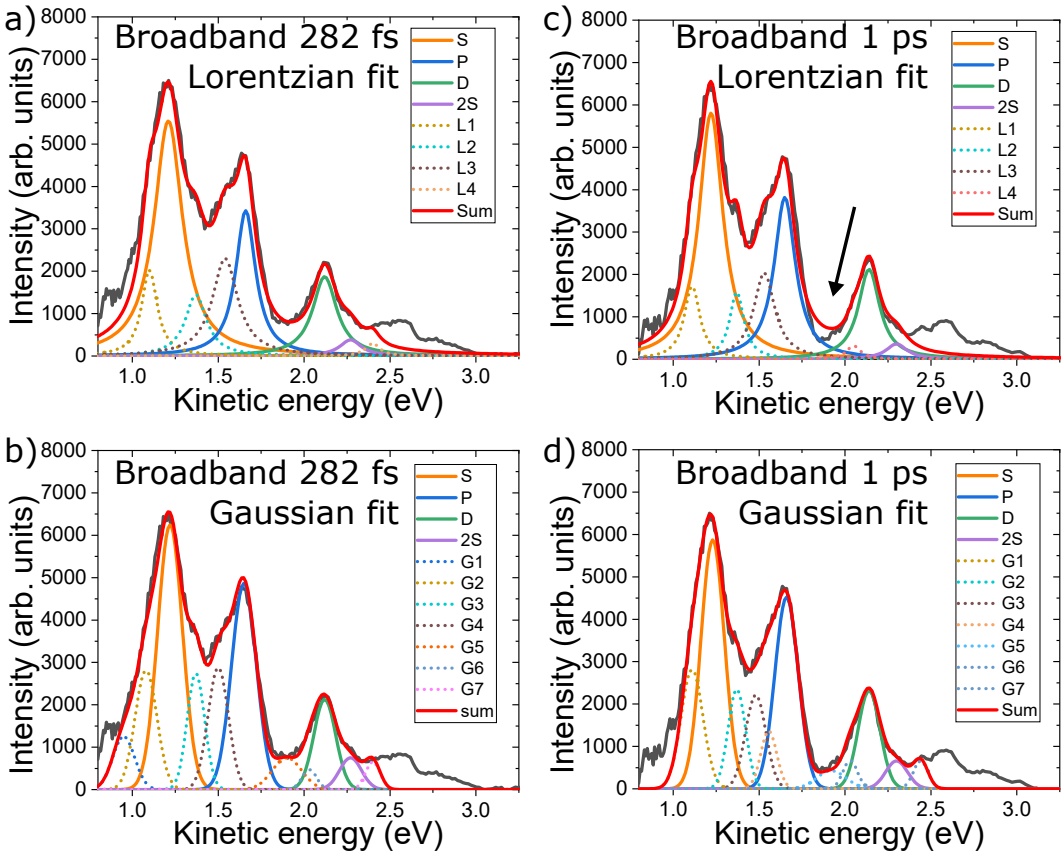

FIGURE 4.12: C_{60} AI-PES, after subtraction of the thermal background, acquired using (a)-(b) 282 fs and (c)-(d) 1 ps 400 nm broadband (FWHM 3 nm) pulses. In (a) and (c) the peak fitting uses Lorentzian functions, while in (b) and (d) Gaussian functions. The arrow in (c) indicates the point where the Lorentzian functions overestimate the intensity.

but Gaussian could reproduce the experimental PES suggests that inhomogeneous broadening is present in these datasets. The above results indicate that when the chirp is not as extreme, the natural linewidth becomes comparable to measured peak widths. This means that in order to yield information on the lifetime of the SAMO states from the peak widths, the excitation energy must be chirp-free.

The effect of using a different bandwidth of excitation was investigated by performing a similar comparison, as described in the previous paragraph, between the broadband 5 ps and the narrowband 4±1 ps pulses. Because the two beams were focused into the interaction chamber using different optical components (Figure 2.12), direct comparison of the fluences was not feasible. Therefore experiments were performed with fluences that achieved similar fragmentation patterns in the mass spectra, Figures 4.15 (a) and (e). The thermally subtracted AI-PES using the broadband and narrowband excitations are displayed in Figure 4.13 (a)-(b) and (c)-(d) respectively. In (a) and (c) the fitting was performed using Lorentzian functions while in (b) and (d) with Gaussian functions. For both sets of data, Gaussian functions seemed to afford the better fit since Lorentzian functions exaggerated the intensity of the shoulders between the P- and D-SAMOs. This would indicate, using the conclusion from the previous discussion, that the SHBC beam is not chirp-free and inhomogeneous broadening is taking place. A closer look at the SHBC spectrum, Figure 2.5 (b), indeed validates this assumption. The optical spectrum deviates from a perfectly Gaussian shape by having a faint shoulder on the left hand side. Given that the SHBC beam is produced by inducing and cancelling out two opposite chirped pulses, if the subtraction is not perfectly optimised, a leftover chirp will be present in the output beam and the result would affect the optical spectrum in such a manner.[150] Moreover, from the peak fitting analysis, all SAMOs of both measurements from Figure 4.13 had the same peak width value. This would suggest that a better energy resolution was not achieved when narrowband excitation was used. This is contradictory to the initial assumption when the fs-ps pump-probe experiment was set up.

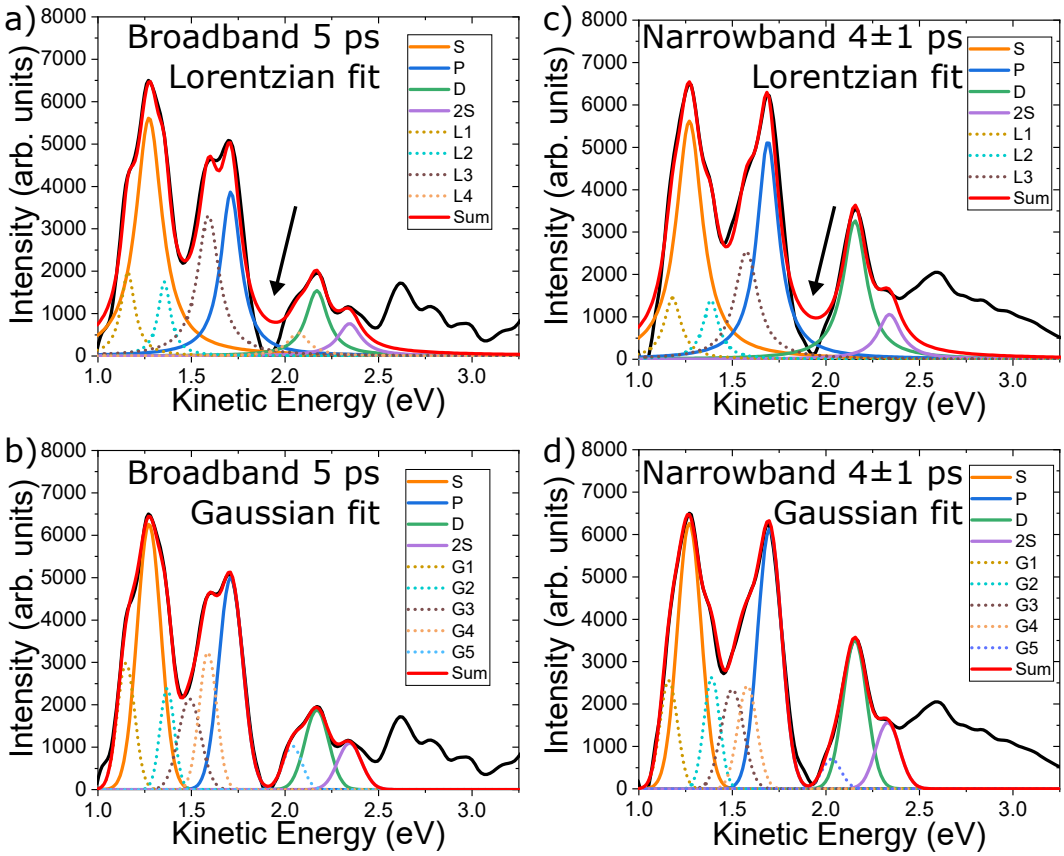

FIGURE 4.13: C_{60} AI-PES, after subtraction of the thermal background, acquired using 400 nm (a)-(b) 5 ps broadband pulses (FWHM 3nm) with a fluence of 0.25 Jcm^{-2} and (c)-(d) 4±1 ps narrowband pulses (FWHM 0.09 nm) with a fluence of 0.55 Jcm^{-2}. In (a) and (c) the peak fitting uses Lorentzian functions, while in (b) and (d) Gaussian functions. The arrows in (a) and (c) indicates the point where the Lorentzian functions overestimate the intensity.

However, it should be pointed out that the peak widths were not determined by the natural lifetime of the states. So these results neither disprove nor validate the assumption and further investigations using genuine narrowband ps chirp-free pulses should be performed to obtain more conclusive results.

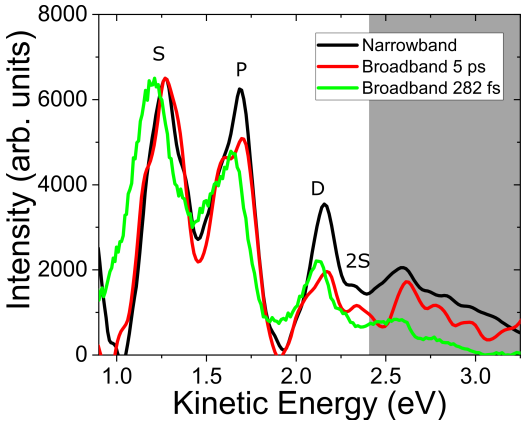

FIGURE 4.14: C_{60} AI-PES, after subtraction of the thermal background, acquired using narrowband 4±1 ps (black), broadband 5 ps (red) and broadband 282 fs (green) 400 nm pulses. The S-SAMO intensity has been normalised between all the spectra.

Figure 4.14 displays the comparison of the thermal background subtracted AI-PES recorded using narrowband (black), broadband 5 ps (red) and broadband 282 fs (green) excitation (all 400 nm). The following discussion will be focused on the high kinetic energy part of the spectra which has been shaded, from about 2.5-3.5 eV. All the spectra have been normalised so that the S-SAMO intensity is identical. Given that 3.1 eV corresponds to the photon energy, the higher intensity around that region would suggest that long-lived, high-lying Rydberg states are responsible for those features in the PES. The data therefore suggest that high-lying states are more easily populated with narrowband pulses. Given that there is less efficient intermediate coupling when using narrowband excitation, the likelihood of getting higher up the electronic ladder and populating high-lying Rydberg states is greater, hence a higher ionisation intensity from these states would be expected.

4.2.3 Long-lived state investigation

In this section, the effect that using narrowband pulses will have on the excitation mechanism and the energy redistribution in C_{60} will be investigated. Figures 4.15 (a), (b) and (c), (d) show respectively the high and low intensity fragmentation mass spectra and PES taken with the narrowband pulses, while (e) and (f) show respectively the mass spectrum and PES taken with the 5 ps broadband pulses. Due to the fact that the two laser beams, narrowband and broadband, are focused using different optics, the focal spot sizes are different, see Chapter 2. Therefore direct comparison of the PES and mass spectra using the same fluence is not possible. Hence, the comparison was made with fluences that result in similar fragmentation patterns in the mass spectra. In Figure 4.15, the characteristic delayed ionisation tail is evident in all the mass spectra, however the intensity of the tail is greater when ionising with narrowband pulses than with broadband. This is the case even when the laser fluence used is not enough to induce extensive fragmentation, (c). This observation indicates that more energy has been redistributed to the vibrational manifold when using narrowband pulses. Moreover, when comparing the PES (b) and (f), the apparent electron temperature is smaller in the narrowband data. This means that overall, there is a larger amount of energy in the electronic levels of the molecules for the broadband case. Thus it was concluded that: (i) when using narrowband excitation, there is a less efficient energy redistribution within the electronic manifold, seen as the lower apparent temperature in the PES and (ii) as such, and having passed the onset to delayed ionsation, more energy is stored in the vibrational manifold. This is seen in the more prominent delayed tail in the mass spectra.

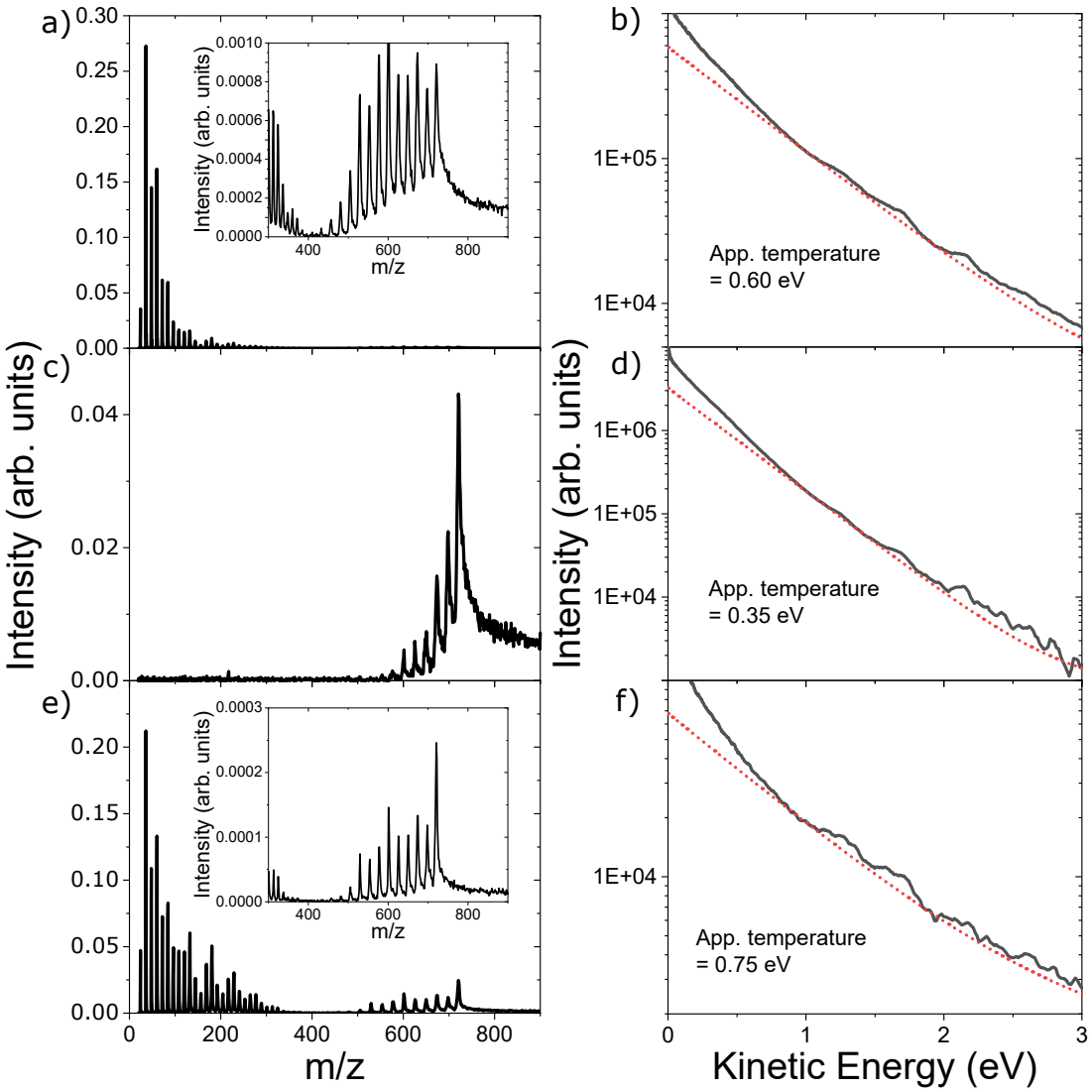

FIGURE 4.15: 400 nm C_{60} mass spectra, (a), (c), (e) and AI-PES spectra, (b), (d), (f). (a)-(b) were recorded using 4±1 ps narrowband pulses with a fluence of 0.55 Jcm^{-2} and an intensity of 0.13 TWcm^{-2}. (c)-(d) were recorded using 4±1 ps narrowband pulses with a fluence of 0.19 Jcm^{-2} and an intensity of 0.05 TWcm^{-2}. (e)-(f) were recorded using 5 ps broadband pulses with a fluence of 0.25 Jcm^{-2} and an intensity of 0.05 TWcm^{-2}. The PES in (b), (d), (f) are plotted in a semi-logarithmic scale and the red dotted lines are the fitted thermal backgrounds.

The delayed ionisation tail was investigated further. To do this, mass spectra were recorded for a few tens of µs after the C_{60}^+ prompt peak. Figure 4.16 (a) shows the mass spectrum where all the fragments apart from C^+ can be seen, while Figure 4.16 (b) has been taken at the same fluence and portrays a longer acquisition of the tail. There appears to be a peak superimposed on the delayed tail. In the following discussion, this peak shall be referred to as the 'bump in the tail'. This peak is really broad and starts to appear at around 6 µs after

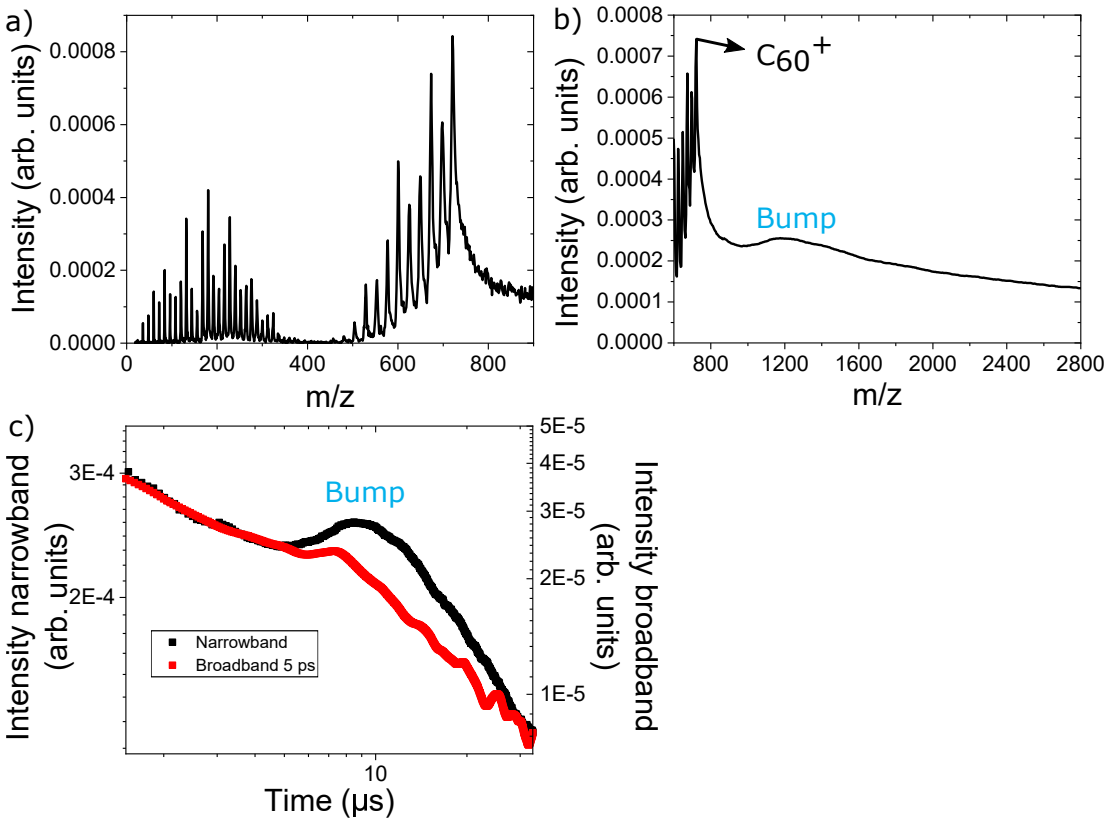

FIGURE 4.16: 400 nm C_{60} mass spectra recorded using 4±1 ps narrowband pulses with a fluence of 0.39 Jcm^{-2} and an intensity of 0.09 $TWcm^{-2}$. (a) and (b) are plotted in a double linear scale. In (a) the C^+ is not seen. (c) is a double logarithmic plot of the data in (b), black trace, having the C_{60}^+ peak set to t = 0 sec. The data from the broadband 5 ps are plotted as well in the red trace.

the C_{60}^+ peak, Figure 4.16 (c) black. It should be noted that an unusual breakage in the linearity of the slope in the log-log plots was also seen at a similar time after the C_{60}^+ peak for the case of the broadband excitation for all the pulse durations that were investigated, Figure 4.8 (a). In Figure 4.16 (c), the broadband 5 ps data are plotted next to the narrowband data to aid with the above comparison. However, in the broadband cases the bump is not as pronounced. Seeing this abrupt change of slope around 6 µs in both broadband and narrowband measurements, and not having seen it before in the literature, when extensive work has been done using 266,[123,151] 330,[152] 337,[146] 790[147] nm pulses, points to the direction that the population of the state that is responsible for the bump could be wavelength dependent and would thus only become resonant with the multiphoton ionisation of 400 nm. To further investigate this speculation, measurements using narrowband excitation of different wavelengths is suggested.

In order to isolate and investigate the bump peak, the intensity of the delayed tail had to be subtracted from the mass spectrum data. This is shown in Figure 4.17 (a) where the power law behaviour, that was mentioned earlier in the chapter, is fitted to the data, shown by the red dotted line. The intensity of the bump is shown by the shaded area. (b) shows the result of subtracting the power law from the data in (a). An exponentially modified Gaussian distribution, green dotted line, was fitted in (b) to identify the peak. A series of mass spectra using different laser intensities is shown in (c). An identical procedure as was described in (a) and (b) was performed for all the different laser intensity mass spectra, and the results from the peak fitting yielded a mean time of 6.9 µs with a standard deviation of 0.1 µs, displayed in (d).

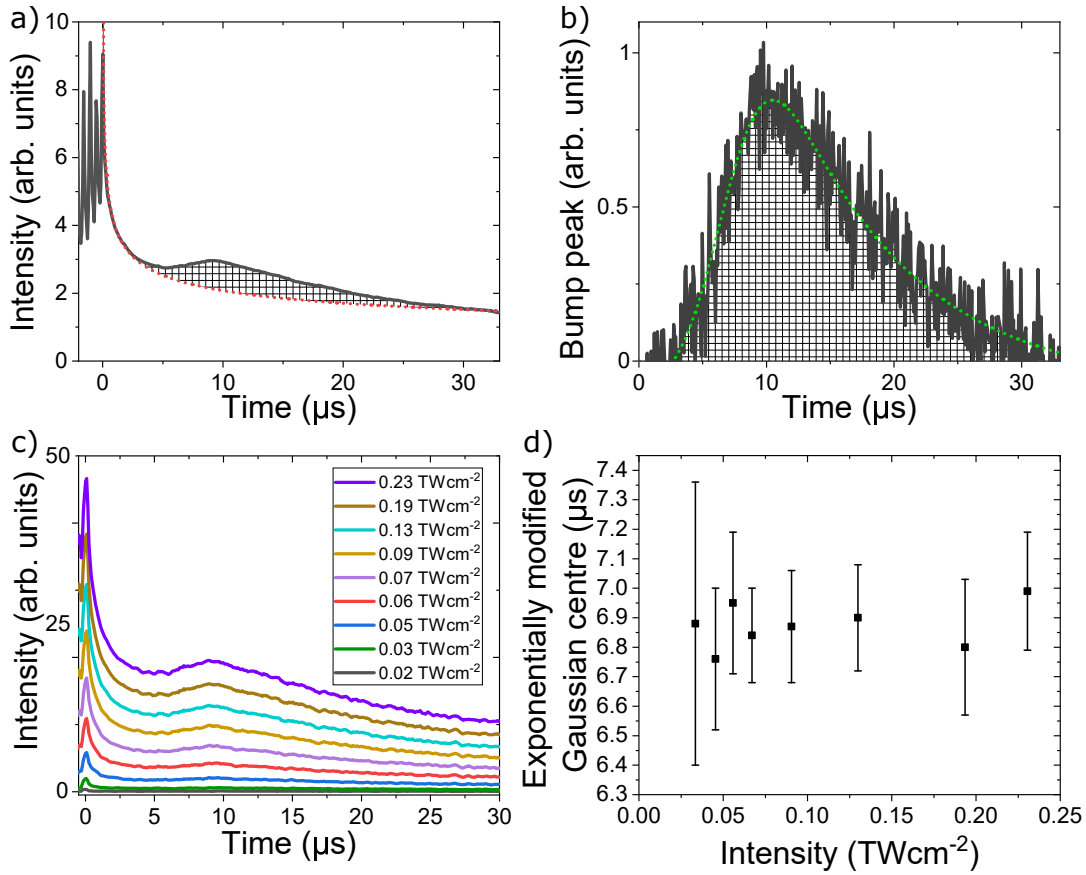

FIGURE 4.17: Further investigation of the bump in the mass spectra delayed tail. (a) C_{60} mass spectrum as a function of the ion arrival time where the C_{60}^+ peak set to t = 0 sec, recorded using an intensity of 0.09 $TWcm^{-2}$. The red dotted line is the fitted power law to the delayed tail. (b) Intensity of the bump peak in (a) after the subtraction of the fitted power law from the data. The area has been shaded in both figures for simplicity. The green dotted line is the fitted exponentially modified Gaussian function. (c) A series of mass spectra using different laser intensities. (d) The centre of the fitted Gaussian peak as a function of the laser excitation intensity from the data in (c). All mass spectra were taken using 400 nm, 4±1 ps narrowband pulses.

The dependence of the fitted peak width with the laser intensity is plotted in Figure 4.18. The linearly increasing relationship suggests that the bump is unlikely to be an artefact of some unknown large mass or group of masses as

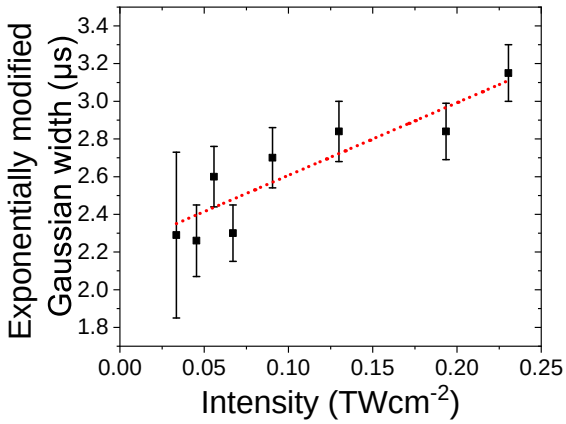

FIGURE 4.18: The fitted peak width of the exponentially modified Gaussian distribution as a function of the laser intensity. Data from the mass spectra of Figure 4.17 (c).

the width and central position would be expected to decrease with a higher laser intensity.

Then, what could the origin of the bump be? In the remainder of this section, two hypothesis will be presented. Firstly, the arguments for, and eventually, against a slow decaying C_{60} triplet state will be investigated. Followed by the hypothesis that a slow decaying superexcited state or slow decaying high-lying excited states in C_{60} may be responsible.

The argument that a decaying C_{60} triplet state is the origin of the bump is as follows. When the 5 ps broadband excitation was used, a large band of high energy states can be populated with the initial multiphoton absorption, schematically shown on the left of Figure 4.19. Energy is efficiently accumulated on the electronic subsystem, while less energy has been redistributed on the vibrational subsystem. These are seen as the higher apparent electron temperature in the PES and the lower intensity of the delayed tail in the mass

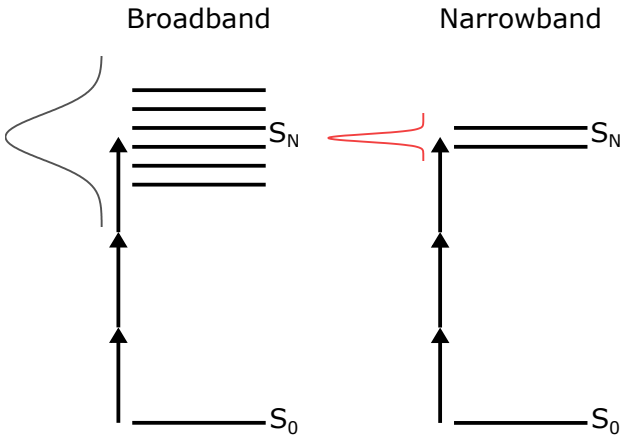

FIGURE 4.19: Schematic diagram showing the difference between the number of states that are populated when broadband or narrowband excitation is used.

spectra respectively, as discussed for Figure 4.15. When narrowband excitation was used, a smaller band of high energy states could be populated, right hand side of Figure 4.19. With fewer states being populated, the electronic energy redistribution processes will be less efficient, seen as the lower apparent electron temperature in the PES. Hence, there is less hot electron emission and the excitation energy is accumulated on the vibrational subsystem, seen as the higher intensity delayed ionisation tail in the mass spectra of Figure 4.15. The energy may accumulate as predominantly vibrational excitation within the triplet manifold and could then be "freed-up" on a longer timescale when the system decays back to the ground singlet state.

When molecules are heated up, they gain vibrational energy.[153,154] For an oven temperature of 723-773 K, the average thermal vibrational energy in the C_{60} molecules which is acquired from the source is determined to be 3.91-4.45 eV.[153] As can be seen from Figure 4.20, the lifetime of the C_{60} triplet state depends exponentially on the internal vibrational energy of the molecules.[155]

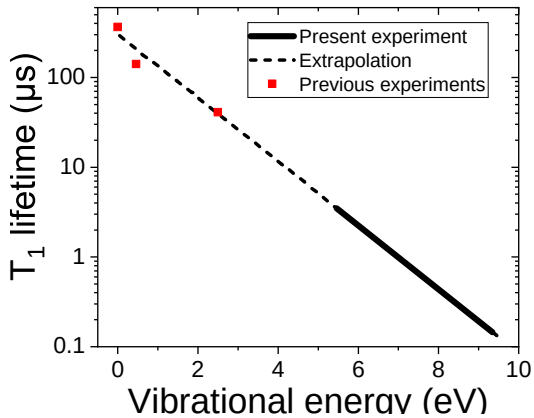

FIGURE 4.20: C_{60} triplet state lifetime as a function of the internal vibrational energy of the molecules, plotted in a semi-logarithmic scale to show the exponential relation. Figure adapted from Etheridge *et al.*[155]

From the above calculated values, the lifetime of the triplet state would have a range of 8.1-12.6 µs. However, one should point out that this lifetime range would be true only for molecules that have just come out of a hot oven. Once molecules have interacted with a laser pulse, they are expected to have acquired additional internal energy due to the photon absorptions. From Figure 1.2 it can be deduced that the lowest possible internal energy that is required for thermionic emission to take place on the experimental timescale is roughly 30 eV. By extrapolating the best fit line from Figure 4.20, the lifetime of the triplet state would be expected to be less than 100 ns. Therefore the bump peak is unlikely to be explained by the lifetime of the decaying triplet state.

The area of the bump peak as a function of the laser intensity, from the results plotted in Figure 4.17 (c), was further explored in Figure 4.21 (a). After an initial constant increase, the values rapidly plateaued and stayed constant for a wide range of fragmentation intensities. For instance, at the start

of the plateau, fourth point from the left, the mass spectrum showed only few fullerene fragments, Figure 4.21 (b), while extensive fragmentation was observed with the highest measured laser intensity, Figure 4.21 (c). In (d), the mass spectra corresponding to laser intensities near the start of the plateau were investigated. It appears that the point where the linear behaviour breaks and the plateau begins, corresponds to the appearance of smaller fragments in the mass spectra. This is clearly evident in (e) where the area under the smaller fragments is plotted against the laser intensity.

As was mentioned in Chapter 1.1, the ionisation probability when no intermediate states are present scales with the laser intensity according to I^n, where n is the total number of photons required for the process. Hence, the slope of the double logarithmic plot of the ion yield as a function of the laser intensity would give the photon order required for the process. In Figure 4.21 (a) the slope is equal to 4.1 ± 0.3, indicating a 4-photon process. This trend could suggest that origin of the bump peak could be related to a state which is resonant with the energy of 4 photons. A potential theoretical explanation which could describe why the bump appears in the data will now be provided. The bump could be the result of decay from a superexcited state in C_{60} which is resonant with a 4-photon process. As this state is being populated, the intensity of the bump peak seen in Figure 4.21 (a) increases until it gets saturated. Once it gets saturated, the excitation energy rather than populating the superexcited state,

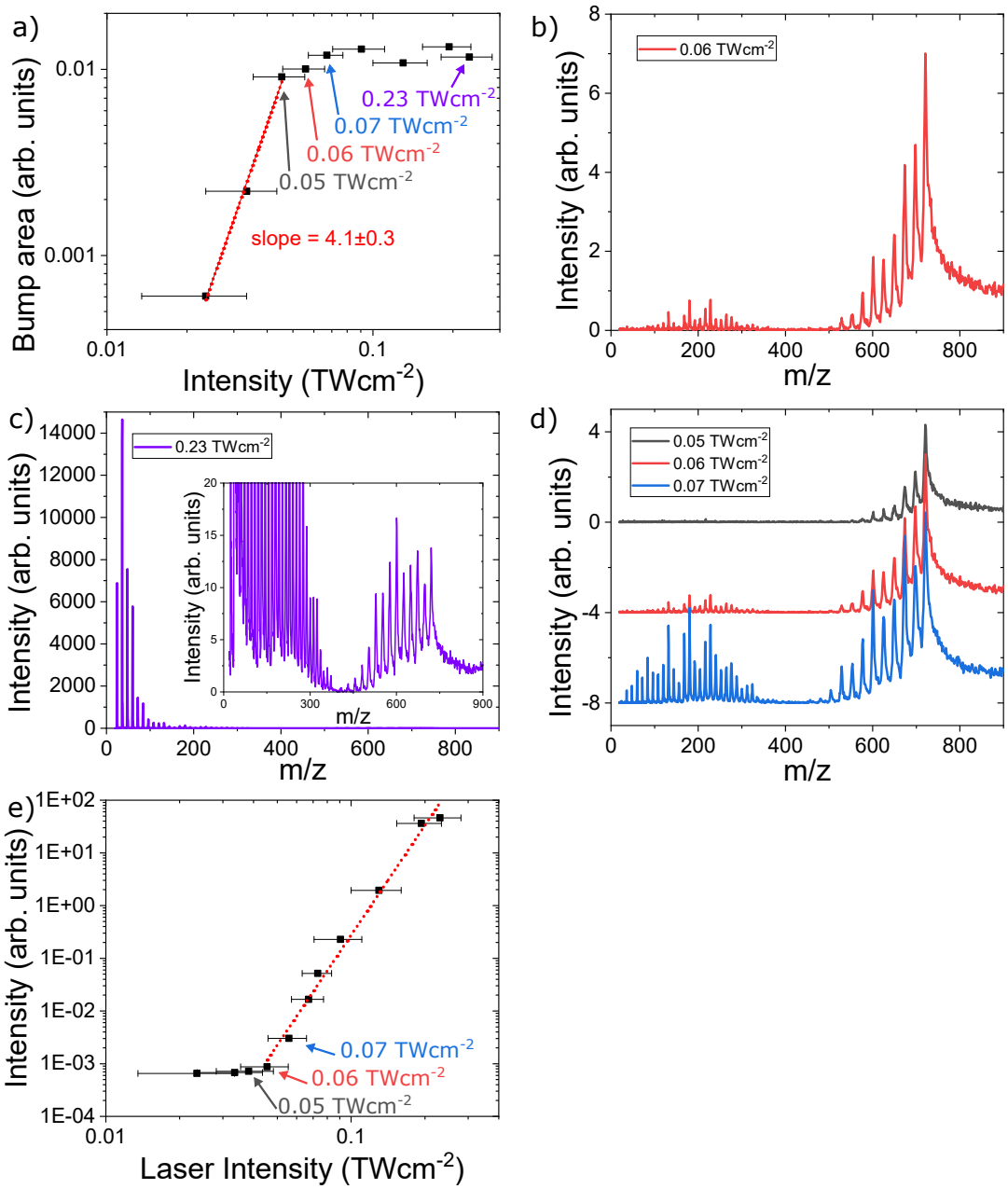

FIGURE 4.21: (a) The area of the bump peak as a function of the laser intensity, plotted in a double logarithmic scale. (b) and (c) are C_{60} mass spectra taken with a laser intensity from the start and end of the plateau in (a) respectively. (b) 0.06 TWcm^{-2} and (c) 0.23 TWcm^{-2}. (d) C_{60} mass spectra taken with laser intensities near where the plateau in (a) starts. (e) The area of the small fragments peaks, C_2 to C_{30}, as a function of the laser intensity. All data were taken using 400 nm, 4±1 ps narrowband pulses.

is accumulated within the vibrational manifold and as such extensive fragmentation occurs, as displayed in Figure 4.21 (e). This would explain why no indication of a bump has been reported in literature when different excitation energies were used. Yasumatsu *et al* had identified several superexcited states in C_{60}, Figure 4.22. However, in their measurements the limit of photon energy that was used was just below 12 eV and in the measurements presented in this thesis, a 4-photon process would populate a state at 12.4 eV. Although Yasumatsu *et al* did not identify this specific superexcited state, their data showed a shoulder from a peak just before 12 eV.

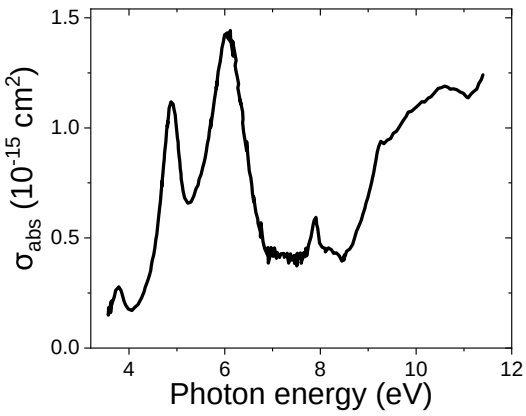

FIGURE 4.22: Gas-phase absorption spectrum of C_{60} recorded at an oven temperature of 850 K. Figure adapted from Yasumatsu *et al*.[158]

Furthermore, from the discussion of Figure 4.14, it was concluded that high-lying Rydberg states may be populated with narrowband pulses. Thus, a slow decay from these long-lived states could also explain the appearance of the bump.

A similar bump behaviour has been reported in two recent studies. Anderson *et al* recorded a spontaneous electron emission from Ag_2^- ions that dominated

their spectra on the ms-s timescale.[156] Hansen theoretically modelled such a behaviour near the freezing point phase transition from the decay rates of clusters.[157] Although these studies do not correlate directly with the C_{60} data, it is interesting that such a behaviour is observed in different systems.

4.2.4 Concluding remarks

The experiments surrounding this chapter were based on testing the fs-ps pump-probe setup which was built to study the SAMO dynamics in C_{60}. Although pump-probe measurements have not yet been achieved, the testing of the individual beams yielded some interesting and unexpected results.

- In a series of photoelectron and mass spectroscopic experiments where the fluence and pulse duration were varied, while the bandwidth of excitation and excitation energy remained constant, the vibronic coupling timescale in C_{60} was identified to be on the order of 240 fs, which is consistent with the previously determined value found in literature. In addition, by investigating the rate of change of the apparent electron temperature and the rate of the production of the delayed ionisation tail as a function of the pulse duration, a time constant of 650-750 fs which is associated with the time that is required for a significant amount of electronic energy to be equilibrated on the vibrational degrees of freedom was identified. After that time, the effects of a vibrationally excited system become dominant over the effects of a hot electronic system. The assumptions in describing these arguments were qualitatively supported by a simple model which has been used in previous studies of the apparent electron temperature in C_{60} and is based on statistical mechanics.

- It was observed that chirped laser pulses induce inhomogeneous broadening of the SAMOs in C_{60}. The results using narrowband excitation showed very similar peak widths as well as inhomogeneous broadening when compared with the chirped elongated broadband pulses. A closer investigation of the optical spectrum revealed that indeed a non-cancelled chirp was present in the narrowband pulses. To further investigate, if indeed, a better energy resolution can be achieved with the narrowband excitation, perfectly optimised chirp-free pulses should be used. Furthermore, a higher intensity of photoelectrons around the photon energy were recorded when narrowband pulses were used. This would suggest that high-lying Rydberg states are populated and subsequently ionised with these ionisation conditions.

- When using narrowband excitation, a bump was superimposed on the delayed ionisation tail in the mass spectra. The origin of this feature was investigated, however, the results were inconclusive. A slow decaying triplet state could not explain the phenomenon. The results indicate that the bump could originate from a decaying long-lived excited electronic state or superexcited state in C_{60}.

5 Conclusion and Outlook

5.1 Conclusion

Through a combination of gas-phase experiments, DFT/TD-DFT calculations and STM/STS experiments, the influence that the encapsulated atom has on the electronic structure of the endohedral fullerenes was investigated by comparing the results for C_{60} and Li@C_{60}.

In the gas-phase experiments, there was contribution from both C_{60} and Li@C_{60} when high purity Li@C_{60} samples were evaporated. The results indicate that a decomposition channel exists where the Li atom is removed from the cage, due to the thermal energy which is supplied to the molecules from the hot source, in combination with so far unidentified chemical reactions. Therefore spectra of C_{60} were acquired with similar excitation conditions in order for the C_{60} contribution to be subtracted from the raw Li@C_{60}/C_{60} data. The results showed that the S_2- and P_Z-SAMO peaks in the PES were split and/or shifted to lower binding energies compared to the C_{60} case. As shown from the TD-DFT calculations, the off-centre position of the Li atom heavily distorts the symmetry of those two SAMOs while the $P_{X/Y}$- and D-SAMOs are less affected.

Ground state DFT calculations were used for the qualitative assignment of the

SAMO peaks in the low-temperature STS spectra of surface bound molecules. Three different cage orientations were recorded for C_{60} molecules while Li@C_{60} molecules were found to have only one, being adsorbed on the surface with a hexagonal face. By performing the experiments at such low temperatures, the Li atom was effectively frozen in space and it's position was fixed between the centre of the cage and the centre of the hexagonal face that was furtherest away from the metal substrate. Hence, due to the asymmetric shape of the S_2- and P_Z-SAMOs, a stronger hybridisation and thus stabilisation between those SAMOs and the metal d-orbitals was evident in the spectra. While the $P_{X/Y}$- and D-SAMOs were unaffected.

An induced switching behaviour was observed in Li@C_{60} molecules. 14 different states were identified in which the Li atom was statistically and reversibly relocated at 5 different height levels across the C_{60} cage (levels 1, 2, 5 and 6 corresponded to positions in front of the different hexagonal faces while the last level was an equatorial position found between levels 3 and 4). A new switching mechanism was proposed in which the Li migration was activated by resonant tunnelling through the $P_{X/Y}$-SAMOs. The justification was based on the fact that these SAMOs are centred on the core of the cage and their electron density is effectively parallel with respect to the metal substrate. Therefore, coupling with the substrate is weaker and there is a higher probability to interact with the endohedral Li atom when they are resonantly excited.

Furthermore, the decay dynamics in photoexcited C_{60} molecules was investigated by varying the laser excitation conditions: laser fluence, pulse duration and bandwidth. The vibronic coupling timescale in C_{60} was confirmed to be around 240 fs. An additional timescale was determined which described

the interplay between the hot and the thermionic electron emissions. That timescale, 650-750 fs, corresponds to the point when thermionic emission dominates over the initial hot electron emission. These findings were supported using a simple model based on statistical mechanics.

A correlation between the laser chirp and the SAMO peak position and broadening mechanism was identified. The results showed that when a considerable amount of chirp was present in the laser pulses, there was inhomogeneous broadening. This is in contrast to the measurements when chirp-free pulses were used that yielded peaks with homogeneous broadening. Hence, in order to obtain information on the lifetime of the SAMOs, chirp-free pulses should be utilised. In addition, when narrowband pulses were used, there was a higher intensity in the PES around the photon energy which suggests that high-lying Rydberg states were being populated. Because of the smaller energy spread in narrowband pulses, there is less efficient energy redistribution and thus there is a higher probability for the electronic energy to climb up the electronic ladder and populate such states.

Lastly, a peak (bump) that was superimposed on the tail of the delayed ionisation was identified for the first time. Irrespectively of the laser intensity, the peak was found at 6.9 µs after the C_{60}^{+} prompt peak. Since the fitted peak widths were getting larger with an increasing laser intensity and the peak positions were constant, an agglomeration of carbon atoms or heavier fullerenes in unlikely be the origin of the bump. A decaying triplet state in C_{60} was also discounted, since with the internal energy that is available in the system after subsequent photon absorptions, the triplet state would be expected to decay on a significantly faster timescale. It was hypothesised that either a decay from

a long-lived superexcited state or from a high-lying Rydberg state could be the origin of the bump.

At this point it would be important to revisit the questions that were posed at the start of this thesis. The investigations within this work have indeed furthered our understanding of the excited state dynamics in fullerenes and endohedral fullerenes. Through a detailed comparison between C_{60} and Li@C_{60}, the effects that the endohedral atom has on the electronic properties of the molecule have been explored. In addition, switching behaviour was observed from single Li@C_{60} surface bound molecules and a unique switching mechanism has been proposed. Moreover, several decay timescales were observed for C_{60}. The vibronic coupling was confirmed in comparison to previous experiments while two new timescales were reported for the first time.

5.2 Outlook

Further theoretical investigations into the exact mechanism that governs the Li switching phenomena should be performed. DFT calculations where the metal substrate is incorporated will allow for a better understanding of how the SAMOs are overlapped with the substrate and how they hybridise with the metal d-orbitals. Since electric fields are expected to distort the shape of the electronic states, it would be interesting to also add an electric field into the calculations. Moreover, calculations identifying the potential energy surfaces of the Li migration could be investigated. To do this, the following methodology is proposed. Perform single point calculations of a surface bound Li@C_{60} molecule where the Li atom is initially placed at the centre of the cage, and

its position is scanned by moving it towards the centre of the 4 different levels of hexagonal rings (for levels 1, 2, 5 and 6) and towards the centre of the C=C bond that joins two adjacent hexagonal rings in levels 3 and 4. Hence, the energetically favourable positions of the 5 different switched states will be calculated. Subsequently, by moving the Li atom across those positions, an energy landscape of the switching behaviour could be modelled.

Furthermore, to test if a better SAMO energy resolution could be achieved using narrowband excitation, genuine chirp-free ps pulses from the SHBC should be utilised. Such an investigation would show if the proposed fs-ps pump-probe experiment would yield the desired results.

By using a range of different wavelength ps narrowband pulses, the structure in the PES that was attributed to indicate an excitation from high-lying Rydberg states could be further investigated. In addition, using the same laser excitation dependency, the origin of the bump could be further explored. If evidence of Rydberg states is found in the PES using different coloured beams and if the bump is still recorded, then a compelling argument that long-lived Rydberg states are responsible for the bump could be made.

Bibliography

[1] H. W. Kroto, J. R. Heath, S. C. O'Brien, R. F. Curl and R. E. Smalley, *Nature*, 1985, **318**, 162–163.

[2] W. Kraetschmer, L. D. Lamb, K. Fostiropoulos and D. R. Huffman, *Nature*, 1990, **347**, 354–358.

[3] J. H. Posthumus, *Reports on Progress in Physics*, 2004, **67**, 623–665.

[4] M. Protopapas, C. H. Keitel and P. L. Knight, *Reports on Progress in Physics*, 1997, **60**, 389–486.

[5] L. V. Keldysh, *Soviet Physics JETP*, 1965, **20**, 1307–1314.

[6] P. H. Bucksbaum, R. R. Freeman, M. Bashkansky and T. J. Mcilratht, *Journal of the Optical Society of America B*, 1987, **4**, 760–764.

[7] P. Agostini, F. Fabre, G. Mainfray, G. Petite and N. K. Rahman, *Physical Review Letters*, 1979, **42**, 1127–1130.

[8] E. E. B. Campbell, K. Hoffmann, H. Rottke and I. V. Hertel, *Journal of Chemical Physics*, 2001, **1716**, 1716–1719.

[9] D. M. Friedrich and W. M. McClain, *Annual review of Physical Chemistry*, 1980, **31**, 559–577.

[10] C. Lifshitz, *Chemical Society Reviews*, 2001, **30**, 186–192.

[11] F. Pagliarulo, B. Climen, B. Baguenard, M. A. Lebeault, A. Ollagnier, J. Wills and C. Bordas, *International Journal of Mass Spectrometry*, 2006, **252**, 100–109.

[12] C. Cauchy, B. J. M., H. Y., A. Rouzee, B. Redlich, A. F. G. V. D. Meer, C. Bordas, M. J. J. Vrakking and F. Lépine, *Physical Review Letters*, 2013, **110**, 193401.

[13] C. Lifshitz, *International Journal of Mass Spectrometry*, 2000, **198**, 1–14.

[14] B. Concina, S. Tomita, J. U. Andersen and P. Hvelplund, *European Physical Journal D*, 2005, **34**, 191–194.

[15] F. Lépine, B. Climen, M. A. Lebeault and C. Bordas, *European Physical Journal D*, 2009, **55**, 627–635.

[16] G. Von Helden, M. T. Hsu, P. R. Kemper and M. T. Bowers, *The Journal of Chemical Physics*, 1991, **95**, 3835–3837.

[17] J. O. Johansson and E. E. B. Campbell, *Chemical Society Reviews*, 2013, **42**, 5661–71.

[18] H. Weidele, D. Kreisle, E. Recknagel, G. Schulze Icking-Konert, H. Handschuh, G. Ganteför and W. Eberhardt, *Chemical Physics Letters*, 1995, **237**, 425–431.

[19] K. Hansen, E. E. B. Campbell and O. Echt, *International Journal of Mass Spectrometry*, 2006, **252**, 79–95.

[20] E. E. B. Campbell, G. Ulmer and I. V. Hertel, *Physical Review Letters*, 1991, **67**, 1986.

[21] M. Hedén, *Ph.D. thesis*, Goteborg University, 2005.

[22] J. O. Johansson, G. G. Henderson and E. E. B. Campbell, *EPJ Web of Conferences*, 2013, **41**, 02015.

[23] I. Shchatsinin, T. Laarmann, G. Stibenz, G. Steinmeyer, A. Stalmashonak, N. Zhavoronkov, C. P. Schulz and I. V. Hertel, *Journal of Chemical Physics*, 2006, **125**, 194320.

[24] K. Hansen, K. Hoffmann and E. E. B. Campbell, *The Journal of Chemical Physics*, 2003, **119**, 2513–2522.

[25] E. E. B. Campbell, K. Hansen, K. Hoffmann, G. Korn, M. Tchaplyguine, M. Wittmann and I. V. Hertel, *Physical Review Letters*, 2000, **84**, 2128–2131.

[26] J. O. Johansson, J. Fedor, M. Goto, M. Kjellberg, J. Stenfalk, G. G. Henderson, E. E. B. Campbell and K. Hansen, *The Journal of Chemical Physics*, 2012, **136**, 164301.

[27] J. O. Johansson, G. G. Henderson, F. Remacle and E. E. B. Campbell, *Physical Review Letters*, 2012, **108**, 173401.

[28] J. Olof Johansson, G. G. Henderson and E. E. B. Campbell, *The Journal of Physical Chemistry A*, 2014, **118**, 8067–8073.

[29] V. R. Bhardwaj, P. B. Corkum and D. M. Rayner, *Physical Review Letters*, 2004, **93**, 043001.

[30] M. Tchaplyguine, K. Hoffmann, O. Dühr, H. Hohmann, G. Korn, H. Rottke, M. Wittmann, I. V. Hertel and E. E. B. Campbell, *Journal of Chemical Physics*, 2000, **112**, 2781–2789.

[31] R. S. Freund, R. F. Stebbings and F. B. Dunning, *Rydberg States of Atoms and Molecules*, Cambridge University Press, 1983.

[32] J. L. Gosselin and P. M. Weber, *Journal of Physical Chemistry A*, 2005, **109**, 4899–4904.

[33] N. Kuthirummal and P. M. Weber, *Chemical Physics Letters*, 2003, **378**, 647–653.

[34] N. Kuthirummal and P. M. Weber, *Journal of Molecular Structure*, 2006, **787**, 163–166.

[35] J. O. Johansson, E. Bohl and E. E. B. Campbell, *Philosophical Transactions Royal Society A*, 2016, **374**, 1–13.

[36] E. Bohl, B. Mignolet, J. O. Johansson, F. Remacle and E. E. B. Campbell, *Physical Chemistry Chemical Physics*, 2017, **19**, 24090–24099.

[37] C. P. Schick and P. M. Weber, *The Journal of Physical Chemistry A*, 2001, **105**, 3725–3734.

[38] M. Boyle, K. Hoffmann, C. P. Schulz, I. V. Hertel, R. D. Levine and E. E. B. Campbell, *Physical Review Letters*, 2001, **87**, 273401.

[39] M. Feng, J. Zhao and H. Petek, *Science*, 2008, **320**, 359–362.

[40] B. Mignolet, J. O. Johansson, E. E. B. Campbell and F. Remacle, *ChemPhysChem*, 2013, **14**, 3332–3340.

[41] H. Reisler and A. I. Krylov, *International Reviews in Physical Chemistry*, 2009, **28**, 267–308.

[42] V. M. Silkin, J. Zhao, F. Guinea, E. V. Chulkov, P. M. Echenique and H. Petek, *Physical Review B - Condensed Matter and Materials Physics*, 2009, **80**, 121408.

[43] M. Boyle, M. Hedén, C. P. Schulz, E. E. B. Campbell and I. V. Hertel, *Physical Review A - Atomic, Molecular, and Optical Physics*, 2004, **70**, 051201.

[44] M. Boyle, T. Laarmann, K. Hoffmann, M. Hedén, E. E. B. Campbell, C. P. Schulz and I. V. Hertel, *European Physical Journal D*, 2005, **36**, 339–351.

[45] J. Zhao, M. Feng, J. Yang and H. Petek, *ACS Nano*, 2009, **3**, 853–864.

[46] M. Feng, J. Zhao, T. Huang, X. Zhu and H. Petek, *Accounts of Chemical Research*, 2011, **44**, 360–368.

[47] M. Feng, Y. Shi, C. Lin, J. Zhao, F. Liu, S. Yang and H. Petek, *Physical Review B*, 2013, **88**, 075417.

[48] M. Iwamoto, D. Ogawa, Y. Yasutake, Y. Azuma, H. Umemoto, K. Ohashi, N. Izumi, H. Shinohara and Y. Majima, *Journal of Physical Chemistry C*, 2010, **114**, 14704–14709.

[49] A. Taninaka, K. Shino, T. Sugai, S. Heike, Y. Terada, T. Hashizume and H. Shinohara, *Nano Letters*, 2003, **3**, 337–341.

[50] S. Usenko, M. Schüler, A. Azima, M. Jakob, L. L. Lazzarino, Y. Pavlyukh, A. Przystawik, M. Drescher, T. Laarmann and J. Berakdar, *New Journal of Physics*, 2016, **18**, 113055.

[51] J. Olof Johansson, E. Bohl, G. G. Henderson, B. Mignolet, T. J. S. Dennis, F. Remacle and E. E. B. Campbell, *The Journal of Chemical Physics*, 2013, **139**, 084309.

[52] E. Bohl, K. P. Sokół, B. Mignolet, J. O. F. Thompson, J. O. Johansson, F. Remacle and E. E. B. Campbell, *Journal of Physical Chemistry A*, 2015, **119**, 11504–11508.

[53] T. Huang, J. Zhao, M. Feng, H. Petek, S. Yang and L. Dunsch, *Physical Review B*, 2010, **81**, 085434.

[54] T. Huang, J. Zhao, M. Feng, A. A. Popov, S. Yang, L. Dunsch and H. Petek, *Nano Letters*, 2011, **11**, 5327–5332.

[55] T. Huang, J. Zhao, M. Feng, A. A. Popov, S. Yang, L. Dunsch and H. Petek, *Chemical Physics Letters*, 2012, **552**, 1–12.

[56] C. Rullière, *Femtosecond Laser Pulses: Principles and Experiments*, 2nd edn., 2005.

[57] D. Strickland and G. Mourou, *Optics Communications*, 1985, **56**, 219–221.

[58] L. Conversion, *TOPAS white manual*.

[59] J. O. Johansson, *Ph.D. thesis*, University of Edinburgh, 2010.

[60] J. Abrefah, D. R. Olander, M. Balooch and W. J. Siekhaus, *Applied Physics Letters*, 1992, **60**, 1313–1314.

[61] W. C. Wiley and I. H. McLaren, *Review of Scientific Instruments*, 1955, **26**, 1150–1157.

[62] B. J. Whitaker, *Imaging in Molecular Dynamics: Technology and Applications*, Cambridge University Press, 1st edn., 2003.

[63] B. J. Whitaker, in *Imaging in Chemical Dynamics*, 2001, pp. 68–86.

[64] D. H. Parker and E. Andr, *Velocity map imaging: applications in molecular dynamics and experimental aspects*, 2003, pp. 20–64.

[65] A. T. J. B. Eppink, S.-m. Wu and B. J. Whitaker, *Reconstruction methods*, 2003, pp. 65–112.

[66] E. R. Grumbling, K. Pichugin, R. Mabbs and A. Sanov, *Journal of Chemical Education*, 2011, **88**, 1515–1520.

[67] K. L. Reid, *Annual review of physical chemistry*, 2003, **54**, 397–424.

[68] R. N. Z. J. Cooper, *The Journal of Chemical Physics*, 1968, **48**, 942.

[69] R. N. Z. J. Cooper, *Journal of Chemical Physics*, 1968, **49**, 4252.

[70] R. Mabbs, E. R. Grumbling, K. Pichugin and A. Sanov, *Chemical Society Reviews*, 2009, **38**, 2169–2177.

[71] G. M. Roberts, J. L. Nixon, J. Lecointre, E. Wrede and J. R. R. Verlet, *Review of Scientific Instruments*, 2009, **80**, 053104.

[72] K. Zhao, T. Colvin, W. T. Hill and G. Zhang, *Review of Scientific Instruments*, 2002, **73**, 3044.

[73] G. G. Henderson, *Ph.D. thesis*, University of Edinburgh, 2012.

[74] V. Dribinski, A. Ossadtchi, V. A. Mandelshtam and H. Reisler, *Review of Scientific Instruments*, 2002, **73**, 2634.

[75] P. Kaminski, R. Wiehle, V. Renard, A. Kazmierczak, B. Lavorel, O. Faucher and B. Witzel, *Physical Review A - Atomic, Molecular, and Optical Physics*, 2004, **70**, 053413.

[76] V. Schyja, T. Lang and H. Helm, *Physical Review A - Atomic, Molecular, and Optical Physics*, 1998, **57**, 3692–3697.

[77] R. R. Freeman, P. H. Bucksbaum, H. Milchberg, S. Darack, D. Schumacher and M. E. Geusic, *Physical Review Letters*, 1987, **59**, 1092–1095.

[78] M. J. Frisch, G. W. Trucks, H. B. Schlegel, G. E. Scuseria, M. A. Robb, J. R. Cheeseman, G. Scalmani, V. Barone, B. Mennucci, G. A. Petersson, H. Nakatsuji, M. Caricato, X. Li, H. P. Hratchian, A. F. Izmaylov, J. Bloino, G. Zheng, J. L. Sonnenberg, M. Hada, M. Ehara, K. Toyota, R. Fukuda, J. Hasegawa, M. Ishida, T. Nakajima, Y. Honda, O. Kitao, H. Nakai,

T. Vreven, J. A. Montgomery, J. E. Peralta, F. Ogliaro, M. Bearpark, J. J. Heyd, E. Brothers, K. N. Kudin, V. N. Staroverov, R. Kobayashi, J. Normand, K. Raghavachari, A. Rendell, J. C. Burant, S. S. Iyengar, J. Tomasi, M. Cossi, N. Rega, J. M. Millam, M. Klene, J. E. Knox, J. B. Cross, V. Bakken, C. Adamo, J. Jaramillo, R. Gomperts, R. E. Stratmann, O. Yazyev, A. J. Austin, R. Cammi, C. Pomelli, J. W. Ochterski, R. L. Martin, K. Morokuma, V. G. Zakrzewski, G. A. Voth, P. Salvador, J. J. Dannenberg, S. Dapprich, A. D. Daniels, Ö. Farkas, J. B. Foresman, J. V. Ortiz, J. Cioslowski and D. J. Fox, *Gaussian 09*, 2009.

[79] J. Foresman and A. Frisch, *Exploring chemistry with electronic structure methods*, Second edi edn., 1996.

[80] D. R. Bowler, *Contemporary Physics*, 2018, **59**, 377–390.

[81] A. G. Orpen and C. A. Morrison, *Structural systematics in molecular inorganic chemistry*, Wiley, 1993, pp. 191–197.

[82] P. Hohenberg and W. Kohn, *Physical Review*, 1964, **136**, 864–871.

[83] W. Kohn and L. J. Sham, *Physical Review*, 1965, **140**, 1133–1138.

[84] E. Runge and E. K. U. Gross, *Physical Review Letters*, 1984, **52**, 997–1000.

[85] E. K. U. Gross and N. T. Maitra, *Fundamentals of Time-Dependent Density Functional Theory: Introduction to TDDFT*, Springer, 2012.

[86] H. J. W. Zandvliet and A. V. Houselt, *Annual Review of Analytical Chemistry*, 2009, **2**, 37–55.

[87] K. W. Hipps, in *Handbook of Applied Solid State Spectroscopy*, Springer, Boston, MA, 2005, ch. 7, pp. 1–33.

[88] G. Schulze, K. J. Franke and J. I. Pascual, *New Journal of Physics*, 2008, **10**, 065005.

[89] M. Stefanou, H. J. Chandler, B. Mignolet, E. Williams, S. A. Nanoh, F. Remacle, R. Schaub and E. E. B. Campbell, *Nanoscale*, 2019, **11**, 2668–2678.

[90] H. J. Chandler, M. Stefanou, E. E. B. Campbell and R. Schaub, *Nature Communications*, 2019, **10**, 2283.

[91] H. Shinohara, *Reports on Progress in Physics*, 2000, **63**, 843–892.

[92] A. A. Popov, *Endohedral Fullerenes : Electron Transfer and Spin*, Springer, 2017.

[93] Y. Chai, T. Guo, C. Jin, R. E. HauflerJ, L. P. Felipe Chibante, J. Fure, L. Wang, J. Michael Alford and R. E. Smalley, *Journal of Physical Chemistry*, 1991, **95**, 7564–7568.

[94] H. Shinohara, H. Sato, Y. Saito, M. Ohkohchi and Y. Ando, *Journal of Physical Chemistry*, 1992, **96**, 3571–3573.

[95] H. Shinohara, H. Sato, M. Ohkohchi, Y. Ando, T. Kodama, T. Shida, T. Kato and Y. Saito, *Nature*, 1992, **357**, 52–54.

[96] H. Shinohara, N. Hayashi, H. Sato, Y. Saito, X. D. Wang, T. Hashizume and T. Sakurai, *The Journal of Physical Chemistry*, 1993, **97**, 13438–13440.

[97] A. Gromov, D. Ostrovskii, A. Lassesson, M. Jo and E. E. B. Campbell, *Journal of Physical Chemistry B*, 2003, **107**, 11290–11301.

[98] R. Tellgmann, N. Krawez, S.-H. Lin, I. V. Hertel and E. E. B. Campbell, *Nature*, 1996, **382**, 407–408.

[99] E. E. B. Campbell, R. Tellgmann, N. Krawez and I. V. Hertel, *Journal of Physics and Chemistry of Solids*, 1997, **58**, 1763–1769.

[100] N. Krawez, A. Gromov, K. Buttke and E. E. B. Campbell, *European Physical Journal D*, 1999, **9**, 345–349.

[101] H. Ueno, S. Aoyagi, Y. Yamazaki, K. Ohkubo, N. Ikuma, H. Okada, T. Kato, Y. Matsuo, S. Fukuzumi and K. Kokubo, *Chemical Science*, 2016, **7**, 5770–5774.

[102] S. Aoyagi, E. Nishibori, H. Sawa, K. Sugimoto, M. Takata, Y. Miyata, R. Kitaura, H. Shinohara, H. Okada, T. Sakai, Y. Ono, K. Kawachi, K. Yokoo, S. Ono, K. Omote, Y. Kasama, S. Ishikawa, T. Komuro and H. Tobita, *Nature Chemistry*, 2010, **2**, 678–683.

[103] H. Okada, T. Komuro, T. Sakai, Y. Matsuo, Y. Ono, K. Omote, K. Yokoo, K. Kawachi, Y. Kasama, S. Ono, R. Hatakeyama, T. Kaneko and H. Tobita, *RSC Advances*, 2012, **2**, 10624–10631.

[104] S. Aoyagi, Y. Sado, E. Nishibori, H. Sawa, H. Okada, H. Tobita, Y. Kasama, R. Kitaura and H. Shinohara, *Angewandte Chemie - International Edition*, 2012, **51**, 3377–3381.

[105] B. I. Dunlap, J. L. Ballester and P. P. Schmidt, *Journal of Physical Chemistry*, 1992, **96**, 9781–9787.

[106] Y. S. Li and D. Tomanek, *Chemical Physics Letters*, 1994, **221**, 453–458.

[107] Y. Yamada, A. V. Kuklin, S. Sato, F. Esaka, N. Sumi, C. Zhang, M. Sasaki, E. Kwon, Y. Kasama, P. V. Avramov and S. Sakai, *Carbon*, 2018, **133**, 23–30.

[108] Y. F. Yang, E. V. Gromov and L. S. Cederbaum, *Journal of Physical Chemistry Letters*, 2019, **10**, 7617–7622.

[109] H. Yagi, N. Ogasawara, M. Zenki, T. Miyazaki and S. Hino, *Chemical Physics Letters*, 2016, **651**, 124–126.

[110] D. L. Lichtenberger, K. W. Nebesny, C. D. Ray, D. R. Huffman and L. D. Lamb, *Chemical Physics Letters*, 1991, **176**, 203–208.

[111] F. Rohmund, A. V. Bulgakov, M. Hedén, A. Lassesson and E. E. B. Campbell, *Chemical Physics Letters*, 2000, **323**, 173–179.

[112] V. N. Popok, I. I. Azarko, A. Gromov, M. Jönsson, A. Lassesson and E. E. B. Campbell, *Solid State Communications*, 2005, **133**, 499–503.

[113] L. Pavanello, Michele; Jalbout, Abraham, F; Trzaskowski, Bartosz; Adamowicz, *Chemical Physics Letters*, 2007, **442**, 339–343.

[114] V. N. Popok, A. Gromov, M. Jonsson, A. Taninaka, H. Shinohara and E. E. B. Campbell, *Nano*, 2008, **3**, 155–160.

[115] A. Lassesson, K. Hansen, M. Joensson, A. Gromov, E. E. B. Campbell, M. Boyle, D. Pop, C. P. Schulz, I. V. Hertel, A. Taninaka and H. Shinohara, *European Physical Journal D*, 2005, **34**, 205–209.

[116] C. Kusch, N. Krawez, R. Tellgmann, B. Winter and E. E. B. Campbell, *Applied Physics A: Materials Science and Processing*, 1998, **66**, 293–298.

[117] H. J. Chandler, *Ph.D. thesis*, University of St. Andrews, 2020.

[118] W. Humphrey, A. Dalke and K. Schulten, *Journal of Molecular Graphics*, 1996, **14**, 33–38.

[119] J. Stone, *Ph.D. thesis*, University of Missouri-Rolla, 1998.

[120] G. Schull, N. Néel, M. Becker, J. Kröger and R. Berndt, *New Journal of Physics*, 2008, **10**, 065012.

[121] J. A. Gardener, G. A. D. Briggs and M. R. Castell, *Physical Review B - Condensed Matter and Materials Physics*, 2009, **80**, 235434.

[122] B. Mignolet, E. E. B. Campbell and F. Remacle, *AIP Conference Proceedings*, 2017, **1906**, 030027.

[123] P. Wurz and K. R. Lykke, *The Journal of Chemical Physics*, 1991, **95**, 7008–7010.

[124] X. Lu, M. Grobis, K. H. Khoo, S. G. Louie and M. F. Crommie, *Physical Review B - Condensed Matter and Materials Physics*, 2004, **70**, 115418.

[125] G. Reecht, B. W. Heinrich, H. Bulou, F. Scheurer, L. Limot and G. Schull, *New Journal of Physics*, 2017, **19**, 113033.

[126] X. Torrelles, M. Pedio, C. Cepek and R. Felici, *Physical Review B*, 2012, **86**, 075461.

[127] S. Leach, M. Vervloet, A. Desprès, E. Bréheret, J. P. Hare, T. John Dennis, H. W. Kroto, R. Taylor and D. R. Walton, *Chemical Physics*, 1992, **160**, 451–466.

[128] A. Aviram and M. A. Ratner, *Chemical Physics Letters*, 1974, **29**, 277–283.

[129] A. Nitzan and M. A. Ratner, *Science*, 2003, **300**, 1384–1390.

[130] D. Xiang, X. Wang, C. Jia, T. Lee and X. Guo, *Chemical Reviews*, 2016, **116**, 4318–4440.

[131] W. Auwarter, K. Seufert, F. Bischoff, D. Ecija, S. Vijayaraghavan, S. Joshi, F. Klappenberger, N. Samudrala and J. V. Barth, *Nature Nanotechnology*, 2012, **7**, 41–46.

[132] S. Aoyagi, Y. Sado, E. Nishibori, H. Sawa, H. Okada, H. Tobita, Y. Kasama, R. Kitaura and H. Shinohara, *Angewandte Chemie - International Edition*, 2012, **51**, 3377–3381.

[133] S. Aoyagi, A. Tokumitu, K. Sugimoto, H. Okada, N. Hoshino and T. Akutagawa, *Journal of the Physical Society of Japan*, 2016, **85**, 094605.

[134] E. Kwon, K.-i. Komatsu, K. Kawachi, Y. Kasama and T. Endo, *Molecular Crystals and Liquid Crystals*, 2014, **598**, 28–31.

[135] H. Suzuki, M. Ishida, M. Yamashita, C. Otani, K. Kawachi, Y. Kasama and E. Kwon, *Physical Chemistry Chemical Physics*, 2016, **18**, 31384–31387.

[136] M. Stefanou, H. J. Chandler, B. Mignolet, E. Williams, S. A. Nanoh, J. O. F. Thompson, F. Remacle, R. Schaub and E. E. B. Campbell, *Nanoscale*, 2019, **11**, 2668–2678.

[137] C. P. Collier, G. Mattersteig, E. W. Wong, Y. Luo, K. Beverly, J. Sampaio, F. M. Raymo, J. F. Stoddart and J. R. Heath, *Science*, 2000, **289**, 1172–1175.

[138] Y. Yasutake, Z. Shi, T. Okazaki, H. Shinohara and Y. Majima, *Nano Letters*, 2005, **5**, 1057–1060.

[139] M. Alemani, M. V. Peters, S. Hecht, K. H. Rieder, F. Moresco and L. Grill, *Journal of the American Chemical Society*, 2006, **128**, 14446–14447.

[140] G. Raggi, A. J. Stace and E. Bichoutskaia, *Physical Chemistry Chemical Physics*, 2014, **16**, 23869–23873.

[141] C. Foroutan-Nejad, V. Andrushchenko and M. Straka, *Physical Chemistry Chemical Physics*, 2016, **18**, 32673–32677.

[142] N. Pavliček, B. Fleury, M. Neu, J. Niedenführ, C. Herranz-Lancho, M. Ruben and J. Repp, *Physical Review Letters*, 2012, **108**, 1–5.

[143] G. J. Simpson, S. W. L. Hogan, M. Caffio, C. J. Adams, H. Früchtl, T. van Mourik and R. Schaub, *Nano Letters*, 2014, **14**, 634–639.

[144] R. Jorn, J. Zhao, H. Petek and T. Seideman, *ACS Nano*, 2011, **5**, 7858–7865.

[145] K. Hansen and O. Echt, *Physical Review Letters*, 1997, **78**, 2337–2340.

[146] F. Rohmund, M. Hedén, A. V. Bulgakov and E. E. B. Campbell, *Journal of Chemical Physics*, 2001, **115**, 3068.

[147] E. E. B. Campbell, K. Hoffmann and I. V. Hertel, *European Physical Journal D*, 2001, **16**, 345–348.

[148] E. E. B. Campbell, G. Ulmer, B. Hasselberger, H. G. Busmann and I. V. Hertel, *Journal of Chemical Physics*, 1990, **93**, 6900–6907.

[149] R. Ehlich, M. Westerburg and E. E. B. Campbell, *Journal of Chemical Physics*, 1996, **104**, 1900–1911.

[150] L. Conversion, *Personal communication with Light Conversion laser technician*, 2019.

[151] G. Walder, K. W. Kennedy and O. Echt, *Zeitschrift für Physik D Atoms, Molecules and Clusters*, 1993, **26**, 288–290.

[152] C. Bordas, B. Baguenard, B. Climen, M. A. Lebeault, F. Lépine and F. Pagliarulo, *European Physical Journal D*, 2005, **34**, 151–155.

[153] B. Tsipinyuk, A. Budrevich, M. Grinberg and E. Kolodney, *Journal of Chemical Physics*, 1997, **106**, 2449–2457.

[154] R. Deng, M. Treat, O. Echt and K. Hansen, *Journal of Chemical Physics*, 2003, **118**, 8563–8565.

[155] H. T. Etheridge, R. D. Averitt, N. J. Halas and R. B. Weisman, *Journal of Physical Chemistry*, 1995, **99**, 11306–11308.

[156] E. K. Anderson, P. K. Najeeb, G. Eklund, K. C. Chartkunchand, S. Rosen, Å. Larson, K. Hansen, H. Cederquist, H. Zettergren and H. T. Schmidt, *Physical Review Letters*, 2020, **173001**, 1–5.

[157] K. Hansen, *Mass Spectrometry Reviews*, 2020, **00**, 1–16.

[158] H. Yasumatsu, T. Kondow, H. Kitagawa, K. Tabayashi and K. Shobatake, *Journal of Chemical Physics*, 1996, **104**, 899–902.

Appendices

A Colour-coded cage diagrams

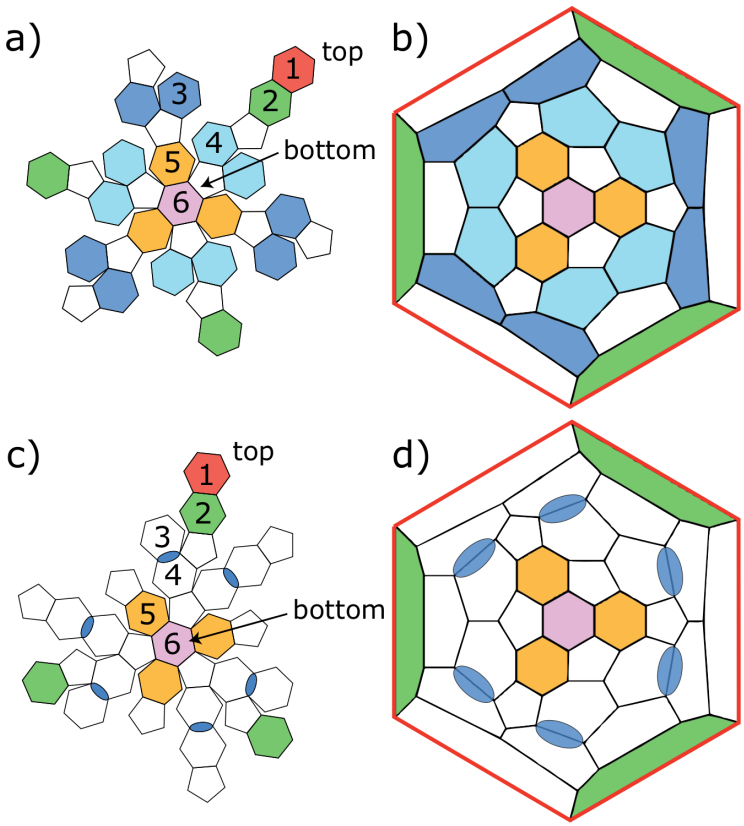

FIGURE A.1: Different representations of the colour-coded C_{60} cage. (a) and (c) deconstructed cage diagrams. (b) and (d) Schlegel diagrams. The Schlegel diagrams are viewed from the axis that passes through the centre of levels 1 and 6 where the outer hexagon corresponds to level 1. (b) and (d) show the updated understanding of all the different Li atom coordinations that were observed in the experiments. The blue highlights represent the equatorial Li positions which are referred to in the discussion as level 3/4.